

# Détection des polarisations cachées dans des matériaux centrosymétriques avec la résonance magnétique nucléaire

par

Jorge Eduardo Ramírez-Ruiz

Mémoire présenté au département de physique  
en vue de l'obtention du grade de maître ès sciences (M.Sc.)

FACULTÉ des SCIENCES  
UNIVERSITÉ de SHERBROOKE

Sherbrooke, Québec, Canada, 25 juillet 2018

Le 25 juillet 2018

*le jury a accepté le mémoire de Monsieur Jorge Eduardo Ramírez-Ruiz dans sa version finale.*

Membres du jury

Professeur Ion Garate  
Directeur de recherche  
Département de physique

Professeur Claude Bourbonnais  
Président Rapporteur  
Département de physique

Professeur Dennis Morris  
Évaluateur interne  
Département de physique

À ma famille, mes amis et mon amour

# Sommaire

Des travaux théoriques récents ont démontré la présence de textures de spin et orbitales cachées dans des matériaux non-magnétiques qui présentent une symétrie d'inversion. Quelques expériences ont déjà été faites pour les faire apparaître, mais toutes brisent la symétrie d'inversion avec une surface. Ici, on propose que ces textures peuvent être détectées dans le volume avec la résonance magnétique nucléaire (RMN) sous un champ électrique. Dans les cristaux avec ces polarisations, un champ électrique uniforme produit, aux sites atomiques reliés par l'inversion spatiale, un champ magnétique qui pointe dans des directions opposées. Comme résultat, le signal de résonance qui correspond à ces sites est divisé en deux. La grandeur de cet effet de dédoublement est proportionnelle au champ électrique et dépend de son orientation par rapport aux axes du cristal et au champ magnétique externe. Comme étude de cas, on présente une théorie du dédoublement du signal de la RMN sous un champ électrique pour  $^{77}\text{Se}$ ,  $^{125}\text{Te}$  et  $^{209}\text{Bi}$  dans  $\text{Bi}_2\text{Se}_3$  et  $\text{Bi}_2\text{Te}_3$ . Dans des échantillons conducteurs soumis à une densité de courant de  $\simeq 10^6 \text{ A/cm}^2$ , ce dédoublement pour Bi peut atteindre 100 kHz, ce qui est comparable ou même plus grand que la largeur intrinsèque du signal. Pour observer cet effet dans les expériences, ce dédoublement doit aussi surpasser la largeur produite par le champ d'Ørsted. Dans  $\text{Bi}_2\text{Se}_3$ , cela demande des fils étroits avec des rayons  $\lesssim 1 \mu\text{m}$ . En outre, on discute d'autres matériaux prometteurs, comme  $\text{SrRuO}_3$  et  $\text{BaIr}_2\text{Ge}_2$ , dont les symétries permettent d'utiliser des stratégies pour supprimer la largeur produite par le champ d'Ørsted. Finalement, on discute les projets futurs sur ce sujet, notamment deux projets qui sont en train d'être développés et qui sont motivés par des expériences.

Mots clés: Polarisation de spin, résonance magnétique nucléaire, réponse linéaire, matériaux centrosymétriques, modèle de liaisons fortes, groupes de symétries.

# Remerciements

Tout d'abord, un gros merci à mon superviseur Ion Garate pour l'encadrement, le support et la compréhension. Merci de me laisser le temps de comprendre mon sujet, de me motiver à travailler à mon rythme et de me donner l'opportunité d'assister à toutes les écoles d'été et conférences. Merci aussi pour les conseils à chaque rédaction et présentation, ainsi que tous ces petits conseils de vie. Merci également à Mitacs pour le support financier.

Merci aux Garate Kids: Samuel, Pedro, Pierre, Simon, Silvia, Kush et Sara pour les conversations, l'ouverture et le support. Ces deux années ont été amusantes grâce à votre aide et votre disposition à être là pour les autres. Un merci spécial à Samuel pour m'aider à chaque fois que j'avais une question, que ça ait été de son code, de présentations ou de physique. Merci également à Silvia Cárdenas et Chloé Gauvin-Ndyae pour vos travaux qui ont soutenu le mien. J'aimerais remercier aussi le département de physique de l'Université, un endroit stimulant pour travailler collaborativement. Les conversations avec les professeurs (notamment Jeffrey Quilliam et Michel-Piolo Ladrière) et leurs étudiants ont vraiment aidé à consolider mon projet.

Gracias a mis amigos de la UNAM: Ana Pau, Fer, Arturo, Luis, Rodrigo, Aramis. Ya sea por algunas llamadas esporádicas, visitas o conversaciones escritas, ustedes me recuerdan los grandes años que pasamos y siempre estarán en mi corazón. Le doy las gracias a mi madre, mi padre y a mis hermanos por todo el amor y ayuda, cerca o a la distancia. Gracias por los consejos y el apoyo con todas las decisiones tomadas y por tomar. Me hacen falta y ustedes saben lo mucho que significan para mí.

Finally, I would like to thank Rachel for all the love. Thank you for being there for me in the good times and helping me with those little frustrations during all this time. You remind me that life is simple and beautiful, and always a little bit more when we are together. I look forward to all the adventures ahead of us.

# Contents

<b>Sommaire</b>	<b>iii</b>
<b>Introduction</b>	<b>1</b>
<b>1 Hidden electronic polarizations in centrosymmetric materials</b>	<b>3</b>
1.1 Bloch Theorem . . . . .	4
1.2 Band degeneracy . . . . .	5
1.2.1 Inversion symmetry . . . . .	7
1.2.2 Time-reversal operator . . . . .	9
1.2.3 Kramers theorem . . . . .	11
1.2.4 Double degeneracy . . . . .	12
1.3 <i>Hidden</i> spin polarization . . . . .	13
1.4 Inversion-symmetry breaking . . . . .	15
1.4.1 Angular dependence of the orbital hopping . . . . .	17
1.4.2 Spinless, matrix Hamiltonian on a square lattice . . . . .	18
1.4.3 Calculating orbital angular momentum . . . . .	20
1.5 Crystallographic space and point groups . . . . .	21
1.5.1 Point groups . . . . .	22
1.5.2 Space groups . . . . .	22
1.5.3 Site symmetry groups and Wyckoff positions . . . . .	23
1.5.4 A useful example . . . . .	24
<b>2 Nuclear magnetic resonance in an electric field</b>	<b>26</b>
2.1 Nuclear magnetic resonance . . . . .	27
2.1.1 Resonance condition . . . . .	28
2.1.2 Spin-spin interactions . . . . .	30
2.1.3 Orbital currents . . . . .	33
2.2 Staggered magnetic response . . . . .	35
2.2.1 Linear response . . . . .	38

<i>Contents</i>	vi
2.3 Current-related complications . . . . .	40
<b>3 Material application: <math>\text{Bi}_2\text{Se}_3</math> and <math>\text{Bi}_2\text{Te}_3</math></b>	<b>43</b>
3.1 Tight-binding approximation . . . . .	44
3.2 Linear response of the hidden polarizations . . . . .	46
3.2.1 Magnetic textures . . . . .	47
3.2.2 Staggered magnetization . . . . .	48
3.2.3 Amperian linewidth and Joule heating . . . . .	51
3.3 Other materials . . . . .	53
<b>4 Future work</b>	<b>57</b>
4.1 Hidden orbital polarization in Silicon . . . . .	58
4.1.1 Tight-binding hamiltonian under strain . . . . .	59
4.1.2 Preliminary results . . . . .	60
4.2 Hidden electrical polarization under external magnetic field . . . . .	62
4.2.1 Local dipole moment operator . . . . .	63
4.2.2 Matrix elements in the tight-binding basis . . . . .	64
4.2.3 Preliminary results . . . . .	65
<b>Conclusion</b>	<b>67</b>
<b>A Symmetry constraints in the form of the magnetoelectric tensor</b>	<b>69</b>
<b>B Spin and orbital contributions to the staggered magnetization</b>	<b>72</b>
<b>Bibliography</b>	<b>72</b>

# List of Tables

4.1 Preliminary values for hidden electric dipole in $\text{Bi}_2\text{Se}_3$ . . . . .	65
---	----

# List of Figures

1.1	Band structure of $\text{Bi}_2\text{Se}_3$ as calculated with a tight-binding Hamiltonian . . .	6
1.2	Crystal structure of $\text{Bi}_2\text{Se}_3$ and $\text{Bi}_2\text{Te}_3$ . . . . .	24
2.1	The nuclear resonance frequency at inversion partner sites depends on the relative orientation between the staggered magnetic field and the external magnetic field . . . . .	37
3.1	Bulk tight-binding bands for $\text{Bi}_2\text{Se}_3$ and $\text{Bi}_2\text{Te}_3$ . . . . .	45
3.2	Momentum-space spin textures for $\text{Se}_{\text{out}}$ and Bi in $\text{Bi}_2\text{Se}_3$ for the conduction and valence bands for inversion partners . . . . .	46
3.3	Momentum-space spin and orbital textures for $\text{Se}_{\text{out}}$ and Bi in $\text{Bi}_2\text{Se}_3$ for the conduction and valence bands . . . . .	47
3.4	Electric-field-induced staggered magnetic field as a function of the carrier density for different nuclei in $\text{Bi}_2\text{Se}_3$ and $\text{Bi}_2\text{Te}_3$ . . . . .	48
3.5	Electric-field-induced staggered magnetic field as a function of the electronic scattering rate for the conducting scenario . . . . .	49
3.6	Electric-field-induced staggered magnetic field as a function of the electronic scattering rate in the insulating case . . . . .	50
3.7	NMR peak splitting for various experimentally reported sample parameters as a function of current density . . . . .	51
3.8	Shape of the NMR signal that probes the hidden polarization and its dependence on the sample size . . . . .	52
3.9	Materials that present a favorable NMR experimental configuration to probe the hidden polarization effect . . . . .	54
4.1	Tight-binding relaxed band structure of silicon . . . . .	60
4.2	Staggered magnetization in silicon as a function of carrier density for fixed strain . . . . .	61

4.3	Staggered magnetization in silicon as a function of strain for fixed carrier density . . . . .	62
B.1	Contributions to the staggered magnetization at the Bi sites as a function of carrier density . . . . .	73
B.2	Contributions to the staggered magnetization at the Se <sub>out</sub> sites as a function of carrier density . . . . .	73

# Introduction

In non-magnetic materials with inversion symmetry, all electronic bands are at least two-fold degenerate. Until recently, it was believed that this degeneracy would prohibit any spin polarization of bands. This view has been dispelled through the discovery that degenerate Bloch states can have nonzero spin[1] and orbital[2] polarizations when projected to real-space positions whose *local* symmetry lacks an inversion center.

These spin and orbital polarizations are “hidden” in two ways. First, they take opposite directions in atoms related by spatial inversion, such that the average of spin or orbital texture over a unit cell vanishes. This is a consequence of the global inversion symmetry in the crystal. Second, upon summing over occupied states in the first Brillouin zone, the momentum-space polarizations add to zero. In other words, these polarizations are hidden both in real and momentum space. However, the existence of nonzero magnetic textures allows us to search for techniques to visualize them. To this date, all the experimental techniques [3, 4, 5] have focused on breaking the global inversion symmetry of the crystal with a surface. Therefore, by using surface-sensitive probes we have access to the spin textures in momentum space and thus it could be possible to reveal them. There is however a substantial problem in this approach pointed out by the authors of Ref. [6]. Using surfaces that inherently break the inversion symmetry renders the access to the bulk states unreliable. Therefore, in this mémoire we develop a theory of nuclear magnetic resonance (NMR) under an electric field as a bulk probe of the hidden polarizations. Through this approach, there is no explicit inversion symmetry breaking, and we propose to reveal these textures by inducing a real-space staggered magnetization within each unit cell of the crystal.

The idea that electric fields can induce real-space spin textures has attracted significant interest in spintronics in general and in the development of new magnetic memory devices in particular [7]. For example, the hidden spin polarization enables to write information in antiferromagnetic memory devices using electric fields. The use of NMR in the detection and characterization of hidden polarizations could bring this powerful experimental technique

closer to spintronics applications.

In chapter 1, we introduce and find out the explicit representations of the most important symmetries that render these textures hidden in a crystal: time reversal and inversion. We then explain what the hidden spin and orbital textures mean in our context. Lastly, we revise some group-theory concepts that help us understand more of the symmetries of any crystal – to finally explore the symmetries of  $\text{Bi}_2\text{Se}_3$  and  $\text{Bi}_2\text{Te}_3$ , which will be the systems under study in the following chapters.

Knowing what the hidden polarizations mean, in chapter 2 we revise the necessary theory of NMR. First, we go over the most important concepts in an NMR experiment for our context – namely the resonance frequencies and the interactions of nuclei with electrons. Armed with these concepts, we tackle the linear response formalism that we need to calculate the magnetic field induced in a nucleus when an electric field is turned on, by polarizing the electrons. The application of an electric field in a conducting material induces a current, which brings itself some complications that we evaluate at the end of the chapter.

In chapter 3, we apply the previous idea to a physical system: the  $\text{Bi}_2\text{Se}_3$  and  $\text{Bi}_2\text{Te}_3$  crystals. We apply an existing tight-binding model for these crystals to express the Bloch states in these basis. It is then a matter of plugging our states in the linear response theory developed in the previous chapter to evaluate the magnetic field that will generate a peak-splitting in the NMR experiments. We present our results and the evaluation of the possible complications that could arise in actual experiments. At the end of this chapter, we propose some solutions that could help us improve the experimental setup for the discovery of the hidden polarizations.

Having explored a physical system where we showed the possible use of NMR to probe our effect, we explore in chapter 4 the possible research avenues in the foreseeable future. First, we consider the possible application of the resonance frequency control by a current in spin qubits in silicon. By using the same ideas, we basically apply the formalism that we know in a silicon crystal. Secondly, we examine the possibility to have a converse effect, in which a magnetic perturbation could induce a hidden electrical response that is localized and compensates within a unit cell. Finally, we give our insights and conclusions of the problem and on the appendices some additional results and symmetry arguments are presented.

## Chapter 1

# Hidden electronic polarizations in centrosymmetric materials

From the perspective of an electron wandering in vacuum, materials can be regarded as things that break the continuous translational symmetry of space. In particular, crystals break this symmetry while bringing however a discrete translational symmetry due to the periodic arrangement of atoms. Considering the scales in the usual problems, and if we are looking at bulk properties of the material, this periodicity can be thought to be infinite. Let us then consider a Hamiltonian for non-interacting electrons in a crystal, which will for now only include the potential due to the atomic sites and the kinetic energy of these electrons.

$$\hat{H} = \sum_i \frac{\hat{\mathbf{p}}_i^2}{2m_e} + V(\hat{\mathbf{r}}_i), \quad (1.1)$$

where  $\hat{\mathbf{p}}_i$  is the canonical momentum operator for electron  $i$ ,  $V(\hat{\mathbf{r}}_i)$  is the potential that it feels at its position  $\mathbf{r}_i$  and  $m_e$  is the mass of the electron.

## 1.1 Bloch Theorem

---

This atomic potential has a spatial dependence, but we can exploit its periodicity. Let us introduce the discrete translation operator  $\hat{T}(\mathbf{a})$  that transforms  $\mathbf{r} \mapsto \mathbf{r} + \mathbf{a}$ . This operator acts on quantum states  $|\psi'\rangle = \hat{T}(\mathbf{a})|\psi\rangle$ . In analogy of the classic counterpart, we want that the expectation value of the position operator in this new state gets changed by  $\mathbf{a}$ ,

$$\langle \psi' | \hat{\mathbf{r}} | \psi' \rangle = \langle \psi | \hat{T}^\dagger(\mathbf{a}) \hat{\mathbf{r}} \hat{T}(\mathbf{a}) | \psi \rangle = \langle \psi | \hat{\mathbf{r}} + \mathbf{a} \hat{1} | \psi \rangle, \quad (1.2)$$

with the normalization condition  $\langle \psi' | \psi' \rangle = \langle \psi | \psi \rangle$  implying that the translation operator is unitary,  $\hat{T}^\dagger(\mathbf{a}) \hat{T}(\mathbf{a}) = \hat{1}$ . From eq. (1.2) and the unitary condition, we find that

$$[\hat{\mathbf{r}}, \hat{T}(\mathbf{a})] = \mathbf{a} \hat{T}(\mathbf{a}). \quad (1.3)$$

From this commutation relation, we find that if  $|\mathbf{r}\rangle$  is the eigenstate of the position operator  $\hat{\mathbf{r}}$ ,

$$\hat{\mathbf{r}} \hat{T}(\mathbf{a}) |\mathbf{r}\rangle = \hat{T}(\mathbf{a}) \hat{\mathbf{r}} |\mathbf{r}\rangle + \mathbf{a} \hat{T}(\mathbf{a}) |\mathbf{r}\rangle = (\mathbf{r} + \mathbf{a}) \hat{T}(\mathbf{a}) |\mathbf{r}\rangle. \quad (1.4)$$

This means that  $\hat{T}(\mathbf{a}) |\mathbf{r}\rangle$  is an eigenstate of the position operator with eigenvalue  $(\mathbf{r} + \mathbf{a})$ . In other words,  $\hat{T}(\mathbf{a}) |\mathbf{r}\rangle = |\mathbf{r} + \mathbf{a}\rangle$ . This lets us find the effect of the adjoint operator on position eigenstates,

$$\hat{T}^\dagger(\mathbf{a}) \hat{T}(\mathbf{a}) |\mathbf{r}\rangle = \hat{T}^\dagger(\mathbf{a}) |\mathbf{r} + \mathbf{a}\rangle = |\mathbf{r}\rangle.$$

That is,

$$\hat{T}^\dagger(\mathbf{a}) |\mathbf{r}\rangle = |\mathbf{r} - \mathbf{a}\rangle \implies \langle \mathbf{r} | \hat{T}(\mathbf{a}) = \langle \mathbf{r} - \mathbf{a} |,$$

from which we can see that  $\hat{T}(\mathbf{a})$  is not a Hermitian operator since  $\hat{T}^\dagger(\mathbf{a}) = \hat{T}(-\mathbf{a})$ .

Now let us apply this operator on the Schrödinger equation of eigenvalues  $H|\psi\rangle = \epsilon|\psi\rangle$  with the Hamiltonian from eq. (1.1). It is easy to prove that our translation operator commutes with the Hamiltonian. Looking at the periodic potential,

$$\hat{T}^\dagger(\mathbf{a}) V(\mathbf{r}) \hat{T}(\mathbf{a}) = V(\mathbf{r} + \mathbf{a}) = V(\mathbf{r}), \quad (1.5)$$

we see the Hamiltonian will commute with the operator provided a translation commutes with the momentum operator. The fact that it does can be intuitively seen from the translation symmetry  $\leftrightarrow$  conservation of momentum. Mathematically, the translation operator can actually be expressed as,

$$\hat{T}(\mathbf{a}) = \exp\left(-\frac{i}{\hbar} \hat{\mathbf{p}} \cdot \mathbf{a}\right), \quad (1.6)$$

where  $\hat{\mathbf{p}}$  is the momentum operator. This way the Hamiltonian clearly commutes with the finite translation operator. Now we can use the commutation relation,  $[\hat{T}(\mathbf{a}), \hat{H}] = 0$  to construct a common eigenbasis for these two operators.

$$\hat{H} |\psi_{\mathbf{k}}\rangle = E_{\mathbf{k}} |\psi_{\mathbf{k}}\rangle \quad (1.7a)$$

$$\hat{T}(\mathbf{a}) |\psi_{\mathbf{k}}\rangle = \left(\frac{1}{p_{\mathbf{k}}}\right) |\psi_{\mathbf{k}}\rangle. \quad (1.7b)$$

Here  $\mathbf{k}$  is the quantum number that labels the states in the common eigenbasis. Using the periodic boundary conditions for the system, it is easy to prove that  $p_{\mathbf{k}} = e^{i\mathbf{k}\cdot\mathbf{a}}$  where  $\mathbf{k} = \frac{2\pi}{L}(n_x, n_y, n_z)$  (where we have used a cubic crystal of side  $L$ , and  $n_i$  is an integer). Thus we have,

$$\hat{T}(\mathbf{a}) |\psi_{\mathbf{k}}\rangle = e^{-i\mathbf{k}\cdot\mathbf{a}} |\psi_{\mathbf{k}}\rangle. \quad (1.8)$$

Or, in real space,

$$\psi_{\mathbf{k}}(\mathbf{r} + \mathbf{a}) = e^{i\mathbf{k}\cdot\mathbf{a}} \psi_{\mathbf{k}}(\mathbf{r}). \quad (1.9)$$

This last equation is known as the Bloch theorem. The eigenstates  $|\psi_{\mathbf{k}}\rangle$  of the Hamiltonian, if we consider spin (and for now  $[\hat{\sigma}_z, \hat{H}] = 0$ ), can also be expressed as

$$\langle r | \mathbf{k}, \sigma \rangle = \psi_{\mathbf{k}, \sigma}(\mathbf{r}) = e^{i\mathbf{k}\cdot\mathbf{r}} u_{\mathbf{k}, \sigma}(\mathbf{r}). \quad (1.10)$$

The resulting Bloch states differ from a plane wave solution only by a periodic modulation  $u_{\mathbf{k}}(\mathbf{r})$  that possesses the same period as the crystalline potential. In general, a dispersion relation  $E_n(\mathbf{k})$  will usually define a set of “energy bands”: for a fixed  $\mathbf{k}$ , we will have many different possible values for the eigenenergies due to internal degrees of freedom. These bands are thus labeled with the band index  $n$  and the Bloch states are denoted as  $|\mathbf{k}, n\rangle$ . These solutions can also reproduce “energy gaps”: energy intervals for which there are no states allowed. In Fig. (3.1), we see an example of this for the  $\text{Bi}_2\text{Se}_3$  crystal, obtained through a tight-binding approximation.

## 1.2 Band degeneracy

---

No matter what approximations we do in our system to obtain the previous bands, the symmetries of the crystal have profound implications on the eigenenergies and eigenstates of any Hamiltonian that can hope to represent the system. For now, we will drop the hats over the operators to lighten the notation, and we will come back to them when needed. Let

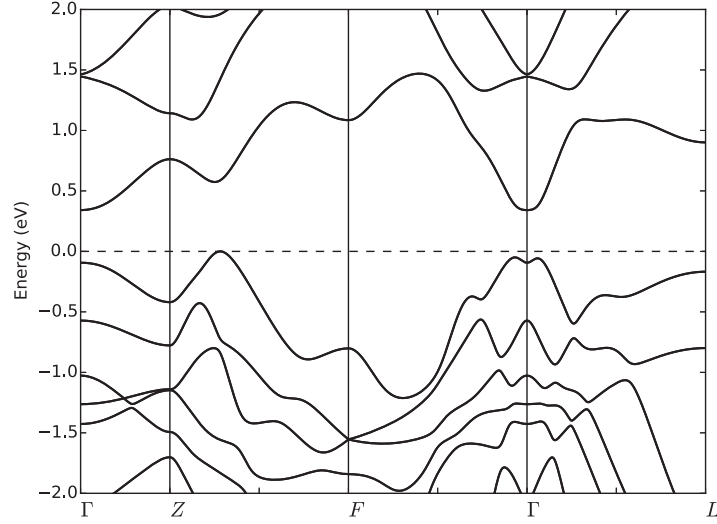


**Figure 1.1** Band structure of Bi<sub>2</sub>Se<sub>3</sub> as calculated with a tight-binding Hamiltonian. We see the energy dispersion relation as a function of different directions in  $\mathbf{k}$ -space. Around  $E(\mathbf{k}) = 0$  we see a band gap. Taken from [8].

$S$  be a symmetry of our single-particle Hamiltonian  $\mathcal{H}$ . Mathematically, we mean that the operator representation of this symmetry commutes with the Hamiltonian,

$$[\mathcal{H}, S] = 0.$$

In the context of statistical mechanics, we say  $S$  is a symmetry of the system when it commutes with the density matrix  $[\rho, S] = 0$ . The symmetry  $S$  is in general unitary or antiunitary, and we will see examples of this in this section. To extract information from the existence of a symmetry, we analyse what is the “action” on observables of the system. Thermal averages of an observable  $\mathcal{O}$  will not change when computed in a different basis obtained from applying the symmetry  $S$ . Because of the commutation with the density matrix, we can let the symmetry operations act on operators instead of on the basis functions, as in

$$\begin{aligned} \langle \mathcal{O} \rangle &= \text{Tr} [\rho \mathcal{O}] \\ &= \text{Tr} [S \rho S^{-1} \mathcal{O}] \\ &= \text{Tr} [\rho S^{-1} \mathcal{O} S], \end{aligned}$$

where we have used the cyclic property of the trace. Therefore, we get the important result that given  $S$  a symmetry, the thermal average of the transformed operator is the same as the

non-transformed,

$$\langle S^{-1} \mathcal{O} S \rangle = \langle \mathcal{O} \rangle. \quad (1.11)$$

We can thus look at what is the signature of the operator under the action of the symmetry. Throughout the rest of this chapter, we will focus on two basic symmetries that render every energy band of a non-magnetic crystal at least two-fold degenerate: inversion and time-reversal symmetries.

### 1.2.1 Inversion symmetry

In vectorial spaces, the parity operator is usually defined as the operator that flips a spatial coordinate. Throughout the rest of this mémoire, we will denote our parity operator as  $\Pi$ , which will flip all three spatial coordinates  $\hat{x}$ ,  $\hat{y}$  and  $\hat{z}$  and is usually called an inversion operation. Let us look at the effect of the inversion operation on certain observables.

Let us assume we know that our system is in a quantum state  $|\psi\rangle$ . Let us then apply the parity operator on this state  $\Pi |\psi\rangle = |\psi'\rangle$ . Evidently, we will ask that the norm is conserved,  $\langle \psi | \psi \rangle = \langle \psi' | \psi' \rangle = \langle \psi | \Pi^\dagger \Pi | \psi \rangle$ . Therefore, parity is a unitary operator,

$$\Pi^\dagger \Pi = 1. \quad (1.12)$$

Furthermore, we will ask by the very nature of the operator that flipping the flipped state takes us back to the original state (up to a phase factor),  $\Pi |\psi'\rangle = |\psi\rangle$ . In other words, that  $\Pi^2 = \hat{1}$ . Then, eq. (1.12) and this last condition imply

$$\begin{aligned} \Pi^\dagger \Pi \Pi &= \Pi \\ \Pi^\dagger &= \Pi. \end{aligned} \quad (1.13)$$

And thus the parity operator is Hermitian. Therefore, if we project a state onto real space,

$$\begin{aligned} \psi(-\mathbf{r}) &= \langle -\mathbf{r} | \psi \rangle = \langle \mathbf{r} | \Pi | \psi \rangle = \langle \mathbf{r} | \psi' \rangle \\ &= \psi'(\mathbf{r}). \end{aligned}$$

Therefore:

$$\langle \psi' | \hat{\mathbf{r}} | \psi' \rangle = - \langle \psi | \hat{\mathbf{r}} | \psi \rangle,$$

where  $\hat{\mathbf{r}}$  is the position operator. Finally, we have that

$$\Pi^\dagger \hat{\mathbf{r}} \Pi = -\hat{\mathbf{r}}. \quad (1.14)$$

When an observable changes sign under the action of a symmetry operation, we say that that observable is *odd* under that symmetry transformation. Therefore, position is odd under inversion, which could have been expected by the very definition of position. Now, another observable that we could be interested in is linear momentum  $\hat{p}$ . The position representation of momentum is  $\hat{p} = -i\hbar\nabla$ , where  $\nabla$  is the usual first-order differential operator. Because of this, it is easy to show that momentum is also odd under inversion.

$$\Pi^\dagger \hat{p} \Pi = -\hat{p}. \quad (1.15)$$

In general, any vector that changes sign under inversion will be denoted as *polar vectors* or *real vectors*. These include quantities such as: velocity, electric field, current density or the electromagnetic vector potential.

Nevertheless, there exists another class of observables that are even under inversion, they do not change sign under inversion. The most standard example is the angular momentum of a particle. This can easily be seen by the classical definition of angular momentum  $L$ ,

$$L = \mathbf{r} \times \mathbf{p}. \quad (1.16)$$

Since both  $\mathbf{r}$  and  $\mathbf{p}$  are polar vectors, they both will change sign under inversion, which means  $L$  will not. This in turn means that the parity operator and a given component  $i$  of the angular momentum operator commute,  $[\Pi, L_i] = 0$ . In quantum mechanics, any angular momentum operator such as spin  $\hat{S}$ , orbital  $\hat{L}$ , or general  $\hat{J}$  angular momenta, will be even under inversion.

Let us turn our attention towards the translation operator  $T(\mathbf{a})$ . The action of inversion on this operator can be obtained from eq. (1.6),

$$\Pi^\dagger T(\mathbf{a}) \Pi = \Pi^\dagger \exp\left(-\frac{i}{\hbar} \hat{p} \cdot \mathbf{a}\right) \Pi = \exp\left(\frac{i}{\hbar} \hat{p} \cdot \mathbf{a}\right) = T^\dagger(\mathbf{a}), \quad (1.17)$$

which implies that commutation leads to,

$$\Pi T(\mathbf{a}) = T^\dagger(\mathbf{a}) \Pi.$$

If we take the Bloch states (that are eigenstates of the translation operator) and start from this last equation,

$$\Pi T(\mathbf{a}) |\psi_k\rangle = \Pi e^{-ik \cdot \mathbf{a}} |\psi_k\rangle = e^{-ik \cdot \mathbf{a}} \Pi |\psi_k\rangle = T^\dagger(\mathbf{a}) \Pi |\psi_k\rangle.$$

Remembering that  $T^\dagger(\mathbf{a}) = T(-\mathbf{a})$ ,

$$T(\mathbf{a})\Pi|\psi_{\mathbf{k}}\rangle = e^{i\mathbf{k}\cdot\mathbf{a}}\Pi|\psi_{\mathbf{k}}\rangle. \quad (1.18)$$

We find out that  $\Pi|\psi_{\mathbf{k}}\rangle$  is an eigenstate of the translation operator with eigenvalue  $e^{i\mathbf{k}\cdot\mathbf{a}}$ .

Let us finally turn our attention at the Hamiltonian. We remember, from eq. (1.1), that the crystalline potential is the one that includes all symmetries. This means that, if  $V(-\hat{\mathbf{r}}) = V(\hat{\mathbf{r}})$ ,

$$\Pi^\dagger\mathcal{H}\Pi = \mathcal{H}, \quad (1.19)$$

because  $\Pi^\dagger\hat{\mathbf{p}}^2\Pi = \hat{\mathbf{p}}^2$ . We will refer to the fact that there exists a point in space from which  $V(-\hat{\mathbf{r}}) = V(\hat{\mathbf{r}})$  as the system being *centrosymmetric*. As we have seen, this means that the Hamiltonian commutes with parity,  $[\Pi, \mathcal{H}] = 0$ , and so parity is a symmetry of the Hamiltonian. Let us consider then the implication of the existence of this inversion symmetry on the eigenstates of  $\mathcal{H}$ . Let  $|\mathbf{k}, \sigma\rangle$  be the simultaneous eigenstate of the Bloch Hamiltonian eq. (1.1) and the translation operator  $T(\mathbf{a})$ . Then,

$$\mathcal{H}\Pi|\mathbf{k}, \sigma\rangle = \Pi E_{\mathbf{k}, \sigma}|\mathbf{k}, \sigma\rangle.$$

This finally means in other words that  $\Pi|\mathbf{k}, \sigma\rangle$  is then a simultaneous eigenstate of  $\mathcal{H}$ , with eigenvalue  $E_{\mathbf{k}, \sigma}$ ; and of  $T(\mathbf{a})$ , with eigenvalue  $e^{i\mathbf{k}\cdot\mathbf{a}}$ . We observe that  $T(\mathbf{a})|\mathbf{k}, \sigma\rangle = e^{-i\mathbf{k}\cdot\mathbf{a}}|\mathbf{k}, \sigma\rangle$ , just as in eq. (1.18), and thus,

$$\Pi|\mathbf{k}, \sigma\rangle = |-\mathbf{k}, \sigma\rangle$$

with eigenvalue  $E_{-\mathbf{k}, \sigma}$  for the Hamiltonian. Now that we know what is the action of inversion on our Bloch states, we find that the energies for a given  $\sigma$  at opposite  $\mathbf{k}$  have to be the same,

$$E_{\mathbf{k}, \sigma} = E_{-\mathbf{k}, \sigma}. \quad (1.20)$$

### 1.2.2 Time-reversal operator

Time-reversal symmetry is a stranger kind of symmetry. The idea is that whatever the description of a system, by reversing time  $t \rightarrow -t$ , an observer should not be able to tell the difference in the description of the dynamical system. In the quantum case, we describe our system by the Schrödinger equation, in the case where we are not considering spin,

$$H\psi(t) = i\hbar\frac{\partial}{\partial t}\psi(t), \quad (1.21)$$

where  $H$  is a time-independent Hamiltonian. If we reverse time,  $\psi(-t)$  would not be a solution due to the first derivative respect to time. However, if we complex conjugate,

$$H\psi^*(t) = -i\hbar \frac{\partial}{\partial t} \psi^*(t),$$

then reversing time would render  $\psi^*(-t)$  a solution of the Schrödinger equation. The time-reversal state will be defined as  $\Theta\psi(t) = \psi^*(-t)$ , where  $\Theta$  is the time-reversal operator. This means that for the case with no spin, the time reversal operator consists of just taking the complex conjugate *to the right*. This last remark is important when dealing with de Dirac notation due to the fact that we are dealing with complex conjugation. This means that for now we will express  $\Theta$  as the complex conjugation to the right  $\underline{K}$ . In general, time-reversal is an *antiunitary* operator. This means it is an antilinear and unitary operator. The action of an antilinear operator  $\Theta$  on a linear combination is different than the one of a normal, linear unitary one,

$$\Theta(a|\psi\rangle + b|\gamma\rangle) = a^*\Theta|\psi\rangle + b^*\Theta|\gamma\rangle, \quad (1.22)$$

where  $*$  denotes complex conjugation of the coefficients. We see that  $\underline{K}$  complies with antilinearity and we ask that the norm is preserved. We note that under time reversal any arbitrary matrix element preserves its norm but not its phase:

$$\langle\psi|\underline{K}\underline{K}|\gamma\rangle = \langle\gamma|\psi\rangle \neq \langle\psi|\gamma\rangle.$$

For now, time reversal is only about taking the complex conjugate. However, when we consider spin, we would like that it transforms under time-reversal just like any angular momentum. In other words, if we look at the classical orbital angular momentum  $\mathbf{L} = \mathbf{r} \times \mathbf{p}$ , when we reverse time,  $\mathbf{L} \rightarrow -\mathbf{L}$  since  $\mathbf{r}$  does not change and  $\mathbf{p}$  does. Using for now that  $\Theta$  takes complex conjugate to the right, we can see the fact that  $\mathbf{p}$  changes sign from either the quantum case  $\Theta(-i\hbar\nabla) = (i\hbar\nabla)\Theta$ ; or a classical case, in which  $\mathbf{p} = m\mathbf{v}$ , and thus by reversing time,  $\Theta\mathbf{p} = -\mathbf{p}\Theta$ .

To find the explicit expression of  $\Theta$  when it acts on spin states, let us express it as complex conjugation times a unitary transformation  $U$ , preserving its anti-unitary nature. Let us now compute expectation values of an operator  $\mathcal{O}$  in times-reversed states.

$$\begin{aligned} \langle\psi|U^\dagger\underline{K}\mathcal{O}\underline{K}U|\gamma\rangle &= (\langle\psi|U^\dagger\underline{K})(\underline{K}\mathcal{O}^*U|\gamma\rangle) \\ &= (\langle\psi|U^\dagger\mathcal{O}^*U|\gamma\rangle)^* \\ &= \langle\gamma|U^\dagger\mathcal{O}^{\dagger*}U|\psi\rangle, \end{aligned}$$

where  $\mathcal{O}^{\dagger*} = \mathcal{O}^T$  is just the transpose. We have then shown that computing expectation

values with time-reversed states is equivalent to computing equilibrium traces of  $U^\dagger \mathcal{O}^T U$  in the normal basis. Therefore, by imposing the action on spin  $\sigma$ ,

$$U^\dagger \sigma^T U = -\sigma \quad (1.23)$$

we will find the explicit form of  $U$  that will depend on the choice of basis for spin. Using Pauli matrices we find that

$$\begin{aligned} U^\dagger \sigma_x U &= -\sigma_x \\ U^\dagger (-\sigma_y) U &= -\sigma_y \\ U^\dagger \sigma_z U &= -\sigma_z. \end{aligned}$$

These equations plus the Pauli matrices properties imply that the form of the unitary transformation follows  $U = e^{i\delta} \sigma_y$ , and thus,

$$\Theta = \underline{K} e^{i\delta} \sigma_y, \quad (1.24)$$

where  $\delta$  is an arbitrary real phase. Then let us find the time-reversed spin states.

$$\Theta |\uparrow\rangle = -ie^{-i\delta} |\downarrow\rangle \quad (1.25a)$$

$$\Theta |\downarrow\rangle = ie^{-i\delta} |\uparrow\rangle, \quad (1.25b)$$

where  $|\sigma\rangle$  are the eigenstates of the quantized z-projection of spin. Choosing  $e^{-i\delta} = i$  to make the phase factor real, we see that reversing time changes up-spin to down-spin and viceversa. Moreover, we get the ‘‘strange’’ result that  $\Theta\Theta |\uparrow\rangle = -|\uparrow\rangle$ . This stems from the general antiunitary property of the time-reversal operator  $\Theta^2 = -1$  that applies to half-integer spins.

### 1.2.3 Kramers theorem

Let us consider our time-reversal-invariant Hamiltonian  $\mathcal{H}$ , eq. (1.1). Using then  $[\Theta, \mathcal{H}] = 0$  and  $[\Theta, T(\mathbf{a})] = 0$ , the time-reversal state  $|\tilde{\psi}_k\rangle = \Theta |\psi_k\rangle$  is also an eigenstate of the Hamiltonian with the same energy  $E_k$ . However,

$$T(\mathbf{a}) |\tilde{\psi}_k\rangle = \Theta T(\mathbf{a}) |\psi_k\rangle = \Theta (e^{-ik \cdot \mathbf{a}} |\psi_k\rangle) = e^{ik \cdot \mathbf{a}} \Theta |\psi_k\rangle = e^{ik \cdot \mathbf{a}} |\tilde{\psi}_k\rangle \quad (1.26)$$

tells us that  $\Theta |\psi_k\rangle = |\tilde{\psi}_k\rangle$  coincides with  $|\psi_{-k}\rangle$ , whose Hamiltonian eigenvalue is  $E_{-k}$ . Therefore, ignoring spin for now, the time-reversal symmetry tells us that the Bloch states

$|\psi_{-k}\rangle$  and  $|\psi_k\rangle$  are degenerate, and thus,

$$E_k = E_{-k}. \quad (1.27)$$

Let us consider eigenstates  $|\sigma\rangle$  of the 1/2 electronic spin  $\sigma_z$ -operator. The full Bloch states will just be a tensor product  $|\mathbf{k}, \sigma\rangle = |\mathbf{k}\rangle \otimes |\sigma\rangle$ . Using the last result along with eqs. (1.25),

$$H\Theta |\mathbf{k}, \sigma\rangle = \Theta H |\mathbf{k}, \sigma\rangle = \Theta E_{k,\sigma} |\mathbf{k}, \sigma\rangle = E_{k,\sigma} |-\mathbf{k}, -\sigma\rangle. \quad (1.28)$$

This tells us that

1.  $\Theta |\mathbf{k}, \sigma\rangle \rightarrow |-\mathbf{k}, -\sigma\rangle$  is an eigenstate of  $H$  with eigenvalue  $E_{k,\sigma}$ .
2. However,  $|-\mathbf{k}, -\sigma\rangle$  is by construction an eigenstate of  $H$  with eigenvalue  $E_{-k,-\sigma}$ .

We do not use the equal sign because it is equal modulo a global phase factor, as can be verified from eq. (1.25). This last equation implies that  $E_{k,\sigma} = E_{-k,-\sigma}$ . But most importantly  $\Theta |\mathbf{k}, \sigma\rangle$  and  $|\mathbf{k}, \sigma\rangle$  are truly different states. In fact, they are orthogonal states, which can be proven easily given the antiunitary nature of the time-reversal operator. These two facts are the content of the Kramers theorem.

#### 1.2.4 Double degeneracy

We have proven that when the system respects inversion and time-reversal symmetries, and spin is a good quantum number,

1.  $E_{k,\sigma} = E_{-k,\sigma}$ .
2.  $E_{k,\sigma} = E_{-k,-\sigma}$ .

In consequence, for every  $\mathbf{k}$ , there are two associated eigenstates that render every band doubly degenerate:  $E_{k,\sigma} = E_{k,-\sigma}$ .

This holds true even in the presence of spin-orbit interaction. The origin of spin-orbit interactions in crystals arises from the spatial dependence of the crystal potential. This generates an effective electric field that electrons in the crystal feel. This in turn means that the electron feels an effective magnetic field in its rest frame. To calculate this effect, it is necessary to consider the relativistic contributions to the Schrödinger equation. In

other words, we have to start from the Dirac equation. When one does this, an additional contribution to the single-electron Hamiltonian appears, eq. (1.1),

$$\mathcal{H} = \frac{\mathbf{p}^2}{2m_e} + V(\mathbf{r}) + \frac{\hbar}{4m_e^2c^2} \boldsymbol{\sigma} \cdot (\nabla V \times \mathbf{p}), \quad (1.29)$$

where  $c$  is the speed of light. The relative strength of the spin orbit coupling will be determined by the magnitude of  $|\nabla V|$ , that depends on the atomic details of the crystal. To see how this additional term can be explicitly an interaction between spin and orbital degrees of freedom, let us consider a Hydrogen-like atom potential. This means that

$$\begin{aligned} \frac{\hbar}{4m_e^2c^2} \boldsymbol{\sigma} \cdot (\nabla V \times \mathbf{p}) &= \frac{Ze^2}{2m_e^2c^2r^3} \mathbf{S} \cdot (\mathbf{r} \times \mathbf{p}) \\ &= \lambda(r) \mathbf{S} \cdot \mathbf{L}, \end{aligned}$$

where  $\mathbf{S} = \frac{\hbar}{2} \boldsymbol{\sigma}$ . The numerical details of the spin-orbit interaction are included in  $\lambda(r)$ . We note however that the orbital angular momentum operator  $\mathbf{L}$  would be ill-defined for an infinite arrangement of atoms, since it depends on the choice of origin. This critical detail is discussed in the models to follow.

The new SOC Hamiltonian, eq. (1.29), is still time-reversal invariant *and* inversion invariant. The former can be seen from the fact that both the spin and momentum operator are odd under time reversal, and the latter because the potential gradient and the momentum operator are both odd under inversion symmetry. The presence of both symmetries still protects the at-least double degeneracy of bands everywhere in reciprocal space, but now there are no pure spin-states due to the  $\mathbf{L} \cdot \mathbf{S}$  term.

### 1.3 Hidden spin polarization

---

We have seen what is the action of the time-reversal and inversion operation on degenerate Bloch states,

$$\Pi |\mathbf{k}, n\rangle \rightarrow |-\mathbf{k}, n\rangle \quad (1.30a)$$

$$\Theta |\mathbf{k}, m\rangle \rightarrow |-\mathbf{k}, n\rangle, \quad (1.30b)$$

where  $m \neq n \in \{1, 2\}$  are the two bands that live in this degenerate band subspace. This means that, given the composition of symmetries  $\Theta \Pi |\mathbf{k}, 1\rangle = e^{i\delta} |\mathbf{k}, 2\rangle$ , we can evaluate the

expectation value of the spin operator in this degenerate subspace at a particular value of  $k$ ,

$$\begin{aligned} \mathbf{S}_k &= \sum_{n' \in \text{deg}\{n\}} \langle k, n' | \frac{\sigma}{2} | k, n' \rangle = \langle k, 1 | (\Theta\Pi)^\dagger \frac{\sigma}{2} (\Theta\Pi) | k, 1 \rangle + \langle k, 2 | (\Theta\Pi)^\dagger \frac{\sigma}{2} (\Theta\Pi) | k, 2 \rangle \\ &= \langle k, 2 | \frac{\sigma}{2} | k, 2 \rangle + \langle k, 2 | (-\frac{\sigma}{2}) | k, 2 \rangle \\ &= 0 \end{aligned}$$

for all wavevectors  $k$ . For the first band, we acted the symmetry operations on the states and on the second one we acted them on the spin operator. It is important to take the expectation value over the two bands because of their degeneracy.

The possible study of spin polarization on centrosymmetric crystals has been overlooked due to this last equation. In a recent paper [1], however, it is suggested that by looking at real-space projected sectors of the spin operator we could find a non-zero expectation value for positions other than the inversion center. Mathematically, if we look at the expectation value over the two bands of

$$\hat{\mathbf{S}}(\mathbf{r}) = \frac{\sigma}{2} |\mathbf{r}\rangle\langle\mathbf{r}|, \quad (1.31)$$

then, we get,

$$\begin{aligned} \mathbf{S}_k(\mathbf{r}) &= \sum_{n' \in \text{deg}\{n\}} \langle k, n' | \hat{\mathbf{S}}(\mathbf{r}) | k, n' \rangle \\ &= \langle k, 1 | (\Theta\Pi)^\dagger \hat{\mathbf{S}}(\mathbf{r}) (\Theta\Pi) | k, 1 \rangle + \langle k, 2 | (\Theta\Pi)^\dagger \hat{\mathbf{S}}(\mathbf{r}) (\Theta\Pi) | k, 2 \rangle \\ &= \langle k, 2 | \hat{\mathbf{S}}(\mathbf{r}) | k, 2 \rangle - \langle k, 2 | \hat{\mathbf{S}}(-\mathbf{r}) | k, 2 \rangle, \end{aligned}$$

which is in general non-zero. We have come back to the hat notation to differentiate between operators and expectation values. This  $\mathbf{S}_k(\mathbf{r}) \neq 0$  is what we call the hidden spin polarization, and we will see the reason why it is *hidden*.

The inversion operator acts on the real-space projection and gives us the projection of spin at the inverted position relative to the inversion center. This has two main consequences, due to inversion and time-reversal symmetries, respectively:

$$\mathbf{S}_k(\mathbf{r}) = \mathbf{S}_k(-\mathbf{r}) \quad \text{for all } k. \quad (1.32a)$$

$$\mathbf{S}_k(\mathbf{r}) = \mathbf{S}_{-k}(\mathbf{r}) \quad \text{for all } \mathbf{r}. \quad (1.32b)$$

This leads to a *hidden* spin polarization in both reciprocal and real space:

1.  $\mathbf{S}_k = \int d^3r \mathbf{S}_k(\mathbf{r}) = 0$  (no spin texture).

2.  $\mathbf{m}(\mathbf{r}) = \sum_{\mathbf{k}} \mathbf{S}_{\mathbf{k}}(\mathbf{r}) f_{\mathbf{k}} = 0$  (no local magnetic moment).

Where  $f_{\mathbf{k}}$  is the Fermi-Dirac distribution. The local magnetic moment is a quantity we define that depends on both  $\mathbf{S}_{\mathbf{k}}(\mathbf{r})$  and the population of states at wavevector  $\mathbf{k}$ . If we could change this population to give certain states  $\mathbf{k}$  close to the Fermi energy more weight than others, we could drive this magnetic moment  $\mathbf{m}(\mathbf{r})$  to a non-zero value. One way to do this is using an external electric field. This could lead to a nonzero local magnetization that is otherwise compensated within a unit cell due to eqs. (1.32). Therefore, there is no macroscopic magnetization. However, there could still be a nonzero *staggered* magnetization within a unit cell,

$$\mathbf{m}(\mathbf{r}) = -\mathbf{m}(-\mathbf{r}), \quad (1.33)$$

which constitutes an effective magnetoelectric effect that could be potentially used for spintronics applications. In the following chapter we propose nuclear magnetic resonance as a potential new probe for this effect. Before we come to that, we discuss the *orbital* electronic polarization that is a consequence of a local inversion symmetry breaking.

## 1.4 Inversion-symmetry breaking

---

In the previous section, we have discussed how the presence of time-reversal symmetry precludes the appearance of crystal magnetization and, together with inversion symmetry, protects the double degeneracy of bands everywhere, in particular in relation to electronic spin. However, there is a known effect that appears at the surfaces of crystals, where the inversion symmetry is explicitly broken. This phenomenon is known as Rashba effect. This effect describes the spin-splitting of bands at certain positions in the Brillouin zone due to the spin-orbit interaction, and is due to Rashba in a series of 2 papers in 1959 [9]. The well-known effect features a chiral spin texture of the surface bands that can be exploited to develop technological devices in the context of spintronics [7]. This chiral spin texture is observed as well on the spin-polarized surface states of topological insulators [10]. In 2012, it was shown that there is an orbital texture present when inversion symmetry is broken at a surface, and thus the conventional Rashba effect is just a consequence of this when spin-orbit interactions are important [11]. In this section, we develop one of the calculations presented in ref. [11] to show how inversion-symmetry breaking leads to a non-zero orbital angular momentum. This will be important in the following section when we treat site-symmetry groups that do not contain inversion.

We leap to second quantization notation, in which we introduce fermion creation (and annihilation) operators  $c_n^\dagger$  ( $c_n$ ), where  $n$  is a collection of quantum numbers that label states that stem from our single-particle Hamiltonian. Thus  $c_n^\dagger$  ( $c_n$ ) creates (annihilates) an electronic state  $|n\rangle$ . Therefore, operators act on quantum states that live in the Fock space, which is the direct sum of Hilbert spaces of 1, 2, ...,  $n$  number of particles. Of course, our number of particles  $n$  is conserved and thus there always has to be the same number of creation and annihilation operators. Working on this *occupation* representation lets us treat the many-body state and operators more intuitively. The creation and annihilation operators follow fermionic anticommutation relations,

$$\{c_n, c_{n'}^\dagger\} = \delta_{n,n'} \quad \{c_n, c_{n'}\} = \{c_n^\dagger, c_{n'}^\dagger\} = 0.$$

In this notation, it is easier to understand the tight-binding Hamiltonian. This approach introduces the full Hamiltonian  $H$ , and particularly the crystal potential  $V(\mathbf{r})$ , through a series of hopping terms that can be understood as energy costs (or gains) for electrons to go from one lattice site to another. This approximation is born from considering the electrons to be tightly bound to their respective sites – thus its name. It is somewhat the opposite approach of the one usually seen in undergraduate courses, known as nearly-free electron Hamiltonian. A typical tight-binding Hamiltonian in the second-quantization notation looks like

$$H = \sum_{\langle i,j \rangle} \sum_{\mu',\mu} (t_{\mu,\mu'}^{i,j} c_{i,\mu}^\dagger c_{j,\mu'} + t_{\mu',\mu}^{j,i} c_{j,\mu'}^\dagger c_{i,\mu}), \quad (1.34)$$

where  $i \neq j$  are lattice site indices,  $\langle i,j \rangle$  indicates that the sum is allowed to be nonzero if  $i, j$  are nearest neighbours and  $\mu, \mu'$  hide all the internal degrees of freedom such as orbital or spin angular momenta. The  $t$  terms are the “hopping” integrals that contain all the information about the kinetic terms and the crystal potential,

$$t_{\mu,\mu'}^{i,j} = \langle i, \mu | H | j, \mu' \rangle. \quad (1.35)$$

Finally, as described above,  $c_{i,\mu}$  ( $c_{i,\mu}^\dagger$ ) is the annihilation (creation) operator of electron at site  $i$  and with internal degrees of freedom  $\mu$ . The standard way to diagonalize this Hamiltonian is by expanding these real-space operators in terms of momentum-space operators,

$$c_{i,\mu} = \frac{1}{\sqrt{N}} \sum_{\mathbf{k}} e^{i\mathbf{k}\cdot\mathbf{r}_i} c_{\mathbf{k},\mu}, \quad (1.36)$$

where  $N$  is the number of sites and  $\mathbf{k}$  is the wavevector. Since we have seen that  $\mathbf{k}$  is a good quantum number that diagonalizes the Hamiltonian, we see that indeed our tight-binding

Hamiltonian is diagonal in this basis,

$$H = \frac{1}{N} \sum_{\mu, \mu'} \sum_{\langle i, j \rangle} \sum_{\mathbf{k}, \mathbf{k}'} t_{\mu', \mu}^{j, i} e^{i\mathbf{k} \cdot \mathbf{r}_i} e^{-i\mathbf{k}' \cdot \mathbf{r}_j} c_{\mathbf{k}, \mu'}^\dagger c_{\mathbf{k}', \mu} + h.c., \quad (1.37)$$

where  $h.c$  denotes the Hermitian conjugate of the previous expression. Since  $i$  and  $j$  are nearest neighbours, we can express  $\mathbf{r}_j = \mathbf{r}_i + \mathbf{n}_{i, j}$  and express the sum over  $i$  and  $j$  as a sum over  $i$  and the nearest neighbours of  $i$ . Let us then perform the sum over  $i$  by remembering that

$$\frac{1}{N} \sum_i e^{i(\mathbf{k} - \mathbf{k}') \cdot \mathbf{r}_i} = \delta_{\mathbf{k}', \mathbf{k}} \quad (1.38)$$

and the fact that the hopping amplitude does not really depend on the label site  $i$ , but will depend on the nearest neighbour positions. We have therefore

$$H = \sum_{\mathbf{k}} \sum_{\mu, \mu'} \sum_{\mathbf{n}} t_{\mu', \mu}^{\mathbf{n}} e^{-i\mathbf{k} \cdot \mathbf{n}} c_{\mathbf{k}, \mu'}^\dagger c_{\mathbf{k}, \mu} + h.c. \quad (1.39)$$

Our tight-binding Hamiltonian is diagonal in  $\mathbf{k}$ . The matrix elements  $t_{\mu', \mu}^{\mathbf{n}} = \langle \mu | H | \mu' \rangle$  will give us all the physics.

#### 1.4.1 Angular dependence of the orbital hopping

So why does the hopping amplitude depend on the nearest neighbour label? We will be handling a basis of local atomic orbitals, and in general there can be a directional hopping if the orbitals that we are using have a non-uniform spatial dependence. The minimal orbital basis set that contains nontrivial orbital information is the basis for  $l = 1$ . We will expand the atomic orbital eigenstates in terms of real  $p_x$ ,  $p_y$  and  $p_z$  orbitals. So how do the hopping amplitudes look like? We use Slater-Koster parameters [12] for the angular dependence of the hopping. The system that we are interested in lies in a surface, and thus our Hamiltonian describes a two-dimensional lattice of atoms. For the moment, we go back to the  $i, j$  notation,

$$\langle p_{x, i} | H | p_{x, j} \rangle = -V_1 \cos^2(\theta_{ij}) + V_2 \sin^2(\theta_{ij}) \quad (1.40a)$$

$$\langle p_{x, i} | H | p_{y, j} \rangle = \langle p_{y, i} | H | p_{x, j} \rangle = (V_2 - V_1) \cos(\theta_{ij}) \sin(\theta_{ij}) \quad (1.40b)$$

$$\langle p_{y, i} | H | p_{y, j} \rangle = -V_1 \sin^2(\theta_{ij}) + V_2 \cos^2(\theta_{ij}) \quad (1.40c)$$

$$\langle p_{z, i} | H | p_{z, j} \rangle = V_2, \quad (1.40d)$$

where, remembering that we are in two dimensions,

$$(\cos(\theta_{ij}), \sin(\theta_{ij})) = (x_{ij}, y_{ij}) / \sqrt{x_{ij}^2 + y_{ij}^2} \quad (1.41)$$

are the directional cosine and sine of the vector that goes from atom  $i$  to  $j$ .

We note that in the literature there exists another label for the  $p$ -orbital hopping amplitude basis  $V_1$  and  $V_2$ , which are  $pp\sigma = -V_1$  and  $pp\pi = -V_2$ . For more information about where these terms come from, we refer to Ref. [13].

Now, if the 2D system were isolated, there would be a zero hopping from  $p_x$  and  $p_y$  to the  $p_z$  orbital, due to inversion symmetry. That is, there would be an equally large overlap of a  $p_x$  or  $p_y$  lobe with the positive and negative  $p_z$  lobe, resulting in zero total overlap. To introduce the breaking of inversion symmetry by a real surface, the authors of Ref. [11] (and, originally, those from Ref. [14]), consider a finite hopping between the surface orbitals and the  $p_z$  orbital,

$$\langle p_{z,i} | H | p_{x,j} \rangle = \frac{3}{2} \gamma \cos(\theta_{ij}) = - \langle p_{x,i} | H | p_{z,j} \rangle \quad (1.42a)$$

$$\langle p_{z,i} | H | p_{y,j} \rangle = \frac{3}{2} \gamma \sin(\theta_{ij}) = - \langle p_{y,i} | H | p_{z,j} \rangle, \quad (1.42b)$$

where  $\gamma$  will be a measure of inversion-symmetry breaking. Since  $\theta_{ij}$  is the angle that the vector  $\vec{n}$  (which lives in the  $x - y$  plane) forms with the  $x$ -axis, we confirm the angular dependence of this hopping.

#### 1.4.2 Spinless, matrix Hamiltonian on a square lattice

For the following problem, we will neglect the spin degree of freedom, and thus orbital angular momentum is a good atomic quantum number. We will use a square lattice, so we can perform the sum over nearest neighbours more easily. Therefore, using eqs. 1.40, we see for example that

$$\sum_{\vec{n}} t_{p_x p_y}^{\vec{n}} e^{i\vec{k} \cdot \vec{n}} = 0, \quad (1.43)$$

since for this hopping, we have the product  $\cos(\theta) \sin(\theta)$ , which is zero for our nearest neighbours that sit on a square lattice:  $\theta \in \{0, \pi/2, \pi, 3\pi/2\}$ . Performing all the sums like

this one, we get a matrix Hamiltonian of the form:

$$H = \sum_{\vec{k}} c_{\vec{k}}^{\dagger} \begin{pmatrix} 2(V_2 \cos(k_y) - V_1 \cos(k_x)) & 0 & -3\gamma i \sin(k_x) \\ 0 & 2(V_2 \cos(k_x) - V_1 \cos(k_y)) & -3\gamma i \sin(k_y) \\ 3\gamma i \sin(k_x) & 3\gamma i \sin(k_y) & 2V_2(\cos(k_x) + \cos(k_y)) \end{pmatrix} c_{\vec{k}},$$

where we are expressing the creation and annihilation operators as spinors.

$$c_{\vec{k}} = \begin{pmatrix} p_{x,\vec{k}} \\ p_{y,\vec{k}} \\ p_{z,\vec{k}} \end{pmatrix} = \frac{1}{\sqrt{N}} \sum_i e^{-i\vec{k}\cdot\vec{r}_i} \begin{pmatrix} p_{x,i} \\ p_{y,i} \\ p_{z,i} \end{pmatrix} \quad (1.44)$$

and  $p_{l,i}$  is an annihilation operator of a  $p$  orbital ( $l \in \{x, y, z\}$ ) at site  $i$ .

In the hopes of having analytic expressions for the bands, let us consider the low energy spectrum,  $ka \ll 1$  ( $a = 1$ )

$$H_{\Gamma} = \sum_{\vec{k}} c_{\vec{k}}^{\dagger} \begin{pmatrix} 2(V_2 - V_1) & 0 & -3\gamma i k_x \\ 0 & 2(V_2 - V_1) & -3\gamma i k_y \\ 3\gamma i k_x & 3\gamma i k_y & 4V_2 \end{pmatrix} c_{\vec{k}}, \quad (1.45)$$

where  $H_{\Gamma}$  is the Hamiltonian around  $k = \Gamma$ . Diagonalizing this Hamiltonian gives us the following eigenenergies:

$$E_1(\mathbf{k}) = 2(V_2 - V_1) \quad (1.46a)$$

$$E_2(\mathbf{k}) = 2(V_2 - V_1) - \frac{9\gamma^2 k^2}{2\Delta} \quad (1.46b)$$

$$E_3(\mathbf{k}) = 4V_2 + \frac{9\gamma^2 k^2}{2\Delta}, \quad (1.46c)$$

where  $k = |\mathbf{k}|$ ,  $\Delta = V_1 + V_2$  and we have used the fact that  $\gamma k \ll \Delta$ . We note that if  $\gamma = 0$ , band 1 and 2 would be degenerate, which we can see from the matrix Hamiltonian. The

eigenvectors are

$$|\mathbf{k}, 1\rangle = \frac{k_y}{k} |p_x\rangle - \frac{k_x}{k} |p_y\rangle \quad (1.47a)$$

$$|\mathbf{k}, 2\rangle = \frac{k_x}{k} |p_x\rangle + \frac{k_y}{k} |p_y\rangle - \frac{3i\gamma k}{2\Delta} |p_z\rangle \quad (1.47b)$$

$$|\mathbf{k}, 3\rangle = |p_z\rangle - \frac{3i\gamma k}{2\Delta} \left( \frac{k_x}{k} |p_x\rangle + \frac{k_y}{k} |p_y\rangle \right). \quad (1.47c)$$

### 1.4.3 Calculating orbital angular momentum

As we know, the orbital angular momentum depends critically on the choice of origin, and renders computations ill-defined when studying an infinite crystal that has a discrete translational symmetry. However, we can define an average Orbital Angular Momentum that is translationally invariant and which is defined from the atomic orbital angular momentum operators. Here we show that, for certain bands, we obtain a nonzero expectation value for this operator that is expressed as

$$\mathbf{L} = \frac{1}{N} \sum_i \mathbf{L}_i. \quad (1.48)$$

$\mathbf{L}_i$  is the atomic orbital angular momentum operator with the origin at the atomic site  $\mathbf{r}_i$ . For band 2, for example,

$$\langle \mathbf{k}, 2 | \mathbf{L} | \mathbf{k}, 2 \rangle = \left( \frac{k_x}{k} \langle p_x | + \frac{k_y}{k} \langle p_y | + \frac{3i\gamma k}{2\Delta} \langle p_z | \right) \mathbf{L} \left( \frac{k_x}{k} | p_x \rangle + \frac{k_y}{k} | p_y \rangle - \frac{3i\gamma k}{2\Delta} | p_z \rangle \right). \quad (1.49)$$

We remember that the operator  $L_i$  acts on real orbitals and in real space. The matrix representation in the basis of real  $p$  orbitals for the atomic OAM operator is

$$L_x = -i\hbar \begin{pmatrix} 0 & 0 & 0 \\ 0 & 0 & 1 \\ 0 & -1 & 0 \end{pmatrix}, \quad L_y = -i\hbar \begin{pmatrix} 0 & 0 & -1 \\ 0 & 0 & 0 \\ 1 & 0 & 0 \end{pmatrix}, \quad L_z = -i\hbar \begin{pmatrix} 0 & 1 & 0 \\ -1 & 0 & 0 \\ 0 & 0 & 0 \end{pmatrix}, \quad (1.50)$$

and hereafter  $\hbar = 1$ . We find a non-zero chiral OAM for two of the bands, and we visualize it through  $L^+ = L_x + iL_y$ ,

$$\langle \mathbf{k}, 2 | L^+ | \mathbf{k}, 2 \rangle = \frac{3i\gamma}{\Delta} (k_x + ik_y) = -\langle \mathbf{k}, 3 | L^+ | \mathbf{k}, 3 \rangle. \quad (1.51)$$

And finally band 1 shows no OAM  $\langle \mathbf{k}, 1 | L^+ | \mathbf{k}, 1 \rangle = 0$ . We can draw some conclusions from this calculation:

- The *net* OAM is zero for all  $\mathbf{k}$  in the Brillouin zone:  $\sum_n \langle \mathbf{k}, n | L | \mathbf{k}, n \rangle = 0$ . This reminds us of the *hidden* polarization related to spin: there is a band orbital polarization that is compensated by another band.
- The OAM is proportional to the inversion-symmetry breaking term: if there was no inversion-symmetry breaking, there would not be any individual band polarization.
- In the case of small spin-orbit coupling, we can perturbatively include spin and see that a “hidden” non-zero spin angular momentum arises and it is a direct consequence of OAM [11, 2]. One recovers exactly the Rashba-type spin splitting as induced by spin-orbit interaction.

In our main calculations for the orbital degree of freedom, we will exploit our knowledge of the hidden spin polarization and the fact that there is an individual band OAM texture to look at a “real-space projection” of the orbital currents. This will lead to a non-zero orbital polarization of electrons that will have an influence on the nuclear magnetic resonance spectrum.

## 1.5 Crystallographic space and point groups

---

In the previous section, we have seen that a local inversion symmetry breaking, that happens for example at a surface, can lead to both a nonzero orbital and spin angular momentum across bands. This is the essential ingredient of the hidden electronic polarizations that we will study in this *mémoire*. In this section, we introduce the notion of the classification of crystals as a function of the discrete symmetries present in their structures. To do this, we look at the symmetries of the unit cell: the minimal repeating unit that contains all the symmetries of the full crystal. We remember that the unit cell is a unit such that by applying the translational unit vectors we can reproduce the whole crystal. The symmetry transformations that render a lattice unchanged form a group. A set of elements + an operation (that we will call product for convenience) form a group when 4 characteristics happen [15]:

1. The product of any two elements of the group is itself an element of the group.

2. The elements of the group associate.
3. There exists an identity  $E$  that leaves any other element invariant under the product.
4. For every element  $A$  of the group, there exists an inverse  $B$  such that  $AB = BA = E$ .

When we talk about crystals, we will always refer to symmetry groups.

### 1.5.1 Point groups

Excluding translation, there are three fundamental types of spatial symmetry transformations that can leave a given lattice point within a unit cell invariant: rotations, reflections across mirror planes and inversion. A point group of a crystal is the group of all symmetry operations that leave *at least one* point invariant. This includes the composition of them, as stated in item 1 of the definition of group. There exist 32 possible 3D point groups that can be found in any standard group theory book. If a point group contains inversion, we will call it a *centrosymmetric* crystal. There exist 11 centrosymmetric point groups, and this *mémoire* centers on them.

### 1.5.2 Space groups

However, the unit cell of a crystal can be quite complicated and contains many types of inequivalent sites inside, such as physically different atoms or sites that cannot be related by a symmetry transformation of the crystal, and thus change the properties of the Hamiltonian. As such, to physically classify a 3D crystal, we refer to the crystallographic space group. In the definition of these groups, we admit the use of translation operations. We can thus restore the full symmetry of the crystal that is described in the single-electron Bloch Hamiltonian eq. (1.1), which is invariant under lattice vector translations. Space group symmetry operations have the following usual notation

$$\{R_\alpha|\tau\},$$

where  $R_\alpha$  is a point-group operation (rotation, reflection, inversion or a composition of them) and  $\tau$  is a pure translation operation. Pure rotations and pure translations are special cases of space group operations:  $\{R_\alpha|0\}$  and  $\{0|\tau\}$ , respectively. Additionally, we can define the product of space group operations as separately treating point groups and translations,

$$\{R_\alpha|\tau\}\{R_\beta|\eta\} = \{R_\alpha R_\beta|\tau + \eta\}.$$

This last definition lets us study the two possible types of compound operations: glide planes ( $\{\sigma|\tau\}$ ) and screw axis ( $\{C_n|\tau\}$ ). In simpler words, the former is a reflection across a mirror plane (denoted by  $\sigma$ ) followed by a translation contained in the same plane and the latter is a rotation of  $\frac{2\pi}{n}$  around an axis followed by a translation along the same axis. As we can see, by admitting translations (this includes translations of a fraction of the unit cell vectors!) we expand the possible combinations that can describe real crystals. As such, there exist a substantially higher amount of space groups than point groups: 230 possible 3D space groups.

Within this huge amount of space groups, we can make a distinction between symmorphic and non-symmorphic space groups. We can write any space group operation in the following way:

$$\{R_\alpha|\tau\} = \{R_\alpha|R_n + \tau_\alpha\} = \{\epsilon|R_n\}\{R_\alpha|\tau_\alpha\},$$

where  $\epsilon$  is identity,  $R_n$  is a general vector of the Bravais lattice and  $\tau_\alpha$  is a non-primitive translation of the Bravais lattice. If, with a suitable choice of origin in the lattice, we find that all the elements of the space group are in the form  $\{\epsilon|R_n\}\{R_\alpha|0\}$  ( $\tau_\alpha = 0$  for all point-group symmetry operations), then the space group is called a simple or symmorphic group. All the others are called nonsymmorphic. There exist 73 symmorphic and 157 nonsymmorphic space groups.

### 1.5.3 Site symmetry groups and Wyckoff positions

As we have mentioned, we can have many different atomic sites within a unit cell. Since we know that point groups leave *at least one* point unchanged, the other lattice sites might not be left unchanged under some or by all of the symmetries contained in the point group. Therefore, we introduce the site-symmetry group as a subgroup of the point group whose elements leave that particular site invariant.

In addition, a point  $P$  is called a point of special position with respect to the space group  $G$  if there is at least one symmetry operation of  $G$ , in addition to the identity, that leaves  $P$  invariant (otherwise,  $P$  is called a point of general position).

Finally, a Wyckoff position consists of all points  $P$  for which their site-symmetry groups are conjugate subgroups of  $G$ . To illustrate this, let us assume Wyckoff position  $b$  has two points  $A$  and  $B$ , whose site-symmetry groups we denote as  $H_A$  and  $H_B$ . This means that there exists  $g \in G$  such that  $gH_Ag^{-1} = H_B$ . Because of this, we include points  $A$  and  $B$  in the same Wyckoff letter.

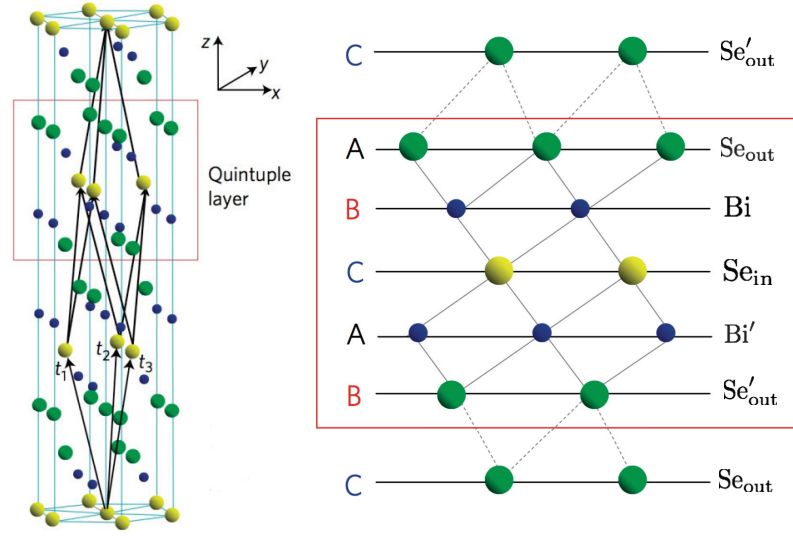


**Figure 1.2** Left: Figure showing the three quintuple layers that are contained in a unit cell, as well as the unit vectors. Right: Layers within a quintuple layer, showing the different types of atomic sites (that are contained in different unit cells). Adapted from Ref. [16].

#### 1.5.4 A useful example

To illustrate these 3 concepts, we take a look at the crystal structure of  $\text{Bi}_2\text{Se}_3$  and  $\text{Bi}_2\text{Te}_3$  that will be the crystals under study in chapter 3. The crystal structure of  $\text{Bi}_2\text{Se}_3$  consists of an ABC stacking of monoatomic triangular lattices normal to the  $c$ -axis. We can see this through the figures produced in Ref. [16], shown in Fig. 1.2. These layers are grouped into quintuple layers (QL) of strongly bounded planes, while neighboring QL interact mainly through van der Waals forces. Each QL contains two equivalent “outer” Se planes ( $\text{Se}_{\text{out}}$ ), two equivalent Bi planes, and another “inner” Se plane ( $\text{Se}_{\text{in}}$ ) located at the center of inversion. Below, we will denote as  $z$  the direction perpendicular to the QL, while  $x$  and  $y$  will indicate orthogonal axes in the plane of the QL.

These crystals structures can be studied from their symmetry groups, as we have said before. Both  $\text{Bi}_2\text{Se}_3$  and  $\text{Bi}_2\text{Te}_3$  belong to the  $D_{3d}$  ( $\bar{3}m$ ) point group. This point group belongs to the rhombohedral structure, and it is denoted by

$$\bar{3}m \equiv D_{3d} = \{E, 2C_3, 3C'_2, I\}, \quad (1.52)$$

where  $C_n$  denotes an axis of  $\frac{2\pi}{n}$  rotation. In the case of  $\text{Bi}_2\text{Se}_3$  the unprimed axis points along the  $z$  direction and the primed axis is contained in the  $xy$  plane. Finally,  $I$  denotes

inversion. Because it contains inversion, this crystal structure is centrosymmetric and thus a good candidate for the presence of hidden polarizations. In the Herman–Mauguin notation ( $\bar{3}m$ ), the  $\bar{3}$  denotes a rotoinversion (a  $\frac{2\pi}{3}$  rotation followed by inversion) and  $m$  denotes a mirror plane. Both operations that can be constructed from the ones listed in eq. 1.52. In particular, both  $\text{Bi}_2\text{Se}_3$  and  $\text{Bi}_2\text{Te}_3$  belong to space group 166:  $R\bar{3}m$ , which is symmorphic.

Due to the ABC stacking, the primitive rhombohedral unit cell spans three QL and contains five atoms: two  $\text{Se}_{\text{out}}$ , two Bi and one  $\text{Se}_{\text{in}}$ . An identical crystal structure applies to  $\text{Bi}_2\text{Te}_3$ , upon replacing Se by Te. The following are important points about the site-symmetry groups of the five different atomic sites in the unit cell that we will use later in chapter 3:

- The site-symmetry group of  $\text{Se}_{\text{in}}$  is  $D_{3d}$ . That is, it coincides with the point group of the crystal and thus it is a special point. The Wyckoff letter for this special position is  $a$ . Because it contains inversion, both local spin and orbital polarizations have to be zero (see eqs. (1.32)).
- The site-symmetry group of  $\text{Se}_{\text{out}}$  and Bi is  $3m \equiv C_{3v} = \{E, 2C_3, 3\sigma_v\}$ . It is a subgroup of  $D_{3d}$ . It contains elements other than  $E$ , so they sit at a special position, which is denoted by Wyckoff letter  $c$  in standard tables. Because  $\text{Se}_{\text{out}}$  and  $\text{Se}'_{\text{out}}$  are related by inversion, they belong to the same Wyckoff position. The same thing happens with Bi and  $\text{Bi}'$ . Because they *locally break* inversion symmetry (there is no  $I$  in their site-symmetry group), they are good candidates to host hidden electronic polarizations.

## Chapter 2

# Nuclear magnetic resonance in an electric field

So far, we have seen that centrosymmetric materials can host hidden electronic polarizations. How can we probe these effects? We have seen that for spin, for example, this electronic polarization is hidden in two ways, as we have seen from eqs. (1.32): they are compensated both in momentum and real space. It was proposed in chapter 1 that in principle, by changing the population of electronic states by means of an electric field, we could render this hidden polarizations locally visible in real space,

$$\mathbf{m}(\mathbf{r}) = -\mathbf{m}(-\mathbf{r}), \quad (2.1)$$

where we had defined  $\mathbf{m}$  as a local magnetic moment. However, this effect is still compensated within a unit cell due to the inversion symmetry. This tells us that any measurement that is global in nature, i.e. depends only on the global symmetries of the crystal, will not capture the local effects.

There have been some proposed methods to probe this effect, and all of them, to the best of our knowledge, use surface-dependent probes. First, the average over the unit cell can be made nonzero by breaking the bulk inversion symmetry at the surface. The resulting net spin polarization would be accessible to surface sensitive probes [3]. Second, in layered materials, a light beam penetrating the crystal along the stacking direction probes predominantly the topmost layer. This fact has enabled the “detection” of the hidden spin polarization in  $WSe_2$  [4]. Third, in certain materials such as  $MoS_2$ , spin-dependent dipole selection rules allow to probe the hidden spin polarization under irradiation by circularly polarized light [5].

However, as recently suggested in Ref. [6], the fundamental inversion-symmetry breaking at the surface spin-splits the original bulk bands for general  $k$ , as we have seen in section 1.4. This effect interferes in spin-resolved surface-sensitive experiments, such as spin- and angle-resolved photoemission spectroscopy (s-ARPES), where we see a spin-splitting of bands that does not reflect the bulk effects [17]. This argument makes a good case for finding a bulk probe to truly disentangle the spin-splitting effects present in basically any surface from the “hidden” ones.

In this chapter, we propose nuclear magnetic resonance as a local, bulk probe of the “hidden” electronic polarizations. The way it will work will be detailed in the following sections, but the idea is as follows: there is a local non-zero value of both electronic orbital and spin-angular momentum *at* the nuclear sites. This is also true for other places around them, as we can see from eqs. (1.32), and thus will also contribute to our effect. Therefore, through the hyperfine coupling between nuclear and electronic spins for example, the nucleus feels an effective magnetic interaction. This communication between electron and nuclear spins is the basis of our proposal. By applying a strong external magnetic field, the nuclear spins will precess at a frequency that depends on the gyromagnetic ratio of the nucleus and the magnitude of the magnetic field. However, the local information given by the electrons will modify this resonance frequency that is sensitive to our probes, thus revealing the “hidden” polarizations.

## 2.1 Nuclear magnetic resonance

---

Magnetic resonance is a phenomenon found in systems that possess magnetic moments. As we said, and as we will show, the term resonance comes from the fact that we will use external, tunable perturbations that can let us access a natural frequency of the system – the precession of a nuclear magnetic moment under a magnetic field, for example. The advantage of this is that we can access local perturbations to this natural frequency coming from the details of the system, and it can possess a reasonable resolution. In this section we look at the resonant condition and what are the local perturbations that we will be interested in for the rest of the chapter.

### 2.1.1 Resonance condition

The principle of magnetic resonance comes from the idea that angular momentum and magnetic moment are related to each other,

$$\boldsymbol{\mu} = \gamma \hbar \mathbf{I}, \quad (2.2)$$

where  $\boldsymbol{\mu}$  is a magnetic moment,  $\mathbf{I}$  is a dimensionless angular momentum operator, such as electronic or nuclear spin, and  $\gamma$  is what is called the gyromagnetic ratio. This last quantity can be better understood from a classical viewpoint, in which we have a charge that moves in a circular path. The ratio between its angular momentum and its magnetic moment associated with the current that it generates tells us, for example, that big masses have low gyromagnetic ratios.

If we now apply a constant and homogeneous magnetic field along the  $\hat{z}$  direction, we can look at the effective Zeeman interaction between  $\mathbf{H} = H_0 \hat{z}$  and our magnetic moment,

$$\mathcal{H} = -\boldsymbol{\mu} \cdot \mathbf{H} = -\hbar \gamma H_0 I_z. \quad (2.3)$$

The eigenvalues of this problem are quite simple since they will only be based on the eigenvalues of  $I_z$ , which are the  $2I + 1$  values that we know from elementary quantum mechanics,

$$E = -\hbar \gamma H_0 m \quad m = -I, \dots, I - 1, I.$$

The levels are equally spaced by  $\hbar \gamma H_0$ . We want to access the information about these energy levels, and the usual way to think about it is by using some sort of spectral absorption. This means that we want some time-dependent interaction that can induce transitions between the energy levels,

$$\Delta E = \hbar \omega.$$

Of course, we have to make sure that the interaction has non-vanishing matrix elements that join initial and final states. In other words, the transition has to be allowed. One way to do this is by using a transverse alternating magnetic field. In terms of a perturbation energy,

$$\mathcal{H}_{\text{pert}} = -\hbar \gamma H_x^0 I_x \cos(\omega t).$$

The allowed transitions for the operator  $I_x$  involve states with  $\Delta m = \pm 1$ . Consequently, the

difference in energy  $\Delta E$  coincides with adjacent energy levels, and thus,

$$\begin{aligned}\hbar\omega &= \gamma\hbar H_0 \\ \text{or } \omega &= \gamma H_0.\end{aligned}\tag{2.4}$$

The fact that  $\hbar$  goes away hints us that this process can be explained from a classical point of view, and in fact it does, with the classical picture of Larmor frequency.

In a resonance experiment, we will have a macroscopic sample that will absorb that energy. To make sure that we will be able to get a signal, we need to look at the nuclear spins from a statistical point of view. For details, we refer to Ref. [18]. For simplicity, we will imagine a crystal with nuclear spins  $I = \frac{1}{2}$ . Knowing that the sample will have a time-dependent perturbation, the energy absorption as a function of time will be given by computing the number of spins per second that go from the lower energy to the upper and subtracting the number that drop down, emitting energy,

$$\frac{dE}{dt} = N_+ W \hbar\omega - N_- W \hbar\omega = \hbar\omega W n,$$

where  $W$  is the probability per second of inducing either a  $m = \frac{1}{2} \rightarrow m = -\frac{1}{2}$  or viceversa.  $n$  is the difference in population between nuclei with  $m = \frac{1}{2}$  and  $m = -\frac{1}{2}$ . This difference in population will depend on the temperature of the sample, the external magnetic field and the transition rates provided by the capacity of the reservoir to absorb or lend energy to the nuclear spins. The ratio between  $N_+$  and  $N_-$  at thermal equilibrium will be given by the Boltzmann weight,

$$\frac{N_-^0}{N_+^0} = e^{-\gamma\hbar H_0/k_B T}.\tag{2.5}$$

In a steady state, the population difference between spin states  $n$  is governed by the thermal equilibrium value  $n_0 = N_+^0 - N_-^0$ , the square of the alternating magnetic field's magnitude  $\propto W$ , and the characteristic time associated with thermal equilibrium  $T_1$ ,

$$n = \frac{n_0}{1 + 2WT_1}.$$

This tells us that if  $2WT_1 \ll 1$ , the alternating magnetic field does not perturb much the population difference away from its thermal value. Finally, we could compute the absorption rate in this steady state. The conclusion that we can draw from this is that our perturbation will not change much the spin population difference that is essential to be able to perform a resonance experiment to get a signal *as long as* the thermal relaxation time is not long compared to the probability transition rate induced by the perturbation. In other words, if

we want to induce an absorption of energy that we can read from a detector, the perturbation has to be small enough to allow it.

In this subsection, we have so far ignored the fact that nuclei in real life are never isolated. For example, eq. (2.3) neglects the fact that the nuclei are surrounded by electrons. In a resonance experiment, there are many effects that can change the information relative to a “nucleus in vacuum” scenario. For example, in paramagnetic substances, electronic spin tries to align itself to the external magnetic field, making the nucleus feel a different effective local magnetic field. This can present itself in many ways that are different in nature, but they all come from the fundamental nucleus-electron interaction. The electrons also have an orbital degree of freedom, and the orbital currents can have a non-vanishing effect on the resonance frequencies. To settle the terminology, we will simply call all the effects that change the resonance frequency from a reference value (“vacuum” or diamagnetic samples) *NMR shifts*. There are many other interactions that change the shape of a linewidth, which can have important consequences on the detection of resonance lines, or we can also draw conclusions from them, such as nucleus-nucleus dipolar interaction. For now, we will focus on the NMR shifts that will give us the information about the hidden polarizations.

Let us modify our simple Hamiltonian, eq. (2.3), by introducing non-interacting electrons that otherwise interact with the nuclei,

$$\mathcal{H} = \mathcal{H}_n + \mathcal{H}_e + \mathcal{H}_{en}, \quad (2.6)$$

where  $\mathcal{H}_n$  includes our previous nuclear Zeeman term and can in principle include interactions between nuclei.  $\mathcal{H}_e$  is the Hamiltonian due to the non-interacting electrons under a Zeeman interaction with the magnetic field and under the crystal potential, eq. (1.1), and the interaction of the orbital degrees of freedom with the vector potential. Finally,  $\mathcal{H}_{en}$  is the magnetic interaction between the nuclei and the electrons. In this subsection we will focus on what are the most important interactions between electrons and nuclei in NMR experiments.

### 2.1.2 Spin-spin interactions

We will consider the interaction between the electronic spins and the nuclear spins. As long as the nuclear magnetic moment  $\boldsymbol{\mu}_n$  and the electronic one  $\boldsymbol{\mu}_e$  are far from each other, we could expect their interaction to be mediated in first order by a dipole-dipole interaction,

$$\mathcal{H}_{en}^{\text{dip}} = \frac{\mu_0}{4\pi} \left( \frac{\boldsymbol{\mu}_n \cdot \boldsymbol{\mu}_e}{r^3} - \frac{3(\boldsymbol{\mu}_n \cdot \mathbf{r})(\boldsymbol{\mu}_e \cdot \mathbf{r})}{r^5} \right), \quad (2.7)$$

where  $\mathbf{r}$  is the radius vector from the nucleus to the electron. As long as the electronic wave function is in a state of non-zero angular momentum, we can expect this approximation to be good. However, for  $s$ -states, this approximation breaks down, given that there is a nonzero probability of finding the electron at the nucleus, thus making the terms in eq. (2.7) diverge. Physically, we expect the  $s$ -orbital contribution to the dipolar interaction to average to zero. In this particular case, we have to maneuver to find a good expression for a finite electronic density at close distances to the nucleus.

#### Hyperfine coupling

To handle electronic  $s$ -states, one usually follows the path of the Dirac equation, since this effect will become more pronounced when the electron is closer to the nucleus than its “classical radius”. However, there is a simple way to derive this interaction from a classical standpoint, whose result is however valid in the relativistic scenario.

Let us model the nucleus as a charge  $q$  traveling in a circular loop of radius  $a$  with velocity  $v$ . The current associated with this motion is simply  $qv/(2\pi a)$ . We can express the magnetic field, due to the nucleus, in the  $\hat{z}$  direction  $\bar{H}_z$ , as an average over the electron ( $s$ -) orbital probability density  $|u(\mathbf{r})|^2$ ,

$$\bar{H}_z = \int d\tau H_z(r) |u(\mathbf{r})|^2, \quad (2.8)$$

where  $H_z(r)$  is the field of the current loop which is perpendicular to the  $\hat{z}$ -direction and  $d\tau$  is a volume differential. Since  $|u(\mathbf{r})|^2$  corresponds to a spherically-symmetric  $s$ -orbital, the other components of the magnetic field vanish. The contributions of  $H_z(r)$  for  $r > a$  will vanish simply due to the angular part of the integral. Finally, writing out the field  $H_z(r)$  as a sum of products of spherical harmonics with radial functions, only the term that corresponds to a uniform field ( $H_c$ ,  $c$  for center of the loop), within  $r < a$  will not vanish [18]. Then, the field due to the nucleus in the  $\hat{z}$ -direction looks like,

$$\bar{H}_z = \int_0^a dr H_c |u(\mathbf{r})|^2.$$

Approximating that  $|u(\mathbf{r})|^2$  does not change much inside the nucleus, then,

$$\bar{H}_z \approx H_c |u(\mathbf{0})|^2 \frac{4\pi}{3} a^3. \quad (2.9)$$

And we know how to calculate the field at a distance  $a$  from the center of the loop,

$$\mathbf{H}_c = \frac{\mu_0}{4\pi} \frac{qv \times \mathbf{r}}{r^3} = \frac{\mu_0}{4\pi} \frac{qv}{a^2} \hat{k}.$$

At the same time, we know that the magnetic moment  $\boldsymbol{\mu}_n$  of the nucleus is given by the current  $i$  circulating,  $\boldsymbol{\mu}_n = i\pi a^2 \mathbf{k}$ . We can thus relate the magnetic field in the  $\hat{z}$  to the magnetic moment of the nucleus,

$$\bar{H}_z \hat{k} = \frac{\mu_0 \boldsymbol{\mu}_n}{2\pi a^3} |u(0)|^2 \frac{4\pi}{3} a^3 = \frac{2}{3} \mu_0 \boldsymbol{\mu}_n |u(0)|^2.$$

Therefore, the ‘‘Zeeman’’ energy for the interaction between a electronic magnetic moment and this magnetic field is:

$$E = -\frac{2}{3} \mu_0 \boldsymbol{\mu}_n \cdot \boldsymbol{\mu}_e |u(0)|^2.$$

We want to express this in terms of an operator that translates that we only keep the electronic wavefunction at the nucleus. Once we do this, it looks like the usual ‘‘Darwin’’ term, or usually called Fermi contact term,

$$\mathcal{H}_{\text{cont}} = -\frac{2}{3} \mu_0 \boldsymbol{\mu}_n \cdot \boldsymbol{\mu}_e \delta(\mathbf{r}), \quad (2.10)$$

where  $\delta(\mathbf{r})$  is a Dirac delta function. We can re-write in a more familiar form by expanding the magnetic moment of an electron. We know that the gyromagnetic ratio of an electron is  $\gamma_e = g_s \frac{\mu_B}{\hbar}$ , where  $\mu_B$  is the Bohr magneton. Expressing the magnetic moment of the electron as  $\boldsymbol{\mu}_e = -\gamma_e \hbar \mathbf{S}$ , we get

$$\mathcal{H}_{\text{cont}} = \boldsymbol{\mu}_n \cdot \left( \frac{2}{3} \mu_0 g_s \mu_B \mathbf{S} \delta(\mathbf{r}) \right). \quad (2.11)$$

We can then define the contact contribution to the local magnetic field as

$$\mathbf{H}_{\text{cont}} = -\frac{2}{3} \mu_0 g_s \mu_B \langle \mathbf{S} \delta(\mathbf{r}) \rangle. \quad (2.12)$$

This contact interaction is the one responsible for many of the known phenomena in nuclear magnetic resonance in terms of Knight shifts. In fact, Slichter [18] refers to the Knight shift as being solely the shift due to this contact term. It successfully explains four experimental facts found for NMR in metals:

1. It predicts that a higher resonance frequency is needed for the metal than in the diamagnetic reference.
2. The fractional shift  $\Delta\omega/\omega$  is independent of  $\omega$  and thus of the external magnetic field.
3. The fractional shift is independent of temperature.
4. The shift is larger for larger-Z atoms (that have larger  $|u(0)|^2$ ).

We will not show these facts for simple cases but we will corroborate it in our results.

### Dipolar interaction

While the contact interaction is enough to understand the main experimental results and usually is the predominant interaction in simple metals, the dipole-dipole interaction between magnetic moments due to spins has to be computed if we want to achieve a more complete picture of the magnetic interaction that the nucleus feels. As we have mentioned before, for orbitals with nonzero orbital angular momentum, eq. (2.7) is a good approximation to the magnetic interaction. We can rewrite this interaction in terms of the magnetic dipole due to the electron spin,

$$\mathcal{H}_{en}^{\text{dip}} = -\boldsymbol{\mu}_n \cdot \frac{\mu_0}{4\pi} g_s \mu_B \left( \frac{\hat{\mathbf{S}} - 3\hat{\mathbf{r}}(\hat{\mathbf{S}} \cdot \hat{\mathbf{r}})}{r^3} \right) \quad (2.13)$$

and we can thus identify an effective magnetic field felt by the nucleus and that is due to the dipolar magnetic moment of the electron spin,

$$\mathbf{H}_{\text{dip}} = \frac{\mu_0}{4\pi} g_s \mu_B \int d^3r \frac{\langle \mathbf{S}(\mathbf{r}) \rangle - 3\hat{\mathbf{r}}(\langle \mathbf{S}(\mathbf{r}) \rangle \cdot \hat{\mathbf{r}})}{r^3}, \quad (2.14)$$

where  $\hat{\mathbf{r}}$  indicates the position unit vector.

### 2.1.3 Orbital currents

In the previous subsection, we have seen that because the electron spin interacts with an external magnetic field, for example, we would have a spin response that can itself interact with the nucleus. On the other hand, we know that electrons have an orbital degree of freedom that can also interact with the external magnetic field. This response of the orbital degree of freedom can in itself generate an effective magnetic field for the nucleus. The shift produced by this type of interaction is called the *chemical shift*. Here we will give a small derivation of the magnetic field that is felt by the nuclear magnetic moment due to the orbital currents, taken from Ref. [18].

Let us consider the single-electron Hamiltonian that we have been considering so far, but under a magnetic field. We can then introduce two vector potentials:  $A_0$  and  $A_n$ . The former is the vector potential associated with the external magnetic field  $\mathbf{H}_0$ , and the latter is the one due to the nucleus  $\mathbf{H}_n$ . In other words,

$$\mathbf{H}_0 = \nabla \times A_0 \quad \mathbf{H}_n = \nabla \times A_n.$$

The Hamiltonian has to transform with the minimal-coupling recipe, the Peierls substitution,

$$\mathcal{H} = \frac{1}{2m} (\mathbf{p} - q\mathbf{A})^2 + V. \quad (2.15)$$

It is clear that we are free to choose the gauge we want, and under a gauge transformation, the solutions to this previous equation have to change accordingly. We then define the current density under the presence of a vector potential to ensure gauge invariance,

$$\mathbf{j}(\mathbf{r}) = \frac{q}{2m} \frac{\hbar}{i} (\psi^* \nabla \psi - \psi \nabla \psi^*) - \frac{q^2}{m} \mathbf{A} \psi^* \psi, \quad (2.16)$$

where  $\psi$  is any wavefunction. Since under a gauge transformation both  $\psi$  and  $\mathbf{A}$  both change, it can be shown that this probability current is gauge invariant. Let us now expand our Hamiltonian, eq. (2.15),

$$\mathcal{H} = \frac{1}{2m} (\mathbf{p} - q\mathbf{A}_0 - q\mathbf{A}_n)^2 + V.$$

Recognizing then  $\boldsymbol{\pi} = \mathbf{p} - q\mathbf{A}_0$  as the canonical momentum that does not consider the nuclear field contribution, we can rewrite our Hamiltonian as

$$\mathcal{H} = \frac{1}{2m} \boldsymbol{\pi}^2 - \frac{q}{2m} (\boldsymbol{\pi} \cdot \mathbf{A}_n + \mathbf{A}_n \cdot \boldsymbol{\pi}) + \frac{q^2}{2m} \mathbf{A}_n^2 + V.$$

We will go ahead and consider the vector potential associated to the nucleus as the one that generates a dipolar field:

$$\mathbf{A}_n = \frac{\mu_0}{4\pi} \frac{\boldsymbol{\mu} \times \mathbf{r}}{r^3}, \quad (2.17)$$

where  $\boldsymbol{\mu}$  is the nuclear magnetic moment. We clarify that choosing a gauge in this context means setting an origin from which we measure this field. Since the nuclear magnetic moment is small compared to the electronic magnetic moments, we will drop the quadratic term in our previous Hamiltonian. Then,

$$\mathcal{H} \approx \frac{1}{2m} \boldsymbol{\pi}^2 + V - \frac{q}{2m} (\boldsymbol{\pi} \cdot \mathbf{A}_n + \mathbf{A}_n \cdot \boldsymbol{\pi}).$$

We note that the first two terms make the Hamiltonian of the electron under the magnetic field. Therefore, we will go ahead and treat the term that contains  $\mathbf{A}_n$  as a perturbation. This means that the first-order correction to the electronic energy due to the nucleus will be given by

$$E_{\text{pert}} = -\frac{q}{2m} \langle \psi | \boldsymbol{\pi} \cdot \mathbf{A}_n + \mathbf{A}_n \cdot \boldsymbol{\pi} | \psi \rangle = \frac{q}{2m} \int d^3r \psi^* (\boldsymbol{\pi} \cdot \mathbf{A}_n + \mathbf{A}_n \cdot \boldsymbol{\pi}) \psi,$$

where  $\psi$  is the solution of the single-particle Hamiltonian under a static magnetic field and the integral is over electron coordinates. Using that  $\boldsymbol{\pi}$  is Hermitian,

$$E_{\text{pert}} = -\frac{q}{2m} \int d^3r \mathbf{A}_n \cdot ((\boldsymbol{\pi}\psi)^* \psi + \psi^* (\boldsymbol{\pi}\psi)).$$

Now we can use the definition of  $\boldsymbol{\pi}$  to arrive at the following expression:

$$E_{\text{pert}} = - \int d^3r \mathbf{A}_n \cdot \mathbf{j}_0(\mathbf{r}),$$

where we have noted  $\mathbf{j}_0(\mathbf{r})$  as the current density when the external magnetic field is turned on, but does not consider the contribution of the nuclear vector potential. We can then substitute this last quantity, eq.(2.17),

$$\begin{aligned} E_{\text{pert}} &= - \frac{\mu_0}{4\pi} \int d^3r \frac{\boldsymbol{\mu} \times \mathbf{r}}{r^3} \cdot \mathbf{j}_0(\mathbf{r}) \\ &= -\boldsymbol{\mu} \cdot \frac{\mu_0}{4\pi} \int d^3r \frac{\mathbf{r} \times \mathbf{j}_0(\mathbf{r})}{r^3}. \end{aligned} \quad (2.18)$$

From the mean value of the current we can define an effective magnetic field due to this electronic current density as

$$\mathbf{H}_{\text{orb}} = \frac{\mu_0}{4\pi} \int d^3r \frac{\mathbf{r} \times \langle \mathbf{j}_0(\mathbf{r}) \rangle}{r^3}. \quad (2.19)$$

## 2.2 Staggered magnetic response

---

Thus far, we have described two types of shift – one due to the electron spin and the other due to the orbital currents produced by the electrons. Then we can say that a given nucleus feels a local magnetic field that is a sum of the external and the internal magnetic fields,

$$\omega(\mathbf{r}_0) = \gamma(\mathbf{r}_0) H_{\text{loc}}(\mathbf{r}_0), \quad (2.20)$$

where  $\gamma(\mathbf{r}_0)$  is the nuclear magnetogyric ratio and  $\mathbf{H}_{\text{loc}}(\mathbf{r}_0)$  is the local magnetic field acting on the nucleus. The local field can be separated into different contributions,

$$\mathbf{H}_{\text{loc}}(\mathbf{r}_0) = \mathbf{H}_{\text{ext}} + \mathbf{H}_{\text{cont}}(\mathbf{r}_0) + \mathbf{H}_{\text{dip}}(\mathbf{r}_0) + \mathbf{H}_{\text{orb}}(\mathbf{r}_0), \quad (2.21)$$

where  $\mathbf{H}_{\text{ext}}$  is the uniform and static external magnetic field and

$$\begin{aligned} \mathbf{H}_{\text{cont}}(\mathbf{r}_0) &= -\frac{2}{3} \mu_0 g_s \mu_B \langle \mathbf{S}(\mathbf{r}_0) \rangle \\ \mathbf{H}_{\text{dip}}(\mathbf{r}_0) &= \frac{\mu_0}{4\pi} g_s \mu_B \int d^3r \frac{\langle \mathbf{S}(\mathbf{r}) \rangle - 3\hat{\mathbf{r}}' \langle \mathbf{S}(\mathbf{r}) \rangle \cdot \hat{\mathbf{r}}'}{r'^3} \\ \mathbf{H}_{\text{orb}}(\mathbf{r}_0) &= \frac{\mu_0}{4\pi} \int d^3r \frac{\mathbf{r}' \times \langle \mathbf{J}(\mathbf{r}) \rangle}{r'^3}, \end{aligned} \quad (2.22)$$

where  $r' \equiv |\mathbf{r} - \mathbf{r}_0|$  and  $\hat{\mathbf{r}}' \equiv \mathbf{r}'/r'$ . Thus far, we have not yet explained how to evaluate the expectation value for the local spin and current operators. These quantities will be in general a response to the external fields. It means that whatever we will calculate in these responses will be a correction to the already present values for the local spin and current operators, that we express as

$$\begin{aligned}\mathbf{S}(\mathbf{r}) &= \sigma|\mathbf{r}\rangle\langle\mathbf{r}|/2 \\ \mathbf{J}(\mathbf{r}) &= -\frac{e}{2}\{\mathbf{v}, |\mathbf{r}\rangle\langle\mathbf{r}|\} - \frac{e^2}{m}\mathbf{A}(\mathbf{r})|\mathbf{r}\rangle\langle\mathbf{r}|,\end{aligned}\quad (2.23)$$

where  $\sigma$  is a vector of Pauli matrices,  $e$  and  $m$  are the electron's charge and mass,  $\{, \}$  is an anticommutator,  $\mathbf{v}$  is the velocity operator and  $\mathbf{A}$  is the vector potential.

In usual NMR, the external static field  $\mathbf{H}_{\text{ext}}$  is used to spin-polarize electrons and to produce orbital currents, both of which contribute to  $\mathbf{H}_{\text{loc}}(\mathbf{r}_0)$ . In linear response,

$$\mathbf{H}_{\text{loc}}(\mathbf{r}_0) = \mathbf{H}_{\text{ext}} + \chi_{\text{H}}(\mathbf{r}_0) \cdot \mathbf{H}_{\text{ext}}, \quad (2.24)$$

where the tensor  $\chi_{\text{H}}(\mathbf{r}_0)$  characterizes the electronic response to the external magnetic field. The internal field  $\chi_{\text{H}}(\mathbf{r}_0) \cdot \mathbf{H}_{\text{ext}}$  shifts the nuclear resonance frequency from its value in vacuum. In principle,  $\mathbf{H}_{\text{loc}}(\mathbf{r}_0)$  (and thus the resonance frequency) is identical for all nuclei of the same species located at symmetry-equivalent lattice sites. In practice, the resonance peak has a finite linewidth because local defects, inhomogeneities in the carrier density and interactions with neighboring nuclei lead to a distribution of the resonance frequencies for equivalent nuclei. From here on, we refer to this linewidth as the “intrinsic” linewidth.

In this work, we are interested in an *additional* contribution to  $\mathbf{H}_{\text{loc}}$  that arises in the presence of an *electric* field  $\mathbf{E}$ . As mentioned in Chapter 1, an electric field produces staggered spin and orbital-current densities in crystals hosting hidden spin and orbital polarizations. From Eq. (2.22), these spin and orbital polarizations result in a staggered magnetic field  $\mathbf{H}_{\text{stag}}$  that takes opposite directions for two nuclei of the same species located at inversion partner sites. Then, the total local field reads

$$\mathbf{H}_{\text{loc}}(\mathbf{r}_0) = \mathbf{H}_{\text{ext}} + \chi_{\text{H}}(\mathbf{r}_0) \cdot \mathbf{H}_{\text{ext}} + \mathbf{H}_{\text{stag}}(\mathbf{r}_0), \quad (2.25)$$

where  $\mathbf{H}_{\text{stag}}(\mathbf{r}_0) \neq 0$  only in presence of an electric field, and only if  $\mathbf{r}_0$  is not an inversion center. As we discuss below, the direction of  $\mathbf{H}_{\text{stag}}$  depends on the direction of  $\mathbf{E}$  as well as on the symmetry of the crystal. In this work, we will concentrate in the common situation where  $H_{\text{ext}} \gg |\chi_{\text{H}} \cdot \mathbf{H}_{\text{ext}}|$  and  $H_{\text{ext}} \gg H_{\text{stag}}$ . Nevertheless,  $H_{\text{stag}}$  need not be small compared to  $|\chi_{\text{H}} \cdot \mathbf{H}_{\text{ext}}|$ , mainly because  $H_{\text{stag}}$  is independent of  $H_{\text{ext}}$  in linear response.

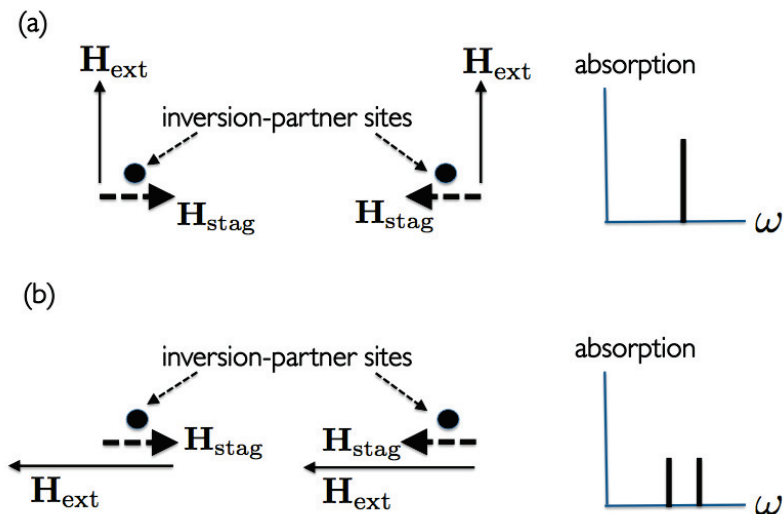


**Figure 2.1** The nuclear resonance frequency at inversion partner sites depends on the relative orientation between the staggered magnetic field and the external magnetic field. In (a),  $\mathbf{H}_{\text{ext}}$  is perpendicular to  $\mathbf{H}_{\text{stag}}$ , and the two sites have the same resonance frequency  $\propto [(H_{\text{ext}} + \chi_H H_{\text{ext}})^2 + H_{\text{stag}}^2]^{1/2}$ . In (b),  $\mathbf{H}_{\text{ext}}$  is aligned (or antialigned) with the staggered field and, consequently, the two sites have different resonance frequencies  $\propto (H_{\text{ext}} + \chi_H H_{\text{ext}} \pm |H_{\text{stag}}|)$ . Here,  $\chi_H \cdot \mathbf{H}_{\text{ext}}$  is the internal magnetic field produced by the electrons in response to  $\mathbf{H}_{\text{ext}}$ . For brevity, we have assumed that  $\chi_H \cdot \mathbf{H}_{\text{ext}}$  is parallel to  $\mathbf{H}_{\text{ext}}$ .

Under a uniform electric field,  $\mathbf{H}_{\text{stag}}$  does not vary from one unit cell to another (though, of course, it varies inside each unit cell in a staggered fashion). Consequently,  $\mathbf{H}_{\text{stag}}$  splits the resonance peak of a type of nucleus in two, without introducing additional broadening. For a given  $\mathbf{H}_{\text{stag}}$ , the magnitude of the splitting depends on the angle between  $\mathbf{H}_{\text{stag}}$  and  $\mathbf{H}_{\text{ext}}$ . As illustrated in Fig. 2.1, it is only the component of  $\mathbf{H}_{\text{stag}}$  parallel to  $\mathbf{H}_{\text{ext}}$  that contributes to the splitting. If  $\mathbf{H}_{\text{stag}} \perp \mathbf{H}_{\text{ext}}$ , all inversion partner nuclei have the same resonance frequency. If  $\mathbf{H}_{\text{stag}}$  is not perpendicular to  $\mathbf{H}_{\text{ext}}$ , the resonance frequencies of inversion partner nuclei differ from one another (by the component of  $\mathbf{H}_{\text{stag}}$  parallel to  $\mathbf{H}_{\text{ext}}$ ). The height of the two peaks is half the height of the parent peak. For sufficiently high electric fields, the splitting between the two peaks can become comparable to or larger than the intrinsic linewidth of each peak. It is in this regime that NMR can work as a probe of the hidden spin and (or) orbital polarizations.

### 2.2.1 Linear response

In order to make the preceding statements quantitative, a recipe is needed to compute  $\mathbf{H}_{\text{stag}}$ . Here, we consider a uniform and static electric field, and adopt the linear response expressions that have been introduced in earlier work [19, 8],

$$\delta\langle\mathbf{O}(\mathbf{r})\rangle = \delta\langle\mathbf{O}(\mathbf{r})\rangle_{\text{intra}} + \delta\langle\mathbf{O}(\mathbf{r})\rangle_{\text{inter1}} + \delta\langle\mathbf{O}(\mathbf{r})\rangle_{\text{inter2}} \quad (2.26)$$

for  $\mathbf{O}(\mathbf{r}) = \mathbf{S}(\mathbf{r}), \mathbf{J}(\mathbf{r})$ , where

$$\begin{aligned} \delta\langle\mathbf{O}(\mathbf{r})\rangle_{\text{intra}} &= -\frac{e\hbar}{2\Gamma} \sum_{E_{\mathbf{k}n}=E_{\mathbf{k}n'}} \langle\psi_{\mathbf{k}n}|\mathbf{O}(\mathbf{r})|\psi_{\mathbf{k}n'}\rangle \langle\psi_{\mathbf{k}n'}|\mathbf{v}\cdot\mathbf{E}|\psi_{\mathbf{k}n}\rangle \frac{\partial f_{\mathbf{k}n}}{\partial E_{\mathbf{k}n}} \\ \delta\langle\mathbf{O}(\mathbf{r})\rangle_{\text{inter1}} &= -2e\hbar \sum_{E_{\mathbf{k}n}\neq E_{\mathbf{k}n'}} \text{Re} [\langle\psi_{\mathbf{k}n}|\mathbf{O}(\mathbf{r})|\psi_{\mathbf{k}n'}\rangle \langle\psi_{\mathbf{k}n'}|\mathbf{v}\cdot\mathbf{E}|\psi_{\mathbf{k}n}\rangle] \frac{\Gamma(E_{\mathbf{k}n} - E_{\mathbf{k}n'})}{[(E_{\mathbf{k}n} - E_{\mathbf{k}n'})^2 + \Gamma^2]^2} (f_{\mathbf{k}n} - f_{\mathbf{k}n'}) \\ \delta\langle\mathbf{O}(\mathbf{r})\rangle_{\text{inter2}} &= -e\hbar \sum_{E_{\mathbf{k}n}\neq E_{\mathbf{k}n'}} \text{Im} [\langle\psi_{\mathbf{k}n}|\mathbf{O}(\mathbf{r})|\psi_{\mathbf{k}n'}\rangle \langle\psi_{\mathbf{k}n'}|\mathbf{v}\cdot\mathbf{E}|\psi_{\mathbf{k}n}\rangle] \frac{\Gamma^2 - (E_{\mathbf{k}n} - E_{\mathbf{k}n'})^2}{[(E_{\mathbf{k}n} - E_{\mathbf{k}n'})^2 + \Gamma^2]^2} (f_{\mathbf{k}n} - f_{\mathbf{k}n'}) \end{aligned} \quad (2.27)$$

are the intraband and interband contributions and  $\Gamma$  is a phenomenological electronic scattering rate (in units of energy). Notation-wise,  $\delta\langle\mathbf{O}(\mathbf{r})\rangle$  denotes the change in the expectation value of  $\mathbf{O}(\mathbf{r})$  due to the electric field. Evaluating Eqs. (2.26), (2.27) and inserting the outcome in Eq. (2.22), we obtain the  $\mathbf{E}$ -induced part of the local field, namely  $\mathbf{H}_{\text{stag}}(\mathbf{r}_0)$ . The contact and dipolar parts of  $\mathbf{H}_{\text{stag}}$  vanish in the absence of spin-orbit interactions, whereas the orbital part does not. It must be noted that  $\mathbf{H}_{\text{orb}}$  contains a staggered as well as a non-staggered part. The latter corresponds to the Oersted field created by a uniform electric current. This part will be left out of  $\mathbf{H}_{\text{stag}}$  and will be treated separately below.

The sums in Eq. (2.27) are carried out over the first Brillouin zone and over all energy bands (with the indicated constraints for intraband and interband parts). The evaluation of these sums requires the knowledge of the electronic structure of the material, the chemical potential, and the electronic scattering rate. Concerning the electronic structure, it should in principle be computed in the presence of  $\mathbf{H}_{\text{ext}}$ . We will however content ourselves with the energy bands and Bloch wave functions at zero external field, which is justified by the fact that we are interested in the linear response to electromagnetic fields. In regards to the chemical potential, it may be extracted from experimental measurements of the carrier density. The scattering rate  $\Gamma$  may be obtained by calculating the conductivity of the system with the Kubo formula and varying  $\Gamma$  in order to match it to the experimental value.

The expressions in Eq. (2.27) are valid when  $\Gamma$  is small: in conducting samples,  $\Gamma$  must be smaller than the Fermi energy (measured from the band edge); in insulating samples,

$\Gamma$  must be smaller than the energy gap. If these conditions are not met, one may resort to more general expressions based on Green's functions[20]. We have verified that the small scattering rate approximation is valid in the parameter regime considered below.

In the small  $\Gamma$  regime,  $\delta\langle\mathbf{O}(\mathbf{r})\rangle_{\text{intra}} \propto 1/\Gamma$ ,  $\delta\langle\mathbf{O}(\mathbf{r})\rangle_{\text{inter1}} \propto \Gamma$  and  $\delta\langle\mathbf{O}(\mathbf{r})\rangle_{\text{inter2}}$  is independent of the scattering rate. Consequently, in highly conducting crystals,  $\delta\langle\mathbf{O}(\mathbf{r})\rangle_{\text{intra}}$  is often dominant. On the contrary, in poorly conducting crystals, the interband part takes over. Moreover, in crystals with time-reversal symmetry,  $\delta\langle\mathbf{O}(\mathbf{r})\rangle_{\text{inter2}} = 0$  (much like the Hall conductivity vanishes in time-reversal symmetric crystals).

Formally, the relation between the applied electric field and the staggered magnetic field can be written as

$$\mathbf{H}_{\text{stag}}(\mathbf{r}_0) = \chi_E(\mathbf{r}_0) \cdot \mathbf{E}, \quad (2.28)$$

where  $\chi_E(\mathbf{r}_0)$  is a *magnetolectric* susceptibility tensor at the nuclear site  $\mathbf{r}_0$ . The form of this tensor, and hence the relative direction between the electric field and the staggered magnetic field, depend on the space group symmetry of the material. It is likewise important to recognize that  $\chi_E$  scales with the conductivity  $\sigma$  of the crystal. This is evident from Eq. (2.27), where replacing  $\mathbf{O}(\mathbf{r})$  by the velocity operator amounts to calculating the electric current produced by a uniform electric field (modulo a prefactor). For instance, in good conductors dominated by the contact interaction, a dimensional analysis shows that

$$\chi_E(\mathbf{r}) \sim \frac{\mu_0 \mu_B \sigma}{e v_F} \overline{|S_{\mathbf{k}n}(\mathbf{r})|}, \quad (2.29)$$

where  $\overline{|S_{\mathbf{k}n}(\mathbf{r})|}$  denotes the average of the magnitude of the (dimensionless) hidden spin polarization over the Fermi surface, and  $v_F$  is the (averaged) Fermi velocity. In a bad conductor, where the interband transitions are dominant, a relation similar to Eq. (2.29) still applies, but the Fermi surface matrix elements of the spin and velocity operators are replaced by interband matrix elements (e.g. between the top of the valence band and the bottom of the conduction band). In perfect insulators with time reversal symmetry, an electric field does not induce a staggered magnetization.

For the purpose of comparison, let us recall that an external electric field induces an electric polarization in perfect insulators with time reversal symmetry. Moreover, the polarizability of dielectrics remains finite in the  $\Gamma \rightarrow 0$  limit. The key behind the difference between the electric and magnetic cases lies in the fact that electrical polarization is even under time reversal, whereas the staggered magnetic field is odd. In fact, the direct counterpart of the dielectric polarization in our problem at hand resides in  $\delta\langle\mathbf{O}(\mathbf{r})\rangle_{\text{inter2}}$ , which would give a  $\Gamma$ -independent staggered magnetic field in an insulator with broken time-reversal symmetry.

In sum, highly conducting samples with large hidden polarizations are good candidates for achieving a strong electric-field-induced splitting of NMR peaks. However, although having a large hidden spin or orbital polarization is always favorable, highly conducting samples result in an unwanted NMR linewidth that can mask the peak splitting. Next, we discuss this problem and possible solutions to it.

### 2.3 Current-related complications

---

In conducting crystals, an electric field produces a linewidth of the resonance peaks which, if sufficiently pronounced, can mask the peaks splitting caused by the staggered field. There are two sources to this linewidth: (i) the change in the imaginary part of the spin and orbital susceptibility due to an electric field, and (ii) the Oersted (“amperian”) magnetic field  $\mathbf{H}_{\text{amp}}$  created by the electric current.

Source (i) implies a change in the  $T_1$  relaxation time in the presence of an electric field. Concentrating on the Fermi contact interaction (though the conclusion below will apply to dipolar and orbital contributions as well), the relaxation rate [21] at temperature  $T$  reads

$$1/T_1(\mathbf{r}_0) \propto T \sum_{\mathbf{q}} \chi''_{\perp,H}(\mathbf{q}, \omega_0, \mathbf{r}_0), \quad (2.30)$$

where  $\chi''_{\perp,H}(\mathbf{q}, \omega_0, \mathbf{r}_0)$  is the imaginary part of the local (at  $\mathbf{r}_0$ ) transverse magnetic susceptibility at momentum  $\mathbf{q}$  and at the resonance frequency  $\omega_0$ . To leading order in  $\omega_0$  (which is a small parameter in relation to characteristic electronic energy scales and disorder broadening) we find [22] that the change of  $\chi''_{\perp,H}$  produced by an electric field is odd under  $\mathbf{q} \rightarrow -\mathbf{q}$ . Hence, given the sum over  $\mathbf{q}$  in Eq. (2.30), there is no change in  $T_1$  to leading order in  $\mathbf{E}$  and  $\omega_0$ .

The linewidth produced by the amperian magnetic field  $\mathbf{H}_{\text{amp}}$  is more insidious, not least because it does not disappear at low temperature. Inside a cylindrical wire with a uniform current density  $J$ ,

$$\mathbf{H}_{\text{amp}}(r) = \frac{\mu_0 J r}{2} \hat{\phi}, \quad (2.31)$$

where  $r$  is the distance from the wire axis and  $\hat{\phi}$  is the azimuthal unit vector. The amperian field circulates in real space, with an average of zero for any nuclear species in the bulk. Therefore, the amperian field produces a distribution of resonance frequencies with zero mean, i.e. a linewidth, with no net shift in the resonance frequency (this is the opposite state of affairs compared to  $\mathbf{H}_{\text{stag}}$ , which shifts the resonance frequency without broadening it).

For latter reference, let us estimate the amperian linewidth. For simplicity, we suppose that the external magnetic field is large compared to the maximum amperian field inside the sample. Then, to first order in  $J$ , we can limit ourselves to the component of  $\mathbf{H}_{\text{amp}}$  that is parallel (or antiparallel) to  $\mathbf{H}_{\text{ext}}$ . Indeed, the component of  $\mathbf{H}_{\text{amp}}$  perpendicular to  $\mathbf{H}_{\text{ext}}$  contributes to the linewidth only to second order, i.e. it can be neglected in linear response theory. Assuming that  $\mathbf{H}_{\text{amp}}$  is coplanar to  $\mathbf{H}_{\text{ext}}$ , a straightforward calculation shows that the fraction of nuclei “seeing” a field between  $H_{\text{ext}} + H$  and  $H_{\text{ext}} + H + dH$  is given by

$$\rho(H)dH = \frac{2}{\pi} \frac{dH}{H_{\text{amp}}(R)} \sqrt{1 - \left(\frac{H}{H_{\text{amp}}(R)}\right)^2} \Theta(|H_{\text{amp}}(R)| - |H|), \quad (2.32)$$

where  $H$  is an arbitrary field along the direction of the external field,  $dH$  is a small interval,  $H_{\text{amp}}(R) = \mu_0 J R / 2$  is the magnitude of the amperian field at the surface of the wire, and  $\Theta(x)$  is the Heaviside function. We verify that  $\int_{-\infty}^{\infty} \rho(H)dH = 1$ . Equation (2.32) gives the current-induced distribution of the resonance frequencies for any nuclear species. It shows that the resonance peak loses its height and is broadened as the current density increases, the linewidth being given by  $\simeq 2H_{\text{amp}}(R)$ .

The NMR peak splitting produced by  $\mathbf{H}_{\text{stag}}$  can be experimentally resolved if it is comparable or larger than the combined intrinsic and Amperian linewidths. The staggered field and the intrinsic linewidth are independent of the wire radius (unless the wire is so narrow that quantum confinement effects become significant, a circumstance that we do not consider here), while the amperian linewidth grows linearly with the wire radius. This implies that the staggered field will be masked by the amperian linewidth when the wire radius exceeds a certain value. We will return to this point below.

In order to eliminate the undesirable amperian linewidth, one might be tempted to work with samples that are as insulating as possible. However, this is not a good strategy because  $\chi_E$  scales roughly as the conductivity of the sample (cf. Eq. (2.29)): in perfectly insulating samples with time-reversal symmetry, the staggered field vanishes. A better strategy is to apply the external magnetic field parallel to the current: in this case,  $\mathbf{H}_{\text{amp}}$  is perpendicular to  $\mathbf{H}_{\text{ext}}$  and, as mentioned above, the amperian contribution to the linewidth becomes negligible to first order in the current density. However, this strategy will work only if  $\mathbf{H}_{\text{stag}}$  has a nonzero component parallel to the current. Whether or not this is the case depends on the material.

In the light of the preceding discussion, there are various questions that must be answered in order to assess the utility of NMR as a probe of the hidden spin and orbital polarization. Is it experimentally possible to attain an electric field at which the splitting of

the resonance peak becomes comparable to or larger than its intrinsic linewidth? Is the necessary electric field sufficiently high that the Joule heating will be problematic, and can the contribution of the current-induced staggered field be distinguished from the background of the amperian field? The answers to these questions are nucleus- and material-dependent.

In the next chapter, we proceed with a detailed study of two candidate materials, where hidden spin and orbital polarizations exist and where NMR spectra have been measured in the absence of electric currents. We will also discuss other materials which, according to symmetry arguments, could prove more promising.

## Chapter 3

# Material application: $\text{Bi}_2\text{Se}_3$ and $\text{Bi}_2\text{Te}_3$

In the last section of Chapter 1, we saw the crystal structure of  $\text{Bi}_2\text{Se}_3$  and  $\text{Bi}_2\text{Te}_3$  and we showed that these materials allow for the existence of hidden spin and orbital polarizations, as have been confirmed by other groups [3]. Since these materials are strongly spin-orbit coupled, they constitute interesting (though likely not ideal[3]) candidates to attain sizeable values of electric-field-induced staggered spin densities. Moreover, these compounds can develop antiferromagnetic order upon magnetic doping[23], which opens the prospect of steering the Néel order parameter via current-induced staggered spin and orbital densities. Adding to the interest, the past five years have witnessed numerous NMR experiments in  $\text{Bi}_2\text{Se}_3$  and  $\text{Bi}_2\text{Te}_3$  [24]-[25], which have led to a characterization of the shifts and linewidths for  $^{77}\text{Se}$ ,  $^{125}\text{Te}$  and  $^{209}\text{Bi}$  in the absence of external electric fields. These experiments have been largely spurred by the fact that  $\text{Bi}_2\text{Se}_3$  and  $\text{Bi}_2\text{Te}_3$  are topological insulators[16], although band topology will not play a significant role in our results. In this Chapter, we will develop a tight-binding model for their lattice structure to project the Bloch-states onto this basis. With this, we calculate the linear response formulae that we presented in Chapter 2. Finally, we can find the contribution to the local magnetic field of the electronic response to the electric field.

### 3.1 Tight-binding approximation

---

In this work, we adopt from Ref. [26] a  $sp^3$  tight-binding description of the single-electron Hamiltonian with spin-orbit interactions,

$$\mathcal{H} = \frac{\mathbf{p}^2}{2m} + V(\mathbf{r}) + \frac{\hbar}{4m^2c^2}(\nabla V \times \mathbf{p}) \cdot \boldsymbol{\sigma}, \quad (3.1)$$

where  $V(\mathbf{r}) = V(\mathbf{r} + \mathbf{R})$  is the lattice potential,  $\mathbf{R}$  are the Bravais vectors giving the positions of the unit cells,  $m$  is the bare electron mass,  $\mathbf{p} = -i\hbar\nabla$  is the canonical momentum,  $c$  is the speed of light in vacuum and  $\boldsymbol{\sigma}$  is a vector of Pauli matrices denoting the spin degree of freedom. The electronic velocity operator, which plays a central role in the theory of NMR shifts, is given by  $\mathbf{v} = (i/\hbar)[\mathcal{H}, \mathbf{r}] = \mathbf{p}/m + (\hbar/4mc^2)\boldsymbol{\sigma} \times \nabla V$ .

In the tight-binding description of the electronic structure, each lattice site is ascribed a localized electronic state  $|\mathbf{R}j\mu\sigma\rangle = |\mathbf{R}j\mu\rangle|\sigma\rangle$ ,  $j$  labels the five atoms inside the primitive unit cell,  $\mu = \{s, p_x, p_y, p_z\}$  denotes the atomic orbitals considered in the  $sp^3$  model, and  $\sigma$  is the spin index. The states  $|\mathbf{R}j\mu\sigma\rangle$  are Löwdin orbitals, obeying  $\langle \mathbf{R}j\mu\sigma | \mathbf{R}'j'\mu'\sigma' \rangle = \delta_{\mathbf{R}\mathbf{R}'}\delta_{jj'}\delta_{\mu\mu'}\delta_{\sigma\sigma'}$ .

Although the calculated orbitals centered in different atoms are not completely orthogonal, the overlaps  $\int d^3r \langle \mathbf{r} | \mathbf{R}j\mu \rangle \langle \mathbf{R}'j'\mu' | \mathbf{r} \rangle$  for  $j \neq j'$  are small enough that neglecting them does not result in a significant error.

In the basis of Löwdin orbitals, the Hamiltonian from Eq. (3.1) can be recasted in the second quantized form as

$$\mathcal{H} = \sum_{\mathbf{R}j\mu\sigma} \sum_{\mathbf{R}'j'\mu'\sigma'} \mathcal{H}_{j\mu\sigma;j'\mu'\sigma'}(\mathbf{R}, \mathbf{R}') c_{\mathbf{R}j\mu\sigma}^\dagger c_{\mathbf{R}'j'\mu'\sigma'}, \quad (3.2)$$

where  $c_{\mathbf{R}j\mu\sigma}^\dagger$  is an operator that creates an electron in state  $|\mathbf{R}j\mu\sigma\rangle$ , and  $\mathcal{H}_{j\mu\sigma;j'\mu'\sigma'}(\mathbf{R}, \mathbf{R}') = \langle \mathbf{R}j\mu\sigma | \mathcal{H} | \mathbf{R}'j'\mu'\sigma' \rangle$ . In  $\text{Bi}_2\text{Se}_3$  and  $\text{Bi}_2\text{Te}_3$ , the numerical values of  $\langle \mathbf{R}j\mu\sigma | \mathcal{H} | \mathbf{R}'j'\mu'\sigma' \rangle$  have been tabulated for up to third nearest neighboring sites by fitting to results from DFT.[26] Spin-orbit interactions, crucial in these materials, are incorporated through onsite terms. Fourier transforming Eq. (3.2), we have

$$\mathcal{H} = \sum_{\mathbf{k}} \sum_{j\mu\sigma} \sum_{j'\mu'\sigma'} \mathcal{H}_{j\mu\sigma;j'\mu'\sigma'}(\mathbf{k}) c_{\mathbf{k}j\mu\sigma}^\dagger c_{\mathbf{k}j'\mu'\sigma'}, \quad (3.3)$$

where  $\mathbf{k}$  is the crystal momentum (within the first Brillouin zone),  $c_{\mathbf{k}j\mu\sigma}^\dagger$  is an operator that

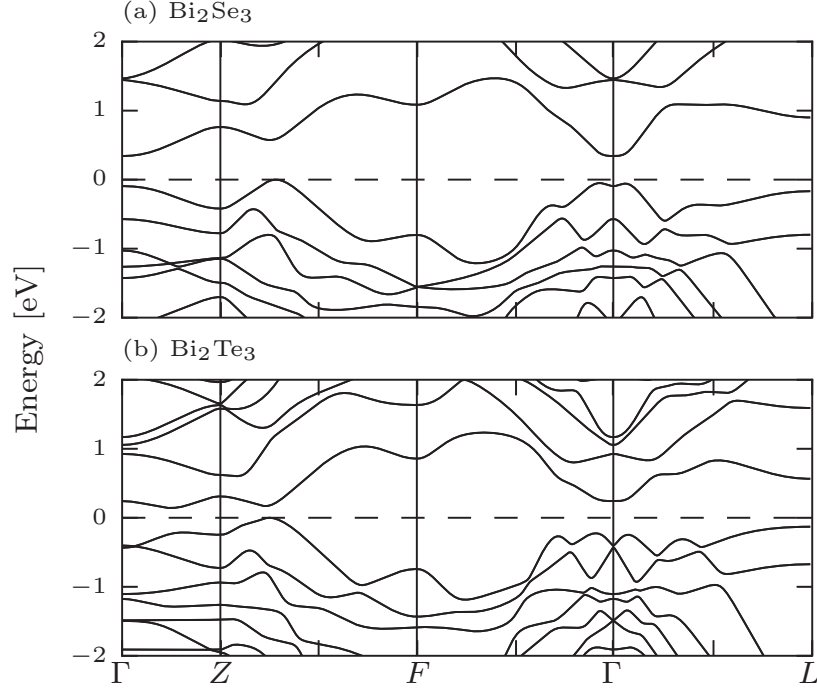


Figure 3.1 Bulk tight-binding bands for  $\text{Bi}_2\text{Se}_3$  and  $\text{Bi}_2\text{Te}_3$ .

creates an electron in a Bloch spinor

$$|\psi_{\mathbf{k}j\mu\sigma}\rangle = \frac{1}{\sqrt{N}} \sum_{\mathbf{R}} e^{i\mathbf{k}\cdot(\mathbf{R}+\mathbf{t}_j)} |\mathbf{R}j\mu\sigma\rangle, \quad (3.4)$$

$\mathbf{t}_j$  is the position of a given atom in the unit cell (so that  $\mathbf{R} + \mathbf{t}_j$  is its actual position in the lattice), and  $N$  is the number of unit cells in the crystal. The eigenstates and eigenvalues of  $\mathcal{H}$  are  $|\psi_{\mathbf{k}n}\rangle$  and  $E_{\mathbf{k}n}$ , respectively, where  $n$  denotes the band index. In particular,  $|\psi_{\mathbf{k}n}\rangle$  are Bloch spinors that obey  $\langle \mathbf{r} + \mathbf{R} | \psi_{\mathbf{k}n} \rangle = \exp(i\mathbf{k} \cdot \mathbf{R}) \langle \mathbf{r} | \psi_{\mathbf{k}n} \rangle$  and  $\langle \psi_{\mathbf{k}n} | \psi_{\mathbf{k}'n'} \rangle = \delta_{\mathbf{k}\mathbf{k}'} \delta_{nn'}$ . The set of states  $\{|\psi_{\mathbf{k}j\mu\sigma}\rangle\}$  defined in Eq (4) form an orthonormal basis. As such, we may write

$$|\psi_{\mathbf{k}n}\rangle = \sum_{j\mu\sigma} C_{\mathbf{k}n;\mathbf{k}j\mu\sigma} |\psi_{\mathbf{k}j\mu\sigma}\rangle, \quad (3.5)$$

where  $C_{\mathbf{k}n;\mathbf{k}j\mu\sigma} = \langle \psi_{\mathbf{k}j\mu\sigma} | \psi_{\mathbf{k}n} \rangle$ . The matrix elements of the Hamiltonian  $\mathcal{H}(\mathbf{k})$  are

$$\begin{aligned} \mathcal{H}_{j\mu\sigma;j'\mu'\sigma'}(\mathbf{k}) &= \langle \psi_{\mathbf{k}j\mu\sigma} | \mathcal{H} | \psi_{\mathbf{k}j'\mu'\sigma'} \rangle \\ &= \frac{1}{N} \sum_{\mathbf{R}\mathbf{R}'} e^{i\mathbf{k}\cdot(\mathbf{R}+\mathbf{t}_j-\mathbf{R}'-\mathbf{t}_{j'})} \mathcal{H}_{j\mu\sigma;j'\mu'\sigma'}(\mathbf{R}, \mathbf{R}'). \end{aligned} \quad (3.6)$$

To avoid confusion, we remark that  $\mathcal{H}(\mathbf{k}) \neq e^{-i\mathbf{k}\cdot\mathbf{r}} \mathcal{H} e^{i\mathbf{k}\cdot\mathbf{r}}$ . A numerical diagonalization of

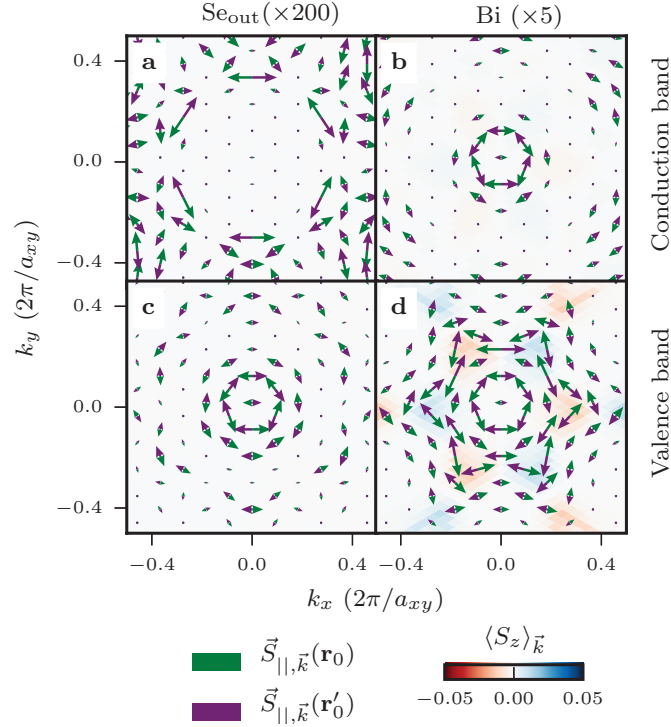


**Figure 3.2** Momentum-space spin textures for  $\text{Se}_{\text{out}}$  (panels (a) and (c)) and Bi (panels (b) and (d)) in  $\text{Bi}_2\text{Se}_3$ . Panels (a)-(b) show the textures at the bottom of the conduction band and panels (c)-(d) display the textures at the top of the valence band. Momentum in the  $k_z = 0$  plane is measured in units of the unit cell lattice parameter ( $a_{xy}$ , in the  $xy$  plane). All panels show the spin textures for inversion partners, in different colors. Angular momenta are measured in units of  $\hbar$ .

$\mathcal{H}(\mathbf{k})$  yields the eigenvalues  $E_{\mathbf{k}n}$  and the coefficients  $C_{\mathbf{k}n;\mathbf{k}j\mu\sigma}$  ( $n = 1, \dots, 40$ ). Figure 3.1 displays  $E_{\mathbf{k}n}$  along the high symmetry directions in the first Brillouin zone[26]. As we know by now, each energy level is doubly degenerate due to the combined time-reversal symmetry and spatial inversion symmetry, so we can only visualize 20 of the bands.

### 3.2 Linear response of the hidden polarizations

Now that we have the tight-binding model to our service, we can use this basis to start calculating some interesting quantities. In this section, we first present the local spin and orbital textures that the site symmetries of Bi and  $\text{Se}_{\text{out}}$  allow for. We exploit these textures to get a staggered magnetization within a unit cell at inversion-partnered sites, that we can calculate with the linear response equations. From there, we analyze the consequences of applying a current to our conducting samples, regarding the Amperian linewidth that we

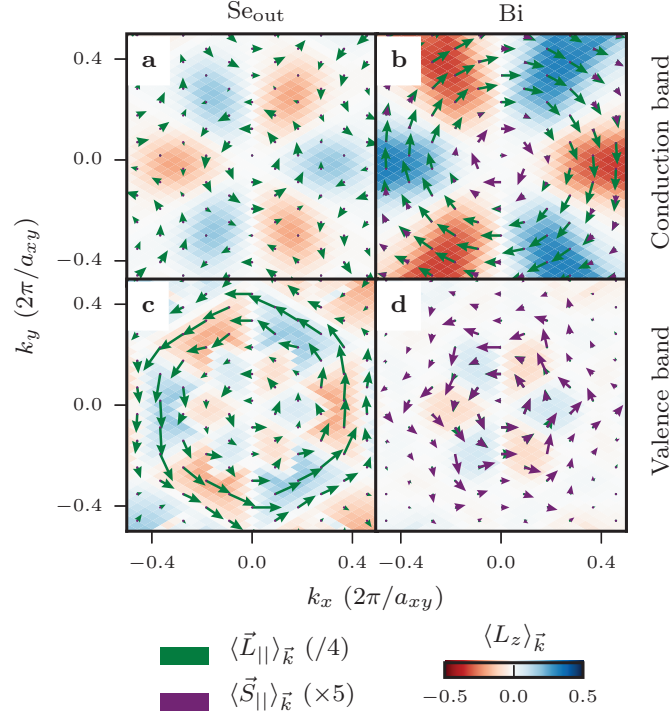


**Figure 3.3** Momentum-space spin and orbital textures for  $\text{Se}_{\text{out}}$  (panels (a) and (c)) and Bi (panels (b) and (d)) in  $\text{Bi}_2\text{Se}_3$ . Panels (a)-(b) show the textures at the bottom of the conduction band and panels (c)-(d) display the textures at the top of the valence band. Momentum in the  $k_z = 0$  plane is measured in units of the unit cell lattice parameter ( $a_{xy}$ , in the  $xy$  plane). Angular momenta are measured in units of  $\hbar$ .

have encountered in Chapter 2 and the Joule heating that a current produces. Finally, using the group theory concepts visited in Chapter 1, we propose other materials with which we can find a better experimental geometry for the detection of this effect.

### 3.2.1 Magnetic textures

Figure 3.2 illustrates the momentum-space spin textures for  $\text{Bi}_2\text{Se}_3$ , projected onto a Bi ( $\text{Bi}'$ ) and a  $\text{Se}_{\text{out}}$  ( $\text{Se}_{\text{out}'}$ ) site, in the absence of electric fields. These textures are calculated according to the definition of local spin from Eq. (1.31). We show only the s-orbital contribution to the spin textures, relevant to the contact interaction. We confirm the contents of Eqs. (1.32), which tell us that (a) for a fixed site, the expectation value of spin for a given band is opposite for opposite values of  $\mathbf{k}$  and (b) for a fixed  $\mathbf{k}$ , the expectation value of spin for a given band is opposite for inversion partners. We can also see how the magnitude of spin polarization is larger for Bi than for  $\text{Se}_{\text{out}}$ , which is consistent with the large s-orbital component of the

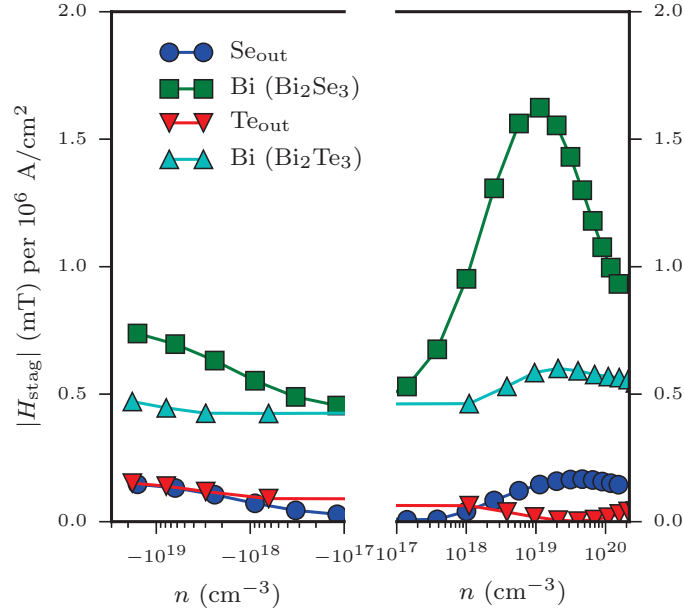


**Figure 3.4** Electric-field-induced staggered magnetic field as a function of the carrier density for different nuclei in  $\text{Bi}_2\text{Se}_3$  and  $\text{Bi}_2\text{Te}_3$ , at room temperature, for a fixed electronic scattering rate  $\Gamma = 10 \text{ meV}$  and a fixed current density  $J = 10^6 \text{ A/cm}^2$ .

conduction and valence bands for the bismuth site [8].

Figure 3.3 illustrates the momentum-space spin and orbital textures for  $\text{Bi}_2\text{Se}_3$ , projected onto a Bi and a  $\text{Se}_{\text{out}}$  site, in the absence of electric fields. These textures are calculated according to the definition of local spin from Eq. (1.31) and from Ref. [2]. We again show only the s-orbital contribution to the spin textures, relevant to the contact interaction. Both orbital and spin textures are considerable, but the former can be up to an order of magnitude larger (reaching up to  $0.5\hbar$ ).

### 3.2.2 Staggered magnetization

In the presence of an electric field, we combine Eqs. (2.22) and (2.27) in order to obtain the staggered field acting on the nuclei. The form of the magnetoelectric tensor  $\chi_E$  (cf. Eq. (2.28))

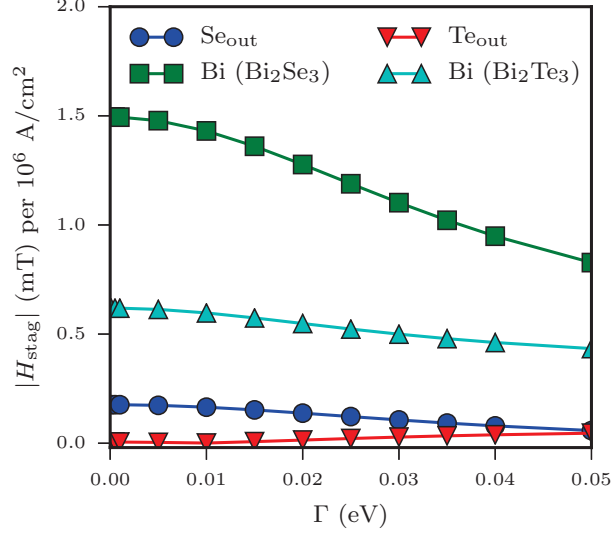


**Figure 3.5** Electric-field-induced staggered magnetic field as a function of the electronic scattering rate in  $\text{Bi}_2\text{Se}_3$  and  $\text{Bi}_2\text{Te}_3$ , at room temperature, for fixed carrier density  $n = 3 \times 10^{19} \text{ cm}^{-3}$  and fixed current density  $J = 10^6 \text{ A/cm}^2$ .

is consistent with the  $R\bar{3}m$  space group symmetry of  $\text{Bi}_2\text{Se}_3$  and  $\text{Bi}_2\text{Te}_3$  (see Appendix A),

$$\chi_E(\mathbf{r}_0) = \begin{pmatrix} 0 & \chi_{xy}(\mathbf{r}_0) & 0 \\ -\chi_{xy}(\mathbf{r}_0) & 0 & 0 \\ 0 & 0 & 0 \end{pmatrix}. \quad (3.7)$$

It follows that  $\mathbf{H}_{\text{stag}} \cdot \mathbf{E} = 0$ , and  $\mathbf{H}_{\text{stag}} = 0$  when  $\mathbf{E} \parallel \hat{z}$ . When the electric field is along  $x$  ( $y$ ), the staggered magnetic field points at  $y$  ( $-x$ ). Once again, inversion partner sites have opposite signs of  $\chi_E(\mathbf{r}_0)$  (see Appendix A).

Figures 3.4, 3.5 and 3.6 display the magnitude of  $\mathbf{H}_{\text{stag}}$  at different nuclei, as a function of the carrier density (for fixed electronic scattering rate  $\Gamma$ ) and as a function of  $\Gamma$  (for fixed carrier density). In Bi, the main contribution to the staggered field comes from the contact term  $\mathbf{H}_{\text{cont}}$ , in part due to the strong atomic spin-orbit coupling. In contrast, in  $\text{Se}_{\text{out}}$  and  $\text{Te}_{\text{out}}$ , which are lighter and have smaller hyperfine couplings,[8] the contact part is suppressed and the orbital part plays a leading role. All these results can be seen in more detail in the figures in Appendix B.

In the metallic regime (Fig. 3.5), the intraband part from Eq. (2.27) dominates. When

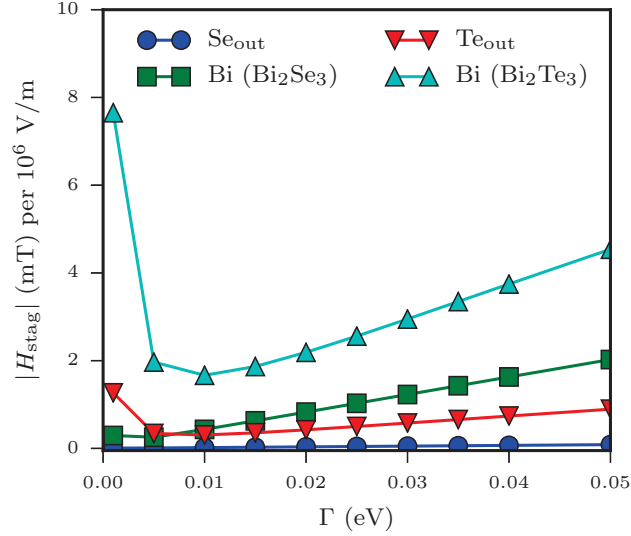


**Figure 3.6** Electric-field-induced staggered magnetic field as a function of the electronic scattering rate in  $Bi_2Se_3$  and  $Bi_2Te_3$ , at room temperature, for fixed carrier density  $n \simeq 10^{15} \text{ cm}^{-3}$  and fixed electric field  $E = 10^6 \text{ V/m}$ . Except for very small values of  $\Gamma$ ,  $H_{stag}$  increases with  $\Gamma$ . This confirms that interband (non Fermi-surface) contributions make the dominant contribution to the staggered field in poorly conducting samples.

the carrier concentration is low (Fig. 3.6), the intraband part dominates as  $\Gamma \rightarrow 0$ , but the interband part takes over as  $\Gamma$  increases. For conducting samples, we choose to represent the staggered field in terms of the current density rather than the electric field. To calculate the current produced by a given electric field for fixed carrier density and electronic scattering rate, we make use of the standard Kubo formula (which, modulo prefactors, amounts to replacing  $\mathbf{O}(\mathbf{r})$  by the velocity operator in Eq. (2.27)). For carrier densities of the order of  $10^{19} \text{ cm}^{-3}$ , a current density of  $10^6 \text{ A/cm}^2$  produces staggered fields of the order of 1 mT at Bi sites. The staggered field is up to an order of magnitude smaller at  $Se_{out}$  and  $Te_{out}$  sites. In experiments, the typical intrinsic linewidth of the Se and Bi NMR peaks is of the order of 10 kHz and 100 kHz, respectively, which in field units is within 0.1 – 1 mT. Thus, for  $J \gtrsim 10^6 \text{ A/cm}^2$ , the staggered fields in Bi and Se can produce peak splittings in excess of the intrinsic linewidth.

Although Figs. 3.4, 3.5 and 3.6 give a quantitative idea for the order of magnitude of  $H_{stag}$ , in reality the electronic scattering rate and the carrier density are not independent variables. In order to obtain more reliable results, we take the carrier densities and resistivities provided by various experiments,[27, 28, 29, 30, 31, 32] and from there calculate the staggered field. The outcome is shown in Fig. 3.7, which displays the dependence of the staggered

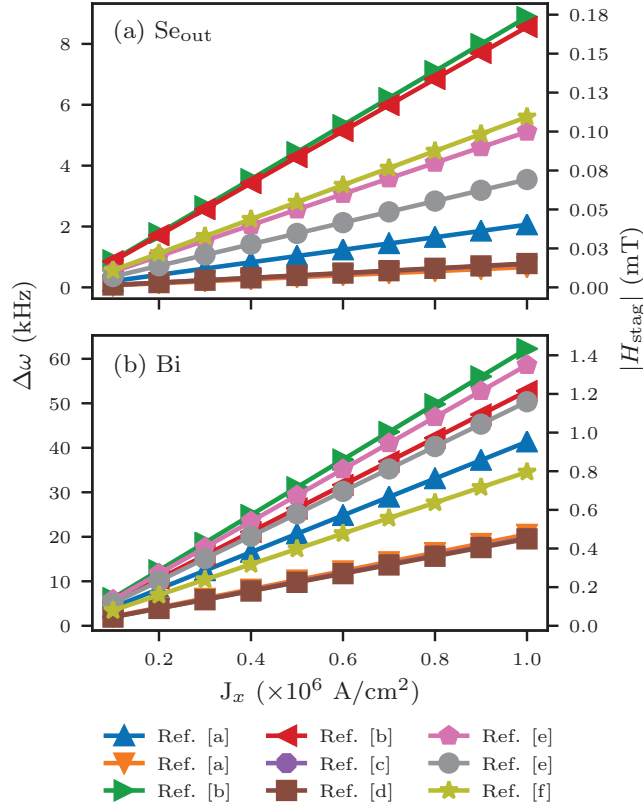


**Figure 3.7** NMR peak splitting for various experimentally reported sample parameters as a function of current density for (a)  $\text{Se}_{\text{out}}$  and (b) Bi, at room temperature. The frequency splitting is defined from Eq. (2.20) as  $\Delta\omega(\mathbf{r}_0) = \gamma(\mathbf{r}_0)|\mathbf{H}_{\text{stag}}(\mathbf{r}_0)|$ .

field on the current density. In the figure, the previous cited experiments are labeled [a]-[f] correspondingly. This figure confirms that sizeable staggered magnetic fields of the order of 1 mT (0.1 mT) can be expected for Bi ( $\text{Se}_{\text{out}}$ ) in conducting samples for current densities of  $10^6 \text{ A/cm}^2$ . In comparison, for similar current densities, the spin-orbit fields in ferromagnetic (Ga, Mn)As and the staggered fields in the antiferromagnetic  $\text{Mn}_2\text{Au}$  are about 0.1 mT.[33, 34]

### 3.2.3 Amperian linewidth and Joule heating

Until now, we have considered the splitting of the resonance peak produced by  $\mathbf{H}_{\text{stag}}$ , while omitting the linewidth produced by the amperian field  $\mathbf{H}_{\text{amp}}$ . In  $\text{Bi}_2\text{Se}_3$  and  $\text{Bi}_2\text{Te}_3$ , the form of  $\chi_E$  is such that the staggered field is perpendicular to the electric field and thus coplanar to the amperian field ( $\mathbf{H}_{\text{amp}} \perp \mathbf{E}$  because  $\mathbf{J} \parallel \mathbf{E}$  in point group  $D_{3d}$  to which  $\text{Bi}_2\text{Se}_3$  and

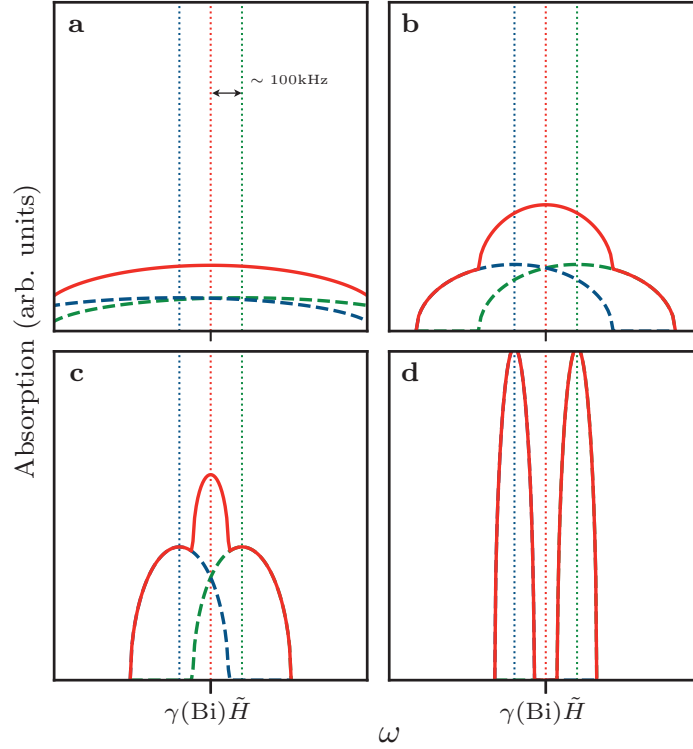


**Figure 3.8** Approximate NMR lineshapes near a  $^{209}\text{Bi}$  resonance peak for a cylindrical wire of radius  $R$ . (a)  $R = 2\mu\text{m}$ , (b)  $R = 1\mu\text{m}$ , (c)  $R = 0.5\mu\text{m}$ , (d)  $R = 0.2\mu\text{m}$ . The vertical dotted lines are guides for the eye indicating  $\tilde{H} \equiv (1 + \chi_H)H_{\text{ext}}$  and  $\tilde{H} \pm H_{\text{stag}}$ . The blue and green dashed lines indicate the separate absorption signals for inversion partner nuclei. The red solid line gives the total measured signal (the sum of the blue and green lines). The electric-field-induced staggered magnetic field splits the resonance frequency of Bi. We take  $H_{\text{stag}} = 2\text{ mT}$  (independent of  $R$ ), which corresponds to a current density of  $\simeq 10^6\text{ A/cm}^2$ , and we use Eqs. (2.31) and (2.32) to model the amperian linewidth. We neglect the intrinsic linewidth because it is typically  $\lesssim 1\text{ mT}$ . For  $R \gtrsim 1\mu\text{m}$ , the effect of the staggered field is masked by the amperian linewidth.

$\text{Bi}_2\text{Te}_3$  belong). Therefore, it is not a good idea to attempt to reduce the amperian linewidth by aligning the external magnetic field with the current, because this would also eliminate the splitting coming from the staggered field (recall Fig. 2.1). Thus, in doped  $\text{Bi}_2\text{Se}_3$  and  $\text{Bi}_2\text{Te}_3$ , both the staggered and amperian fields have to be considered. Moreover, the two scale linearly with the current density, which means that their relative importance will depend on the geometry of the sample. For a wire with a circular cross section and radius  $R$ , the condition for detecting the staggered field in the background of the amperian fields (i.e.  $H_{\text{stag}} \gtrsim H_{\text{amp}}(R)$ ) can be expressed as

$$R \lesssim \frac{\mu_B}{e v_F} \overline{|S_{\mathbf{k}n}(\mathbf{r})|} \quad (3.8)$$

where we have used Eq. (2.29). In sum, it is desirable to have crystals with large hidden spin polarization (strong spin-orbit interaction, large hyperfine coupling) to satisfy condition (3.8) for larger values of  $R$ . In Fig. 3.8, we show how the staggered field on Bi sites becomes detectable for wires whose cross-sectional area is  $\lesssim 1\mu\text{m}^2$ . To detect the staggered field on Se or Te sites, the radius of the wire should be about an order of magnitude smaller. For such small cross-sectional areas, the NMR signal is reduced, and low temperature measurements may be required to compensate for the loss. On a positive side, the wire length can be arbitrarily long; in fact,  $\text{Bi}_2\text{Se}_3$  and  $\text{Bi}_2\text{Te}_3$  nanoribbons of lengths up to several millimeters have already been synthesized and their transport properties measured [35].

Another potential issue with conducting samples and high current-densities is the Joule heating. For a film of thickness  $w$  in contact with an insulating substrate, the change in temperature due to the Joule effect can be roughly estimated as  $\Delta T \simeq J^2 w^2 / (\sigma \kappa)$ , where  $\kappa$  is the thermal conductivity of the electrically insulating substrate. Taking  $J = 10^6 \text{A}/\text{cm}^2$ ,  $\sigma = 10^6 \Omega^{-1}\text{m}^{-1}$ ,  $\kappa = 100 \text{Wm}^{-1}\text{K}^{-1}$  (a sapphire[36] substrate at a few Kelvin) and  $w \simeq 1 \mu\text{m}$ , the Joule heating is rather small ( $\Delta T \simeq 1 \text{K}$ ). Nevertheless, for fixed  $J$ , the Joule heating becomes problematic as the sample thickness exceeds  $10\mu\text{m}$ .

### 3.3 Other materials

---

Given the aforementioned difficulties in  $\text{Bi}_2\text{Se}_3$  and  $\text{Bi}_2\text{Te}_3$ , it is natural to wonder about other materials whose attributes might be more favorable for NMR-based detection of the hidden spin or orbital polarization. The first approach is to try crystals with larger hidden spin polarization, so that the maximum value of  $R$  in Eq. (3.8) becomes larger.  $\text{LaOBiS}_2$  and related compounds[3] could be interesting candidates in that regard.

Another approach is to search for materials where  $\mathbf{H}_{\text{stag}} \cdot \mathbf{E} \neq 0$ . In other words, crystals where  $\chi_E$  has one or more nonzero diagonal elements ( $\chi_{jj} \neq 0$  for one or more values of  $j$ , where  $j \in \{x, y, z\}$ ). In addition to  $\mathbf{H}_{\text{stag}} \cdot \mathbf{E} \neq 0$ , we need the electric current  $\mathbf{J}$  to be parallel to the electric field: together, these two conditions ensure a nonzero staggered field in the direction perpendicular to the amperian field. The objective of this section is to identify materials that meet these criteria. This objective is motivated by the fact that, in materials with  $\mathbf{H}_{\text{stag}} \cdot \mathbf{E} \neq 0$  and  $\mathbf{J} \parallel \mathbf{E}$ , there will be an optimal configuration for the external electric and magnetic fields, shown schematically in Fig. 3.9: with  $\mathbf{H}_{\text{ext}} \parallel \mathbf{E}$ , the amperian linewidth can be largely eliminated (it goes as the square of the electric field) while keeping the effect of the staggered field intact (linear in the electric field).

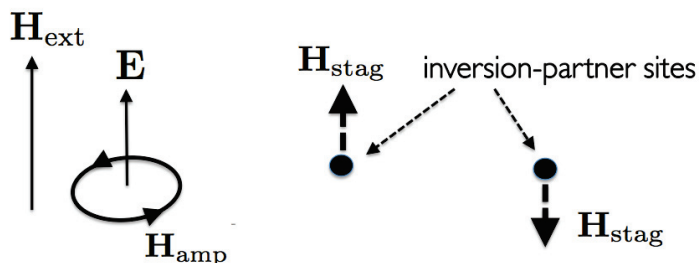


**Figure 3.9** A favorable configuration to probe the hidden spin and orbital polarizations with NMR, in crystals where the macroscopic (unit cell averaged) current is flowing parallel to the electric field  $\mathbf{E}$ , and the staggered field has a nonzero component along the current. This situation is optimal in that the amperian field is perpendicular to the staggered field. Then, if a large external magnetic field is applied parallel to the current, the linewidth from the amperian field is suppressed (it becomes second order in the electric field), while the NMR peak splitting due to the staggered field remains intact (first order in the electric field). This situation can be realized in crystals belonging to monoclinic or higher-symmetry crystal classes, provided that one or more atoms in the unit cell are located at sites whose local symmetries do not contain either inversion or mirror planes.

Before continuing, we remark that the amperian field  $\mathbf{H}_{\text{amp}}$  is a macroscopic (unit cell averaged) quantity. Accordingly, its direction can be determined completely from the knowledge of the point group of the crystal. For a given electric field, the conductivity tensor determines the direction of  $\mathbf{J}$ , which in turn establishes the direction of  $\mathbf{H}_{\text{amp}}$ . In contrast, the staggered field is a local quantity whose variation inside the unit cell plays a major role. Thus, in order to determine the form of  $\chi_E(\mathbf{r}_0)$ , we must use the space group of the crystal.

We are now ready to embark on symmetry arguments. On the one hand, for crystals of monoclinic or higher symmetry (see, for example, Ref. [37]) the macroscopic conductivity tensor is such that  $\mathbf{J} \parallel \mathbf{E}$ , as long as the electric field is applied along a symmetry axis. Here, it suffices to consider the conductivity tensor in the absence of external magnetic fields, because we are interested in the linear response to electromagnetic fields. On the other hand, the crystals allowing for  $\mathbf{H}_{\text{stag}} \cdot \mathbf{E} \neq 0$  must have atoms whose site symmetries contain neither inversion nor (vertical or horizontal) mirror planes. This rule follows from the fact that spin is a pseudovector, while the electric field is a polar vector (see Appendix A for details). In general, we can infer whether a crystal will allow for  $\mathbf{H}_{\text{stag}} \cdot \mathbf{E} \neq 0$  or not from the knowledge of the atomic arrangement in the unit cell (i.e. the Wyckoff positions occupied by the atoms, along with their site symmetries).

From the outset, it must be recognized that many layered semiconductors with hidden polarizations display  $\chi_{ij} \neq 0$  for  $i \neq j$ , but  $\chi_{jj} = 0$ , because all atoms occupy sites whose

local symmetry contains a mirror plane. This is the case in  $\text{Bi}_2\text{Se}_3$  and  $\text{Bi}_2\text{Te}_3$ , in which Bi,  $\text{Se}_{\text{out}}$  and  $\text{Te}_{\text{out}}$  occupy Wyckoff positions  $2c$  of site symmetry  $C_{3v}$ .<sup>[38]</sup> This is also the case in transition metal dihalides<sup>[39]</sup> of the type  $\text{MX}_2$ , where M is a transition metal cation and X is a halogen anion. The same state of affairs applies to layered semiconductors of the type of GaTe.<sup>[40]</sup> Next, we will give several representative examples of centrosymmetric materials with significant spin-orbit interactions, for which  $\chi_{jj}(\mathbf{r}_0) \neq 0$ .

The first proposed example comes from monoclinic transition metal trihalides<sup>[41]</sup> with the  $\text{AlCl}_3$  structure (space group  $C2/m$ ). Among them, we note  $\alpha\text{-RuCl}_3$ , which is a candidate for being a spin liquid.<sup>[42]</sup> In this layered compound, the monoclinic  $C_2$  axis is oriented along  $y$ , and the layers are stacked along  $z$ . Ru atoms occupy Wyckoff positions  $4g$  (site symmetry  $C_2$ ), and the two symmetry-inequivalent Cl atoms (named Cl1 and Cl2) occupy Wyckoff sites  $8j$  (site symmetry 1) and  $4i$  (site symmetry  $C_s$ ), respectively. Hence,  $\chi_{jj}(\text{Ru}) \neq 0$  and  $\chi_{jj}(\text{Cl1}) \neq 0$ , but  $\chi_{jj}(\text{Cl2}) = 0$  because  $C_s$  has a mirror plane. Recent experiments<sup>[43]</sup> have reported  $^{35}\text{Cl}$  NMR data in the absence of electric fields. It would be interesting to see the evolution of the Cl1 NMR shift as a function of an electric field applied along the  $y$  direction (with  $\mathbf{H}_{\text{ext}} \parallel \hat{y}$ ). One drawback of this material is that it is insulating,<sup>[44]</sup> with a room temperature resistivity of the order of  $10^3 \Omega \text{ cm}$ . Hence, the main contribution to the staggered field will come from the deformation of Bloch wave functions by an electric field (the interband part), which will lead to an electric-field-induced change in the hyperfine coupling. Detailed calculations will be required in order to find out the electric fields and the disorder scattering rates for which the staggered field becomes significant.

Another example concerns  $\text{As}_2\text{Se}_3$  and  $\text{As}_2\text{S}_3$  crystals, belonging to the space group  $P2_1/c$ . These are layered compounds, where the monoclinic  $C_2$  axis is perpendicular to the layers.<sup>[45]</sup> The two symmetry-inequivalent As atoms and the three symmetry-inequivalent Se (or S) atoms per unit cell are all located<sup>[46]</sup> at general Wyckoff positions (site symmetry 1). Hence,  $\chi_{jj} \neq 0$  for all atoms. The  $^{77}\text{Se}$  NMR data in the absence of an electric field<sup>[47]</sup> shows three peaks, which correspond to the three inequivalent Se atoms. If an electric field is applied along the monoclinic axis, each of the peaks should split in two. Unfortunately, these compounds have extremely large resistivities,<sup>[48]</sup> especially in the direction perpendicular to the layers ( $\simeq 10^{12} \Omega \text{ cm}$ ), which may make the staggered field too weak.

$\text{SrRuO}_3$  (space group  $Pbnm$ ) and related compounds appear to be much better candidates. For one thing,  $\text{SrRuO}_3$  conducts electricity (with a resistivity of about  $1 \text{ m}\Omega \text{ cm}$  at room temperature<sup>[49]</sup>), and one of its two symmetry-inequivalent oxygens sits in a general Wyckoff position  $8d$  (site symmetry 1).<sup>[50]</sup> For this oxygen,  $\chi_{jj} \neq 0$ . For the rest of the atoms, the site symmetry contains either a non-diagonal mirror plane or inversion, so that  $\chi_{jj} = 0$ . Due to the admixture of  $2s$  electrons at the Fermi level,<sup>[51]</sup> the contribution from the contact

interaction to the staggered field should be significant. Consequently, it will be interesting to measure the evolution of the  $^{17}\text{O}$  resonance frequency under an electric field (once again we suggest applying the electric field along a symmetry axis, with the external magnetic field parallel to it).

As extra examples, we list  $\alpha\text{-Cu}_2\text{Se}$  and  $\text{BaIr}_2\text{Ge}_2$ , both from space group  $P2_1/c$ . In these compounds, all atoms are located in sites whose local symmetry is just the identity.[52] Hence,  $\chi_{jj}(\mathbf{r}_0) \neq 0$  for all atoms. These compounds have rather low resistivities ( $\text{BaIr}_2\text{Ge}_2$  is metallic, while the resistivity of  $\alpha\text{-Cu}_2\text{Se}$  can be as low as  $1\text{ m}\Omega\text{cm}$  at room temperature), and the low-energy electronic states have a significant  $s$ -orbital character, which presages a sizeable staggered field for reasonable electric fields.

Thus far, we have presented examples of materials with significant spin-orbit coupling. In crystals without spin-orbit coupling, the electric-field-induced NMR shift has purely orbital origin (i.e. the contact and dipolar contributions to  $\mathbf{H}_{\text{stag}}$  vanish). This purely orbital shift can be expected to be smaller than that of strongly spin-orbit coupled systems with significant contact hyperfine interaction. However, as we have found in our calculations for  $\text{Bi}_2\text{Se}_3$  and  $\text{Bi}_2\text{Te}_3$ , the orbital component of  $\mathbf{H}_{\text{stag}}$  can attain  $0.1\text{ mT}$  for current densities of  $10^6\text{ A/cm}^2$ , which can by itself leave a fingerprint in the NMR spectrum. Motivated by this, we close this section by proposing a few weakly spin-orbit coupled materials, whose crystal symmetries allow current-induced staggered magnetic fields with a suppressed amperian linewidth. First, we mention organic layered compounds of the type of BEDT-TTF. Several of these compounds[53] are centrosymmetric, conducting, and contain atoms in general Wyckoff positions with site symmetry 1. Second, we bring up the cuprate  $\text{La}_{2-x}\text{Sr}_x\text{CuO}_4$  (space group  $Bmab$ ), which constitutes a Fermi liquid in the overdoped regime. In this compound, one of the two inequivalent oxygens in the unit cell[54] is placed in Wyckoff position  $8e$  (site symmetry  $C_2$ ), which allows for  $\chi_{jj} \neq 0$ .

## Chapter 4

# Future work

Up until this point, we have presented the idea of the hidden spin and orbital polarization and how we could measure them in a rather simple way using nuclear magnetic resonance in an electric field. Particularly, we have shown this idea using a particular material in mind. In this short chapter, we will show two projects that can potentially be worth exploring.

The first project uses the same idea of the whole mémoire. We apply a current to obtain a staggered magnetic response, but this time we apply the ideas and the formalism to silicon, another centrosymmetric crystal.

The second project focuses on a more general idea. Thus far we have calculated a particular magnetic response of an electrical perturbation. Now we ask ourselves about the converse phenomenon: can we get a similar electrical response out of a magnetic perturbation?

The particular motivations and problems will be included in the section devoted for each one.

## 4.1 Hidden orbital polarization in Silicon

---

The reason to use  $\text{Bi}_2\text{Se}_3$  and  $\text{Bi}_2\text{Te}_3$  to apply our ideas of hidden spin and orbital polarizations were mainly motivated by a strong spin-orbit coupling present in these materials. The spin-orbit coupling, discussed in Chapter 1, couples the electric field to the spin degree of freedom. Given that the Bismuth sites, for example, have a strong hyperfine coupling, the contact interaction that dominates the magnetoelectric effect gives hope for its detection with NMR.

From a different perspective, what we are doing with this magnetoelectric effect is to manipulate the resonance frequencies of nuclei in a material. This idea is widely used in the spintronics [34] and quantum computing community. For the latter, there is an approach to quantum computing in which the energy levels of nuclear spins of donors in silicon are manipulated to be able to perform computations [55]. Silicon is used due to the high abundance of  $^{28}\text{Si}$  in nature. Given the spinless nature of the nucleus for this isotope, it provides a good “spin vacuum” for donors in silicon. It means that if a donor (extra proton + electron) such as arsenic or phosphorus with spinful nuclei were to be in this background, the coupling between two of them, remains isolated from a “spin noise”. This means that the energy levels, and thus the resonance frequency to induce transitions between them, of the donors can be controlled with low decoherence. This control is accomplished by using gate voltages in the region of dopants [55].

By virtue of detecting them with NMR, we have shown that it is possible to control the resonance frequencies relative to energy levels that concern nuclear spins. We explore the opportunity to potentially propose another control tool in doped silicon using the source-drain current and the symmetry properties of silicon. However, we find two main complications for the case of silicon:

1. The spin-orbit interaction in silicon is very small (compared to  $\text{Bi}_2\text{Se}_3$  or to the bandgap). This means that the control of the resonance frequency has to come from the orbital degrees of freedom, which we have seen in  $\text{Bi}_2\text{Se}_3$  could be an order of magnitude smaller than the hyperfine coupling present in  $^{209}\text{Bi}$ .
2. The site-symmetry group of the nuclear sites in silicon’s unit cell do not allow for the hidden polarizations to be made visible.

The first difficulty is only really a difficulty until we see the numbers that we can obtain only with the orbital degree of freedom. The second problem is a fundamental one. However,

by inducing strain, we can lower the site symmetries while keeping the global inversion symmetry of the crystal [56]. Therefore, we explore the hidden polarizations produced by an electric field in silicon under strain.

#### 4.1.1 Tight-binding hamiltonian under strain

There are tight-binding models that incorporate strain by modifying the hopping parameters. One can do this by fitting with a power law the hopping  $V_{\mu\nu}$  between orbital  $\mu$  in a site and  $\nu$  in a different site[57]:

$$V_{\mu\nu}(d) = V_{\mu\nu}(d_0) \left(\frac{d}{d_0}\right)^{\eta_{\mu\nu}}, \quad (4.1)$$

where  $d$  is the distance between sites after the strain,  $d_0$  is the unstrained distance and  $\eta_{\mu\nu}$  is the Harrison parameter.

Because of the widespread use of semiconductors, sophisticated tight-binding models that incorporate ten orbitals ( $s, s^*, p_x, p_y, p_z, d_{xy}, d_{yz}, d_{zx}, d_{x^2-y^2}, d_{3z^2-r^2}$ ) have been developed to replicate with detail the realistic band structure of cubic semiconductors[58].

Combining these two facts, a sophisticated ten-orbital tight binding model for silicon with the possibility to add strain was constructed in Ref. [59]. It incorporates strain for the hopping parameters that involve different sites with the Harrison parameters, as in equation (4.1). However, for the onsite matrix elements in the model, they develop a first-order expansion of the crystal potential as a function of the atomic positions, thus incorporating strain in microscopic detail. We took this tight-binding model, reported in Ref. [59], to build the basis to expand the Bloch functions of silicon that now depend on strain.

Silicon has two atoms per unit cell, which lets us define two sublattices of the crystal. The space group for silicon is the symmorphic  $Fd\bar{3}m$ . The site-symmetry group for both sites is  $\bar{4}3m$ . The inversion symmetry is hidden in the rotoinversion axis  $\bar{4}$ . Each of the sublattices has one atom per unit cell, and we expect that by locally breaking the inversion symmetry by means of a uniaxial strain, the hidden polarizations will give us a magnetic response that is opposite across the sublattices. Without going into much detail, the most important piece of information comes with the dependence of the atomic positions with strain. In a homogeneously strained crystal, these new positions  $\mathbf{R}_i$  for site  $i$ , as a function of the unstrained positions  $\mathbf{R}_i^0$ , are given by the following equation,

$$\mathbf{R}_i = (\hat{\mathbf{I}} + \hat{\epsilon})\mathbf{R}_i^0 \pm \zeta \frac{a}{4} (\epsilon_{yz}, \epsilon_{zx}, \epsilon_{xy}) \quad (4.2)$$

where the + (respectively, the -) corresponds to the the sublattice 1 (sublattice 2),  $\zeta$  is a

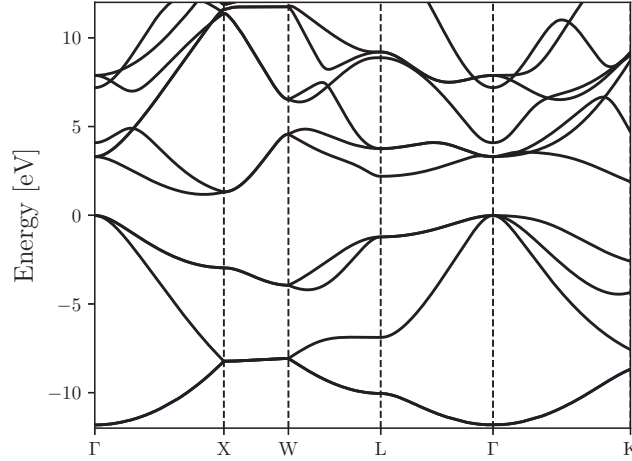


**Figure 4.1** Relaxed silicon band structure computed from the tight-binding approximation from Ref. [59]. We see the indirect band gap happening between the valence band maximum at  $\mathbf{k} = \Gamma$  and one of the conduction band minima at  $\mathbf{k} = X$ .

phenomenological internal strain parameter,  $a$  is silicon's lattice parameter,  $\hat{I}$  is the identity matrix and  $\hat{\epsilon}$  is the matrix of strains. As we can see, the second term is only non-zero when there are nonzero off-diagonal strain matrix elements. This means that  $\zeta$  describes the motion of one sublattice with respect to the other under shear strain.

#### 4.1.2 Preliminary results

Fig. 4.1 shows the band structure of the silicon crystal using the tight-binding method under no strain. We can reproduce the  $\sim 2$  eV indirect band gap between the valence band maximum at  $\mathbf{k} = \Gamma$  and one of the conduction band minima at  $\mathbf{k} = X$ .

We then go ahead and apply all the formalism described in Chapters 1, 2 and 3. To do this, however, we need the information about the wavefunctions at the nucleus, for a nucleus that interests us. Because we already have this information for  $^{209}\text{Bi}$ , we provide results for Bi-doped silicon. Fig. 4.2 shows the staggered magnetic field obtained when we induce a uniaxial strain along the  $[001]$  direction for two values of strain, 5% compression and 5% elongation. We show the  $x$  component of the staggered magnetization; all the other components are orders of magnitude smaller. We note that in this case the applied current and the staggered magnetic field are parallel (and antiparallel), which helps us get rid of the amperian field. However, the induced staggered magnetization is one order of magnitude smaller than the best case scenario in  $\text{Bi}_2\text{Se}_3$  for the same applied current.

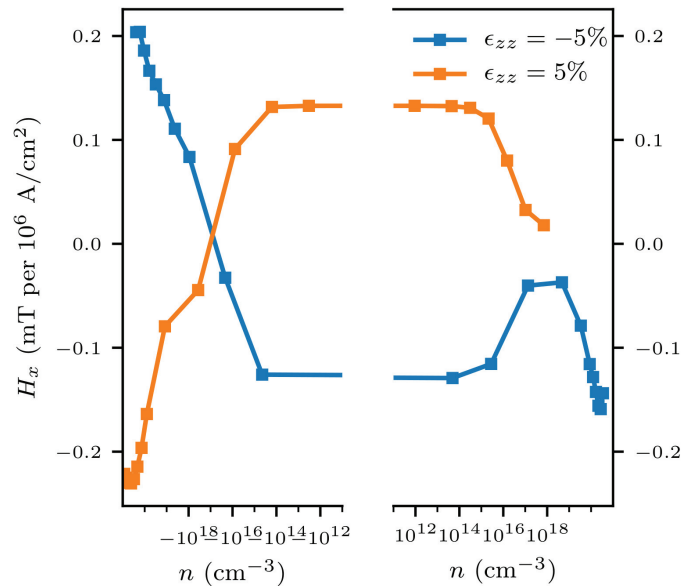


**Figure 4.2** Magnetic response in one sublattice as a function of carrier density for two fixed values of strain. All other components of the magnetization are orders of magnitude smaller. The applied current is in the same direction as the response.

Finally, fig. 4.3 shows the staggered magnetization response as a function of strain percentage for two fixed values of carrier density (in one, chemical potential crosses the conduction band (CB), and in the other it crosses the valence band (VB)). We clearly see that when there is no strain induced in the crystal, the staggered magnetization goes to zero.

With these results we confirm the need of strain in the silicon crystal to induce a staggered magnetic field with a current. The best order of magnitude of this staggered field that we can obtain for Bi is  $\sim 0.1$  mT with a current density of  $10^6$  A/cm<sup>2</sup>. There are many other questions that we want to explore:

- Is it possible to presently apply this current in silicon samples?
- Is there an advantage to effectively substitute the gate voltages by strains?
- What's the dependence of this staggered magnetic field with other types of strains?

It is in our intentions to talk with experimentalists if it is a research avenue worth pursuing.

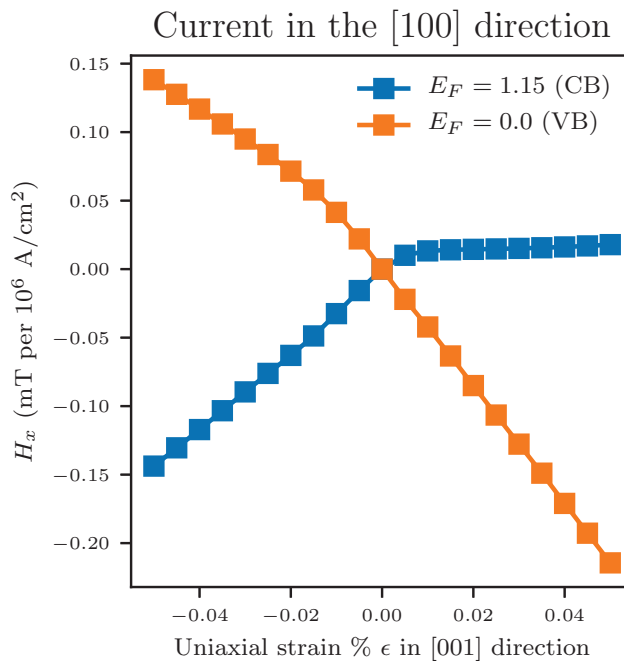


**Figure 4.3** Magnetic response in one sublattice as a function of strain for two fixed values of chemical potential. The applied current is in the same direction as the response. CB stands for conduction band and VB stands for valence band.

## 4.2 Hidden electrical polarization under external magnetic field

We have shown that there exists a hidden magnetic polarization at nuclear sites in centrosymmetric crystal that can be rendered visible by means of an electric field: both by changing the electronic band populations and the electronic wavefunctions. Given the nature of this magnetoelectric effect, we venture into the question of finding local electric dipole moments inside a unit cell under a magnetic field – that is, a converse effect, where now the perturbation is magnetic and the local response is of electric nature.

The particular motivation for this project comes from (presently unpublished) NMR data of the  $^{209}\text{Bi}$  sites in  $\text{Bi}_2\text{Se}_3$ . In chapter 2, we presented the theory of NMR that is valid for any spinful nucleus. However, if the total half-integer spin of the nucleus exceeds  $1/2$ , a phenomenon called “quadrupolar splitting” arises. For a detailed explanation, see Chapter 10 of Ref. [18].

Basically, if there is a non-spherical distribution of charge in the nucleus, there could be an effective electrostatic energy associated with the orientation of this distribution of charge. This distribution of charge can be carried out into a multipole expansion. It can be

shown that the quadrupole moment interaction with the electric field gradients shifts the resonance frequencies for transitions between nuclear spin projections  $m_I > 1/2$ . Therefore, if we have a nucleus with a nuclear spin  $I > 1/2$ , the resonance spectrum gets additional peaks coming from the other shifted energy levels. This quadrupolar interaction depends highly on the orientation of the external magnetic field relative to the principal axes of the crystal. This angular dependence allows a “magic angle” at which all the splitting due to quadrupolar coupling vanishes. Given that the nuclear spin of bismuth is  $I = 9/2$ , the NMR spectrum for this site, away from the magic angle, gets 8 extra peaks [24]. At exactly the magic angle, we should only get the main resonance line.

This project is meant to try to look at the influence of a possible extra electric field gradient produced at a bismuth site by the coupling between the external magnetic field and the dipole moments of the surrounding atoms. This could affect the resonance spectrum for nuclear spins higher than  $9/2$  even at the magic angle, depending on the crystal symmetries.

#### 4.2.1 Local dipole moment operator

Classically, we know that an electric dipole is formed when there are two opposite charges are very close to each other. This classic idea of “dipole” can be extended, and when we consider a more complex charge distribution, whose electric field can be expanded in a series of moments. The second moment is the dipole moment and serves as a first approximation to compute complex charge distributions by looking at them from far away, where in the zeroth order approximation we just look at the total charge as a point charge. For a continuous charge distribution  $\rho(\mathbf{r})$ , its dipole moment  $\mathbf{p}$  is defined as

$$\mathbf{p} = \int_V d^3r \rho(\mathbf{r}) \mathbf{r}.$$

When  $\rho(\mathbf{r}) = \sum_{i=1}^N q_i \delta(\mathbf{r} - \mathbf{r}_i)$ , and  $N = 1$ , we get the classical expression for a dipole moment  $\mathbf{p} = q\mathbf{d}$ . The electric field at point  $\mathbf{R}$ , measured from the origin, associated with a dipole is

$$\mathbf{E}(\mathbf{R}) = \frac{3(\mathbf{p} \cdot \mathbf{R})\mathbf{R} - \mathbf{p}}{4\pi\epsilon_0 R^3}. \quad (4.3)$$

Let us now write our charge density as a quantum-mechanical operator,

$$\rho(\mathbf{r}) = q\psi^\dagger(\mathbf{r})\psi(\mathbf{r}) = q \sum_{k,k'} \sum_{n,n'} \psi_{k,n}^*(\mathbf{r})\psi_{k',n'}(\mathbf{r})c_{k,n}^\dagger c_{k',n'}.$$

We then want to compute the expectation value of our dipole moment operator,

$$\langle \mathbf{p} \rangle = q \int d^3r \mathbf{r} \sum_{\mathbf{k},n} \psi_{\mathbf{k},n}^*(\mathbf{r}) \psi_{\mathbf{k},n}(\mathbf{r}) f_{\mathbf{k},n},$$

where  $f_{\mathbf{k},n}$  is the Fermi-Dirac distribution that comes about when we take the expectation value of the number operator in the non-interacting case. We then make use of a closure relation to get to a normal expectation value of an operator using wavefunctions expanded in a  $\mathbf{k}$ -space basis,

$$\langle \mathbf{p} \rangle = q \sum_{\mathbf{k},n} \langle \mathbf{k}, n | \mathbf{r} | \mathbf{k}, n \rangle f_{\mathbf{k},n}.$$

We will, however, define a “local” electric dipole moment operator by projecting onto a site  $\mathbf{r}_0$ ,

$$\langle \mathbf{p}(\mathbf{r}_0) \rangle = q \sum_{\mathbf{k},n} \langle \mathbf{k}, n | \mathbf{r} | \mathbf{r}_0 \rangle \langle \mathbf{r}_0 | \mathbf{k}, n \rangle f_{\mathbf{k},n}. \quad (4.4)$$

#### 4.2.2 Matrix elements in the tight-binding basis

Given that we have a tight-binding approximation, we want to find the matrix elements of our local dipole moment operator in this basis,

$$| \mathbf{k} n \rangle = \sum_{j_0, \mu, \sigma} | \mathbf{k} j_0 \mu \sigma \rangle \langle \mathbf{k} j_0 \mu \sigma | \mathbf{k} n \rangle.$$

Since we want to know what will be the real-space projection on these states, we expand in a real-space basis, knowing  $\langle \mathbf{R} j_0 \mu \sigma | \mathbf{k} j_0 \mu \sigma \rangle = \frac{1}{\sqrt{N}} e^{i\mathbf{k} \cdot \mathbf{R}}$ ,

$$| \mathbf{k} j \mu \sigma \rangle = \frac{1}{\sqrt{N}} \sum_{\mathbf{R}} e^{i\mathbf{k} \cdot \mathbf{R}} | \mathbf{R} j \mu \sigma \rangle.$$

Therefore, the matrix elements will be given by

$$\langle \mathbf{k} n | \mathbf{r} | \mathbf{r}_0 \rangle \langle \mathbf{r}_0 | \mathbf{k}' n' \rangle = \frac{1}{N} \sum_{\mathbf{R}, \mathbf{R}'} e^{i(\mathbf{k} \cdot \mathbf{R} - \mathbf{k}' \cdot \mathbf{R}')} \sum_{\substack{j, \mu, \sigma \\ j', \mu', \sigma'}} \langle \mathbf{k} n | \mathbf{k} j \mu \sigma \rangle \langle \mathbf{R} j \mu \sigma | \mathbf{r} | \mathbf{r}_0 \rangle \langle \mathbf{r}_0 | \mathbf{R}' j' \mu' \sigma' \rangle \langle \mathbf{k}' j' \mu' \sigma' | \mathbf{k}' n' \rangle.$$

The real-space projection selects a nuclear site with coordinates  $\mathbf{R}_0$  for the Bravais lattice vector and  $\mathbf{t}_{j_0}$  for specific site within a unit cell,  $\mathbf{r}_0 = \mathbf{R}_0 + \mathbf{t}_{j_0}$ . Because all unit cells are

**Table 4.1** Hidden electric dipole moment for the different sites in Bi<sub>2</sub>Se<sub>3</sub> under no perturbation.

Lattice site	$\hat{z}$ -component of $\langle \mathbf{p}(\mathbf{r}_0) \rangle$ ( $\times 10^{-37}$ C m)	in Debyes ( $\times 10^{-8}$ D)
Se <sub>in</sub>	0	0
Se <sub>out</sub>	1.1828	3.5456
Bi	3.9705	11.902
Bi'	-3.9705	-11.902
Se <sub>out</sub>	-1.1828	-3.5456

identical, we can just choose  $\mathbf{R}_0 = 0$ . Therefore,

$$\langle \mathbf{k}n | \mathbf{r} | \mathbf{r}_0 \rangle \langle \mathbf{r}_0 | \mathbf{k}'n' \rangle = \frac{1}{N} e^{i(\mathbf{k}-\mathbf{k}') \cdot \mathbf{r}_0} \sum_{\substack{\mu, \sigma \\ \mu', \sigma'}} \langle \mathbf{k}n | \mathbf{k}j_0\mu\sigma \rangle \langle \mathbf{0}j_0\mu\sigma | \mathbf{r} | \mathbf{0}j_0\mu'\sigma' \rangle \langle \mathbf{k}'j_0\mu'\sigma' | \mathbf{k}'n' \rangle. \quad (4.5)$$

Let us focus on the intra-atomic dipole matrix elements in our tight-binding basis,

$$\mathbf{p}_{\mu, \mu'}^{j_0} = e \langle \mathbf{0}j_0\mu\sigma | \mathbf{r} | \mathbf{0}j_0\mu'\sigma' \rangle = e \int d^3r \psi_{\mu}^*(\mathbf{r}_0) \mathbf{r} \psi_{\mu'}(\mathbf{r}_0) \delta_{\sigma, \sigma'}, \quad (4.6)$$

where the  $\psi_{\mu}(\mathbf{r}_0)$  is the electronic wavefunction around the nuclear site  $\mathbf{r}_0$ , which can be calculated through DFT, atomic DFT, or in a hydrogen-like approximation.

#### 4.2.3 Preliminary results

We then use eq. (4.5) for  $\mathbf{k}', n' = \mathbf{k}, n$  to compute the expectation value of the intra-atomic dipole moment in the absence of an external field, eq. (4.4). We still need the information about the radial part of the wavefunction, which for now we approximate with a hydrogen-like atom with radial wavefunctions that only differ from hydrogen by the appropriate atomic number. We can therefore compute the integral in eq. (4.6) for all the atoms in Bi<sub>2</sub>Se<sub>3</sub>. Using  $N = V_{\text{cell}}/V_{\text{crystal}}$ , we get Table 4.1, where we show only the  $z$  component. All the other components are zero.

We see that even in the absence of magnetic field, there is already a staggered dipole moment within a unit cell. Because it is compensated in each unit cell, there is no net electrical polarization. The symmetries thus allow a nonzero electric dipole in the  $z$  direction that is nevertheless 8 orders of magnitude smaller compared to the dipole moment of water (in the

order of 1 Debye).

The present state of affairs in this research avenue is to implement the linear response of this quantity with the magnetic field, which we have done before in the case of the magnetic response to evaluate the NMR shifts in conventional setups [8].

- Find  $\chi_E(\mathbf{r}_0)$  in the relation  $\langle \mathbf{p}(\mathbf{r}_0) \rangle = \chi_E(\mathbf{r}_0) \cdot \mathbf{H}$ , where  $\mathbf{H}$  is the external field. Confirm that its matrix elements obey the symmetry restrictions of the crystal. Compare this correction to the local dipole moment with the “permanent” one.
- Estimate the electric field gradient produced by the dipole moments.
- Evaluate if the interaction with the nuclear quadrupole moment can lift the degeneracy of the nuclear energy levels at the magic angle.

# Conclusion

Throughout this mémoire, we have looked into the implications that symmetries have on the physical manifestations of certain phenomena. In particular, this reasoning applies in the quantum-mechanical formalism of crystals. From a microscopic perspective, the energies and wavefunctions that describe electrons moving in a crystal are restricted by the symmetries of the problem.

In chapter 1, we have seen that two particular symmetries, inversion and time-reversal, render every Bloch band at least two-fold degenerate everywhere in reciprocal space. This has profound implications on the spin angular momentum expectation value across bands, as well as for the orbital angular momentum. We have shown that when looking at real-space sectors, we could extract information about the spin and angular polarizations of bands. By analyzing their properties, we have seen that these polarizations are hidden in two ways. To try to obtain a measurement, we have proposed nuclear magnetic resonance in an electric field to probe this local effect that compensates within a unit cell.

In chapter 2, we have completed a quantitative theory of the NMR shifts that arise when we allow the probed nuclear sites to talk to their electronic surroundings. In particular, we have looked at the calculation of the electrically induced NMR shifts, as well as some potential problems related to amperian magnetic fields. The basis of our proposal is that, under an electric field, the NMR peaks corresponding to sites away from the inversion center should be split into two.

In chapter 3, we have applied these ideas to a particular set of crystals whose electronic wavefunctions show strong spin-orbit interaction. To do this, we adapted an existing tight-binding model for these materials and computed all the quantities defined in chapter 2. The most important result that we find is that we could observe the hidden polarizations with this method in this material if many particular constraints are met. We conclude that these materials are not ideal mainly because the electrically induced staggered magnetic field is perpendicular to the current. This fact makes it more difficult to observe the NMR

peak splitting experimentally because one must contend with the linewidth generated by the circulating amperian magnetic fields. We have discussed two possible solutions to this problem. One is to use wires with small cross sectional areas. Another option is to use other materials, whose crystal symmetry allows to have the staggered field perpendicular to the amperian field. The ideal systems would be highly conducting, strongly spin-orbit coupled, with significant  $s$ -orbital admixture near the Fermi level, and would have some atoms whose site symmetries lack inversion and non-diagonal mirror planes. There exist materials, like  $\text{SrRuO}_3$  and  $\text{BaIr}_2\text{Ge}_2$ , that appear to satisfy all of these requirements.

Although the electrically induced splitting of NMR resonance peaks predicted in this work has not been reported thus far, partially related effects are known in the semiconductor and quantum information literature.

On the one hand, in silicon-based qubits,[60] an electric field modifies the hyperfine coupling of a donor nuclear spin-electron system placed in proximity to a gate, thereby shifting the resonance frequency in a controllable way. This effect is formally similar to the interband contribution discussed in our work, which also captures the change in the local field originating from the electric-field-induced deformation of the electronic wave functions. That said, there are several differences. First, our formalism involves many electrons, as opposed to just one in silicon qubits. For that reason, the intraband (Fermi-surface) contribution, which plays a major role in our theory, is not present in silicon qubit proposals. Second, in our case the magnitude and direction of  $\mathbf{H}_{\text{stag}}$  depend on the local symmetry at the location of the nucleus; such symmetry considerations do not play a role in existing silicon qubit proposals.

On the other hand, there exists a large body of theoretical and experimental work [61, 62] concerning electric-field effects in electron spin resonance (ESR). For instance, in spin-orbit coupled systems with broken inversion symmetry, an electric field can lead to an electronic spin polarization, which modulates (or induces, in the case of ac electric fields) ESR. Our idea differs from this line of work in that we are focused on nuclear spin resonance. In centrosymmetric and non-magnetic crystals,  $\mathbf{H}_{\text{stag}}$  averages to zero inside a unit cell. Thus, for itinerant electron systems, the shift in the ESR frequency due to  $\mathbf{H}_{\text{stag}}$  should vanish in the bulk.

Finally, in chapter 4, we have discussed possible extensions of our work that imply short- and long-term projects. First, we have found it would be interesting to explore the impact (if any) of hidden spin and orbital polarizations in the manipulation of spin qubits. Secondly, we explored the idea of the converse effect happening in centrosymmetric crystal – namely, an electrical response from a magnetic perturbation.

## Annexe A

# Symmetry constraints in the form of the magnetoelectric tensor

In this Appendix, we show how symmetry operations of the space group of the crystal determine the form of  $\chi_E$ . For concreteness, we will study the transformation properties of a related but simpler quantity,

$$\begin{aligned} \tilde{\chi}_{ij}(\mathbf{r}) = & \sum_{\mathbf{k}n n'} \langle \psi_{\mathbf{k},n} | S_i(\mathbf{r}) | \psi_{\mathbf{k},n'} \rangle \langle \psi_{\mathbf{k},n'} | v_j | \psi_{\mathbf{k},n} \rangle \\ & \times F(E_{\mathbf{k},n}, E_{\mathbf{k},n'}), \end{aligned} \quad (\text{A.1})$$

where  $i, j \in \{x, y, z\}$  and  $F(E_{\mathbf{k},n}, E_{\mathbf{k},n'})$  is a function only of energies of Bloch states (as well as their broadening parameter  $\Gamma$ ). The tensor  $\chi_E(\mathbf{r})$  transforms in the same way as  $\tilde{\chi}$  under space group operations, because internal magnetic fields transform in the same way as spins (both are pseudovectors).

Let  $R$  be a symmetry operation of the non-magnetic crystalline space group. Under this operation, a wave vector  $\mathbf{k}$  changes to  $R\mathbf{k}$ , with  $E_{R\mathbf{k},n} = E_{\mathbf{k},n}$ . In addition,[15]  $R|\psi_{\mathbf{k}n}\rangle = U_{\mathbf{k}n}|\psi_{R\mathbf{k},n}\rangle$ , where  $U_{\mathbf{k}n}$  is a unitary matrix acting on the twofold degenerate subspace of band  $n$  at momentum  $\mathbf{k}$  (it also includes the phase factors from non-symmorphic symmetry

operations). Inserting  $R^{-1}R = \mathbf{1}$  in Eq. (A.1), we can write

$$\begin{aligned}
\tilde{\chi}_{ij}(\mathbf{r}) &= \sum_{\mathbf{k}n n'} \langle \psi_{R\mathbf{k},n} | RS_i(\mathbf{r})R^{-1} | \psi_{R\mathbf{k},n'} \rangle \langle \psi_{R\mathbf{k},n'} | Rv_j R^{-1} | \psi_{R\mathbf{k},n} \rangle F(E_{\mathbf{k}n}, E_{\mathbf{k}n'}) \\
&= \sum_{R\mathbf{k},n n'} \langle \psi_{R\mathbf{k},n} | RS_i(\mathbf{r})R^{-1} | \psi_{R\mathbf{k},n'} \rangle \langle \psi_{R\mathbf{k},n'} | Rv_j R^{-1} | \psi_{R\mathbf{k},n} \rangle F(E_{R\mathbf{k},n}, E_{R\mathbf{k},n'}) \\
&= \sum_{\mathbf{k}n n'} \langle \psi_{\mathbf{k}n} | RS_i(\mathbf{r})R^{-1} | \psi_{\mathbf{k}n'} \rangle \langle \psi_{\mathbf{k}n'} | Rv_j R^{-1} | \psi_{\mathbf{k}n} \rangle F(E_{\mathbf{k}n}, E_{\mathbf{k}n'}). \tag{A.2}
\end{aligned}$$

In the first line of Eq. (A.2), the matrix  $U$  has been removed by a gauge transformation (this is always possible because  $\tilde{\chi}_{ij}$  is gauge invariant). In the second line, we have used the fact  $\sum_{\mathbf{k}} f(\mathbf{k}) = \sum_{\mathbf{k}} f(R\mathbf{k}) = \sum_{R\mathbf{k}} f(\mathbf{k})$  for any function  $f(\mathbf{k})$  because  $\mathbf{k}$  and  $R\mathbf{k}$  contain the same momenta (only the ordering differs, but the sum is independent of the ordering). In the third line, we have made a change of variables  $R\mathbf{k} \rightarrow \mathbf{k}$ .

Armed with Eq. (A.2), one can find out how various symmetry operations constrain the form of  $\tilde{\chi}$ . To begin, let us consider the spatial inversion operator,  $R = I$ . In this case,

$$IS_i(\mathbf{r})I^{-1} = I \frac{\sigma_i}{2} I^{-1} I |\mathbf{r}\rangle \langle \mathbf{r}| I^{-1} = \frac{\sigma_i}{2} |\mathbf{r}'\rangle \langle \mathbf{r}'| = S_i(\mathbf{r}'), \tag{A.3}$$

where we have used the fact that spin is a pseudovector and  $\mathbf{r}' = I\mathbf{r}$  is the inversion partner of  $\mathbf{r}$ . Since velocity is a polar vector,  $Iv_j I^{-1} = -v_j$ . Hence, from Eq. (A.2), we get

$$\tilde{\chi}_{ij}(\mathbf{r}) = -\tilde{\chi}_{ij}(\mathbf{r}'). \tag{A.4}$$

This shows that  $\chi_E$  takes the opposite sign at inversion partner sites, a fact that we have repeatedly mentioned in the main text. In particular, if the site symmetry of the atom includes inversion, i.e. if  $\mathbf{r}' = \mathbf{r}$ , we are led to  $\chi_E(\mathbf{r}) = -\chi_E(\mathbf{r}) = 0$ .

Let us now consider a rotation by an angle  $\phi$  around the  $z$  axis. For an  $n$ -fold axis,  $\phi = 2\pi/n$ , the operators transform as

$$\begin{aligned}
C_\phi S_i(\mathbf{r}) C_\phi^{-1} &= e^{i\frac{\sigma_z}{2}\phi} \frac{\sigma_i}{2} e^{-i\frac{\sigma_z}{2}\phi} C_\phi |\mathbf{r}\rangle \langle \mathbf{r}| C_\phi^{-1} \\
C_\phi v_j C_\phi^{-1} &= e^{i\frac{\sigma_z}{2}\phi} v_j e^{-i\frac{\sigma_z}{2}\phi}. \tag{A.5}
\end{aligned}$$

In the second line,  $v_j$  must be understood as a vector whose only nonzero component is the  $j$ -th component. If  $C_\phi \mathbf{r}$  and  $\mathbf{r}$  are equivalent sites (i.e. if the site symmetry at  $\mathbf{r}$  contains the

$C_\phi$  operation), the local spin operator transforms as

$$\begin{aligned} S_x(\mathbf{r}) &\rightarrow S_x(\mathbf{r}) \cos \phi + S_y(\mathbf{r}) \sin \phi \\ S_y(\mathbf{r}) &\rightarrow -S_x(\mathbf{r}) \sin \phi + S_y(\mathbf{r}) \cos \phi \\ S_z(\mathbf{r}) &\rightarrow S_z(\mathbf{r}). \end{aligned} \quad (\text{A.6})$$

The velocity operator transforms similarly. It then follows from Eq. (A.2) that  $\tilde{\chi}_{xz}(\mathbf{r}) = \tilde{\chi}_{xz}(\mathbf{r}) \cos \phi + \tilde{\chi}_{yz}(\mathbf{r}) \sin \phi$  and  $\tilde{\chi}_{yz}(\mathbf{r}) = -\tilde{\chi}_{xz}(\mathbf{r}) \sin \phi + \tilde{\chi}_{yz}(\mathbf{r}) \cos \phi$ . When  $\phi \neq 0 \pmod{2\pi}$ , the only solution for these two equations is  $\tilde{\chi}_{xz}(\mathbf{r}) = \tilde{\chi}_{yz}(\mathbf{r}) = 0$ . Likewise, one can show that  $\tilde{\chi}_{zj}(\mathbf{r}) = 0$  for  $j \in \{x, y\}$ . Similarly, another consequence of the  $C_\phi$  axis is that

$$\begin{aligned} (\tilde{\chi}_{xx}(\mathbf{r}) - \tilde{\chi}_{yy}(\mathbf{r})) \sin^2 \phi &= (\tilde{\chi}_{xy}(\mathbf{r}) + \tilde{\chi}_{yx}(\mathbf{r})) \sin \phi \cos \phi \\ (\tilde{\chi}_{xx}(\mathbf{r}) - \tilde{\chi}_{yy}(\mathbf{r})) \sin \phi \cos \phi &= -(\tilde{\chi}_{xy}(\mathbf{r}) + \tilde{\chi}_{yx}(\mathbf{r})) \sin^2 \phi. \end{aligned}$$

If  $\sin \phi = 0$  ( $C_2$  axis), these two equations are trivially satisfied. However, if  $\sin \phi \neq 0$ , they enforce  $\tilde{\chi}_{xx}(\mathbf{r}_0) = \tilde{\chi}_{yy}(\mathbf{r}_0)$  and  $\tilde{\chi}_{xy}(\mathbf{r}_0) = -\tilde{\chi}_{yx}(\mathbf{r}_0)$ . Such is the case of Bi, Se<sub>out</sub> and Te<sub>out</sub> sites in Bi<sub>2</sub>Se<sub>3</sub> and Bi<sub>2</sub>Te<sub>3</sub>, whose site symmetries contain a  $C_3$  axis along  $z$ .

Next, let us consider an atomic site  $\mathbf{r}$  whose local symmetry contains a mirror plane. For concreteness, let us suppose that the mirror is perpendicular to the  $y$  axis. Under this mirror,  $S_x(\mathbf{r}) \rightarrow -S_x(\mathbf{r})$  and  $v_x \rightarrow v_x$ , which implies that  $\tilde{\chi}_{xx}(\mathbf{r}) = -\tilde{\chi}_{xx}(\mathbf{r}) = 0$ . Likewise,  $S_y(\mathbf{r}) \rightarrow S_y(\mathbf{r})$  and  $v_y \rightarrow -v_y$ , which means that  $\tilde{\chi}_{yy}(\mathbf{r}) = -\tilde{\chi}_{yy}(\mathbf{r}) = 0$ . Also,  $S_z(\mathbf{r}) \rightarrow -S_z(\mathbf{r})$  and  $v_z \rightarrow v_z$ , which leads to  $\tilde{\chi}_{zz}(\mathbf{r}) = -\tilde{\chi}_{zz}(\mathbf{r}) = 0$ . In sum, a site symmetry containing a mirror plane that is perpendicular to either the  $x$ ,  $y$  or  $z$  axis imposes  $\tilde{\chi}_{jj}(\mathbf{r}) = 0$ , a result that we have utilized in the main text. This kind of situation arises in Bi<sub>2</sub>Se<sub>3</sub> and Bi<sub>2</sub>Te<sub>3</sub>, where Bi, Se<sub>out</sub> and Te<sub>out</sub>. In contrast, if the site symmetry contains a diagonal mirror (not perpendicular to neither  $x$ ,  $y$  nor  $z$  axes), it is no longer true that  $\tilde{\chi}_{jj}(\mathbf{r}) = 0$ .

A mirror plane can also constrain the off-diagonal matrix elements of  $\chi_E$ . For example, a site symmetry including a mirror perpendicular to the  $y$  axis yields  $\tilde{\chi}_{xz}(\mathbf{r}) = 0$ , because  $S_x(\mathbf{r}) \rightarrow -S_x(\mathbf{r})$  and  $v_z \rightarrow v_z$  under the said mirror. Likewise,  $S_z(\mathbf{r}) \rightarrow -S_z(\mathbf{r})$  and  $v_x \rightarrow v_x$  translate into  $\tilde{\chi}_{zx}(\mathbf{r}) = 0$ . In contrast,  $\tilde{\chi}_{xy}(\mathbf{r})$  and  $\tilde{\chi}_{yz}(\mathbf{r})$  are allowed to be nonzero. The presence of additional mirror operations in the site symmetry group will add further zeros in  $\chi_E$ . For example, if two mirror planes exist, one perpendicular to  $x$  and one perpendicular to  $y$ ,  $\tilde{\chi}_{yz}(\mathbf{r}) = 0$ , though  $\tilde{\chi}_{xy}(\mathbf{r})$  is still allowed to be nonzero (essentially because  $S_x$  and  $v_y$  transform in the same way under both mirrors). In Bi<sub>2</sub>Se<sub>3</sub> and Bi<sub>2</sub>Te<sub>3</sub>, where all mirror planes at the locations of Bi, Se<sub>out</sub> and Te<sub>out</sub> contain the  $z$  axis,  $\chi_{xy}(\mathbf{r}) \neq 0$  is allowed.

## Annexe B

# Spin and orbital contributions to the staggered magnetization

Figs. B.1 and B.2 shows the contributions to the staggered magnetic field, shown in Eq. (2.22), at the Bi and  $\text{Se}_{\text{out}}$  in  $\text{Bi}_2\text{Se}_3$ , as a function of the carrier density. As referenced in the text, the contact interaction is the larger of the contributions at the Bi sites, due to the large hyperfine coupling of bismuth. However, the dipolar interaction becomes the predominant one for  $\text{Se}_{\text{out}}$  sites.

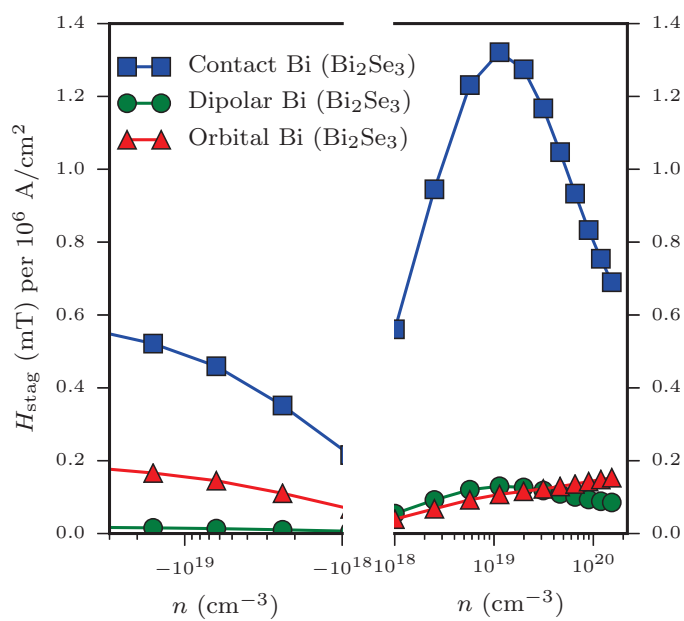


**Figure B.1** Contributions to the staggered magnetization at the Bi sites as a function of carrier density

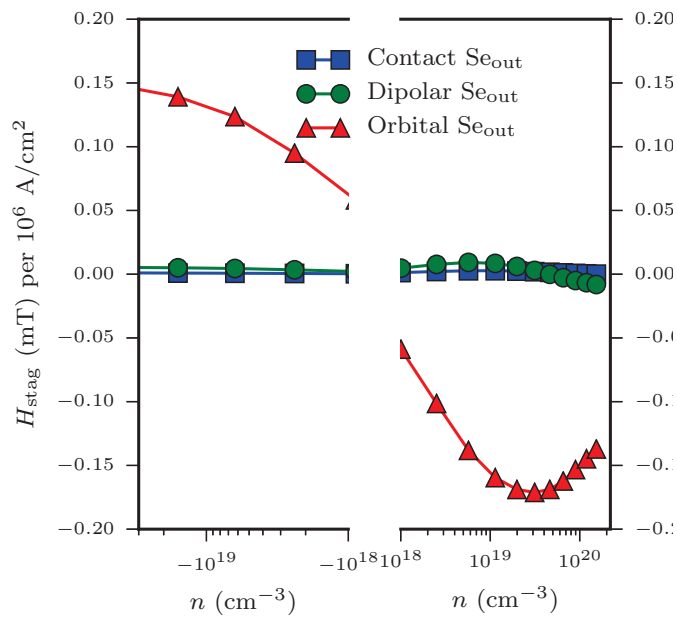


**Figure B.2** Contributions to the staggered magnetization at the Se<sub>out</sub> sites as a function of carrier density

## Bibliography

- [1] Zhang, X., Liu, Q., Luo, J., Freeman, A. & Zunger, A. Hidden spin polarization in inversion-symmetric bulk crystals. *Nature Physics* **10**, 387–393 (2014).
- [2] Ryoo, J. H. & Park, C.-H. Hidden orbital polarization in diamond, silicon, germanium, gallium arsenide and layered materials. *NPG Asia Materials* **9** (2017).
- [3] Liu, Q. *et al.* Search and design of nonmagnetic centrosymmetric layered crystals with large local spin polarization. *Phys. Rev. B* **91**, 235204 (2015). URL <https://link.aps.org/doi/10.1103/PhysRevB.91.235204>.
- [4] Riley, J. M. *et al.* Direct observation of spin-polarized bulk bands in an inversion-symmetric semiconductor. *Nature Physics* **10**, 835–839 (2014).
- [5] Razzoli, E. *et al.* Selective probing of hidden spin-polarized states in inversion-symmetric bulk MoS<sub>2</sub>. *Phys. Rev. Lett.* **118**, 086402 (2017). URL <https://link.aps.org/doi/10.1103/PhysRevLett.118.086402>.
- [6] Li, P. & Appelbaum, I. Kramers' revenge. *arXiv* **1801** (2018).
- [7] Jungwirth, T., Marti, X., Wadley, P. & Wunderlich, J. Antiferromagnetic spintronics. *Nature Nanotechnology* **11**, 231–241 (2016).
- [8] Boutin, S., Ramírez-Ruiz, J. & Garate, I. Tight-binding theory of NMR shifts in topological insulators Bi<sub>2</sub>Se<sub>3</sub> and Bi<sub>2</sub>Te<sub>3</sub>. *Phys. Rev. B* **94**, 115204 (2016). URL <https://link.aps.org/doi/10.1103/PhysRevB.94.115204>.
- [9] Rashba, E. I. & Sheka, V. I. Symmetry of energy bands in crystals of wurtzite type ii. symmetry of bands with spin-orbit interaction included. *Fiz. Tverd.* 162–176 (1959).
- [10] Hasan, M. Z. & Kane, C. L. Colloquium: Topological insulators. *Rev. Mod. Phys.* **82**, 3045–3067 (2010). URL <https://link.aps.org/doi/10.1103/RevModPhys.82.3045>.
- [11] Park, J.-H., Kim, C. H., Rhim, J.-W. & Han, J. H. Orbital Rashba effect and its detection by circular dichroism angle-resolved photoemission spectroscopy. *Phys. Rev. B* **85**, 195401 (2012). URL <https://link.aps.org/doi/10.1103/PhysRevB.85.195401>.

- [12] Slater, J. C. & Koster, G. F. Simplified LCAO method for the periodic potential problem. *Phys. Rev.* **94**, 1498–1524 (1954). URL <https://link.aps.org/doi/10.1103/PhysRev.94.1498>.
- [13] Sutton, A. P. *Electronic Structure of Materials* (Clarendon Press, 1993).
- [14] Petersen, L. & Hedegard, P. A simple tight-binding model of spin–orbit splitting of sp-derived surface states. *Surface Science* **459**, 49 – 56 (2000). URL <http://www.sciencedirect.com/science/article/pii/S0039602800004416>.
- [15] Mildred S. Dresselhaus, A. J., Gene Dresselhaus. *Group Theory: Application to the Physics of Condensed Matter* (Springer-Verlag Berlin Heidelberg, 2008).
- [16] Zhang, H. *et al.* Topological insulators in Bi<sub>2</sub>Se<sub>3</sub>, Bi<sub>2</sub>Te<sub>3</sub> and Sb<sub>2</sub>Te<sub>3</sub> with a single Dirac cone on the surface. *Nature Physics* **5**, 438–442 (2009).
- [17] Armitage, N. P., Mele, E. J. & Vishwanath, A. Weyl and Dirac semimetals in three-dimensional solids. *Rev. Mod. Phys.* **90**, 015001 (2018). URL <https://link.aps.org/doi/10.1103/RevModPhys.90.015001>.
- [18] Slichter, C. P. *Principles of magnetic resonance* (Springer-Verlag, 1990), 3rd edn.
- [19] Li, H. *et al.* Intraband and interband spin-orbit torques in noncentrosymmetric ferromagnets. *Phys. Rev. B* **91**, 134402 (2015). URL <https://link.aps.org/doi/10.1103/PhysRevB.91.134402>.
- [20] Garate, I. & MacDonald, A. H. Influence of a transport current on magnetic anisotropy in gyrotropic ferromagnets. *Phys. Rev. B* **80**, 134403 (2009). URL <https://link.aps.org/doi/10.1103/PhysRevB.80.134403>.
- [21] Moriya, T. The effect of electron-electron interaction on the nuclear spin relaxation in metals. *J. Phys. Soc. Jpn* **18** (1963).
- [22] Garate, I., Gilmore, K., Stiles, M. D. & MacDonald, A. H. Nonadiabatic spin-transfer torque in real materials. *Phys. Rev. B* **79**, 104416 (2009). URL <https://link.aps.org/doi/10.1103/PhysRevB.79.104416>.
- [23] S. W. Kim, J. D., S. Vrtnik & Jung, M. H. Antiferromagnetic order induced by gadolinium substitution in Bi<sub>2</sub>Se<sub>3</sub> single crystals. *Appl. Phys. Lett.* **106** (2015).
- [24] Young, B.-L. *et al.* Probing the bulk electronic states of Bi<sub>2</sub>Se<sub>3</sub> using nuclear magnetic resonance. *Phys. Rev. B* **86**, 075137 (2012). URL <https://link.aps.org/doi/10.1103/PhysRevB.86.075137>.
- [25] Nisson, D. M., Dioguardi, A. P., Peng, X., Yu, D. & Curro, N. J. Anomalous nuclear magnetic resonance spectra in Bi<sub>2</sub>Se<sub>3</sub> nanowires. *Phys. Rev. B* **90**, 125121 (2014). URL <https://link.aps.org/doi/10.1103/PhysRevB.90.125121>.
- [26] Kobayashi, K. Electron transmission through atomic steps of Bi<sub>2</sub>Se<sub>3</sub> and Bi<sub>2</sub>Te<sub>3</sub> surfaces. *Phys. Rev. B* **84**, 205424 (2011). URL <https://link.aps.org/doi/10.1103/PhysRevB.84.205424>.

- [27] A.Hruban *et al.* Reduction of bulk carrier concentration in Bridgman-grown Bi<sub>2</sub>Se<sub>3</sub> topological insulator by crystallization with Se excess and Ca doping. *Journal of Crystal Growth* **407**, 63–67 (2014).
- [28] Sugama, Y., Hayashi, T., Nakagawa, H., Miura, N. & Kulbachnskii, V. Magnetoresistance and Shubnikov–de Haas effect in magnetic ion-doped Bi<sub>2</sub>Se<sub>3</sub>. *Physica B* **298**, 531–535 (2001).
- [29] Butch, N. P. *et al.* Strong surface scattering in ultrahigh-mobility Bi<sub>2</sub>Se<sub>3</sub> topological insulator crystals. *Phys. Rev. B* **81**, 241301 (2010). URL <https://link.aps.org/doi/10.1103/PhysRevB.81.241301>.
- [30] Hor, Y. S. *et al.* *p*-type Bi<sub>2</sub>Se<sub>3</sub> for topological insulator and low-temperature thermoelectric applications. *Phys. Rev. B* **79**, 195208 (2009). URL <https://link.aps.org/doi/10.1103/PhysRevB.79.195208>.
- [31] Checkelsky, J. G. *et al.* Quantum interference in macroscopic crystals of nonmetallic Bi<sub>2</sub>Se<sub>3</sub>. *Phys. Rev. Lett.* **103**, 246601 (2009). URL <https://link.aps.org/doi/10.1103/PhysRevLett.103.246601>.
- [32] Hor, Y. S. *et al.* Superconductivity in Cu<sub>x</sub>Bi<sub>2</sub>Se<sub>3</sub> and its implications for pairing in the undoped topological insulator. *Phys. Rev. Lett.* **104**, 057001 (2010). URL <https://link.aps.org/doi/10.1103/PhysRevLett.104.057001>.
- [33] Howells, B., Edmonds, K. W., Campion, R. P. & Gallagher, B. L. Temperature dependence of spin-orbit torque effective fields in the diluted magnetic semiconductor (Ga,Mn)As. *Appl. Phys. Lett.* **105** (2014).
- [34] Železný, J. *et al.* Spin-orbit torques in locally and globally noncentrosymmetric crystals: Antiferromagnets and ferromagnets. *Phys. Rev. B* **95**, 014403 (2017). URL <https://link.aps.org/doi/10.1103/PhysRevB.95.014403>.
- [35] Fang, L. *et al.* Catalyst-free growth of millimeter-long topological insulator Bi<sub>2</sub>Se<sub>3</sub> nanoribbons and the observation of the  $\pi$ -Berry phase. *Nano Lett.* **12**, 6164–6169 (2012).
- [36] Dobrovinskaya, E. R., Lytvynov, L. & Pishchik, V. *Sapphire: Material, Manufacturing, Applications* (Springer Berlin, 2009).
- [37] Powell, R. C. *Symmetry, Group Theory and the Physical Properties of Crystals* (Springer, New York, 2010).
- [38] M. I. Aroyo, J. M. P.-M., Orobengoa, D., Tasci, E., de la Flor, G. & Kirov, A. *Bulg. Chem. Commun.* **43**, 183 (2011).
- [39] Ribeiro-Soares, J. *et al.* Group theory analysis of phonons in two-dimensional transition metal dichalcogenides. *Phys. Rev. B* **90**, 115438 (2014). URL <https://link.aps.org/doi/10.1103/PhysRevB.90.115438>.
- [40] Rocha Leão, C. & Lordi, V. Ab initio guided optimization of GaTe for radiation detection applications. *Phys. Rev. B* **84**, 165206 (2011). URL <https://link.aps.org/doi/10.1103/PhysRevB.84.165206>.

- [41] McGuire, M. M. Crystal and magnetic structures in layered, transition metal dihalides and trihalides. *Crystals* **7** (2017).
- [42] Johnson, R. D. *et al.* Monoclinic crystal structure of  $\alpha$  - RuCl<sub>3</sub> and the zigzag antiferromagnetic ground state. *Phys. Rev. B* **92**, 235119 (2015). URL <https://link.aps.org/doi/10.1103/PhysRevB.92.235119>.
- [43] Baek, S.-H. *et al.* Evidence for a field-induced quantum spin liquid in  $\alpha$ -RuCl<sub>3</sub>. *Phys. Rev. Lett.* **119**, 037201 (2017). URL <https://link.aps.org/doi/10.1103/PhysRevLett.119.037201>.
- [44] Binotto, L., Pollini, I. & Spinolo, G. Optical and transport properties of the magnetic semiconductor  $\alpha$ -RuCl<sub>3</sub>. *Phys. Stat. Sol. B* **44** (1971).
- [45] Zallen, R., Slade, M. L. & Ward, A. T. Lattice vibrations and interlayer interactions in crystalline As<sub>2</sub>S<sub>3</sub> and As<sub>2</sub>Se<sub>3</sub>. *Phys. Rev. B* **3**, 4257–4273 (1971). URL <https://link.aps.org/doi/10.1103/PhysRevB.3.4257>.
- [46] Stergiou, A. C. & Rentzeperis, P. J. *Z. Krist.* **173** (1985).
- [47] Sykina, K. *et al.* <sup>77</sup>Se solid-state NMR of As<sub>2</sub>Se<sub>3</sub>, As<sub>4</sub>Se<sub>4</sub> and As<sub>4</sub>Se<sub>3</sub> crystals: a combined experimental and computational study. *Phys. Chem. Chem. Phys.* **15** (2013).
- [48] Madelung, O., Rossler, U. & Schulz, M. (eds.) *Non-Tetrahedrally Bonded Elements and Binary Compounds I* (Springer Berlin, 1998).
- [49] Noro, Y. & Miyara, S. Electrical resistivity of SrRuO<sub>3</sub>. *J. Phys. Soc. Jpn* **27** (1969).
- [50] Zayak, A. T., Huang, X., Neaton, J. B. & Rabe, K. M. Structural, electronic, and magnetic properties of SrRuO<sub>3</sub> under epitaxial strain. *Phys. Rev. B* **74**, 094104 (2006). URL <https://link.aps.org/doi/10.1103/PhysRevB.74.094104>.
- [51] Yoshimura, K. *et al.* <sup>17</sup>O NMR observation of universal behavior of ferromagnetic spin fluctuations in the itinerant magnetic system Sr<sub>1-x</sub>Ca<sub>x</sub>RuO<sub>3</sub>. *Phys. Rev. Lett.* **83**, 4397–4400 (1999). URL <https://link.aps.org/doi/10.1103/PhysRevLett.83.4397>.
- [52] Chi, H. *et al.* Low-temperature structural and transport anomalies in Cu<sub>2</sub>Se. *Phys. Rev. B* **89**, 195209 (2014). URL <https://link.aps.org/doi/10.1103/PhysRevB.89.195209>.
- [53] Li, R. *et al.* Room- and low-temperature crystallographic study of the ambient pressure organic superconductor (Bisethylene dithiotetrathiofulvalene)<sub>4</sub>Hg<sub>2.89</sub>Br<sub>8</sub>. *Chem. Mater.* **10** (1998).
- [54] Reehuis, M. *et al.* Crystal structure and high-field magnetism of La<sub>2</sub>CuO<sub>4</sub>. *Phys. Rev. B* **73**, 144513 (2006). URL <https://link.aps.org/doi/10.1103/PhysRevB.73.144513>.
- [55] Dupont-Ferrier, E. *et al.* Coherent coupling of two dopants in a silicon nanowire probed by Landau-Zener-Stückelberg interferometry. *Phys. Rev. Lett.* **110**, 136802 (2013). URL <https://link.aps.org/doi/10.1103/PhysRevLett.110.136802>.
- [56] Cardona, M. Semiconductors under uniaxial strain. *Phys. Stat. Sol. B* **198** (1996).

- [57] Froyen, S. & Harrison, W. A. Elementary prediction of linear combination of atomic orbitals matrix elements. *Phys. Rev. B* **20**, 2420–2422 (1979). URL <https://link.aps.org/doi/10.1103/PhysRevB.20.2420>.
- [58] Jancu, J.-M., Scholz, R., Beltram, F. & Bassani, F. Empirical spds\* tight-binding calculation for cubic semiconductors: General method and material parameters. *Phys. Rev. B* **57**, 6493–6507 (1998). URL <https://link.aps.org/doi/10.1103/PhysRevB.57.6493>.
- [59] Niquet, Y. M., Rideau, D., Tavernier, C., Jaouen, H. & Blase, X. Onsite matrix elements of the tight-binding Hamiltonian of a strained crystal: Application to silicon, germanium, and their alloys. *Phys. Rev. B* **79**, 245201 (2009). URL <https://link.aps.org/doi/10.1103/PhysRevB.79.245201>.
- [60] Kane, B. E. A silicon-based nuclear spin quantum computer. *Nature* **393**, 133–137 (1998).
- [61] Pioro-Ladrière, M. *et al.* Electrically driven single-electron spin resonance in a slanting Zeeman field. *Nature Physics* **4**, 776–779 (2008).
- [62] Laird, E. A. *et al.* Hyperfine-mediated gate-driven electron spin resonance. *Phys. Rev. Lett.* **99**, 246601 (2007). URL <https://link.aps.org/doi/10.1103/PhysRevLett.99.246601>.